Nanoscale Lubricant Flow and Heat Transfer at the Head-Disk Interface in Hard Disk Drives

by

Siddhesh Vivek Sakhalkar

A dissertation submitted in partial satisfaction of the

requirements for the degree of

Doctor of Philosophy

in

Engineering - Mechanical Engineering

in the

Graduate Division

of the

University of California, Berkeley

Committee in charge:

Professor David B. Bogy, Chair
Professor Shawn Shadden
Professor Per-Olof Persson

Summer 2020

Nanoscale Lubricant Flow and Heat Transfer at the Head-Disk Interface in Hard Disk Drives

Abstract

Nanoscale Lubricant Flow and Heat Transfer at the Head-Disk Interface in Hard Disk Drives

by

Siddhesh Vivek Sakhalkar

Doctor of Philosophy in Engineering - Mechanical Engineering

University of California, Berkeley

Professor David B. Bogy, Chair

In the hard disk drive (HDD) industry, technologies such as Heat-Assisted Magnetic Recording (HAMR) and Microwave-Assisted Magnetic Recording (MAMR) are currently under development to increase the areal density of contemporary HDDs beyond 1 Tb/in^2. Traditional magnetic media has reached the superparamagnetic limit: if the size of the media bits is further decreased (to increase the areal density), the bits will become thermally unstable. HAMR and MAMR aim to overcome this obstacle and increase the data density by using a high coercivity magnetic media that can store data at very small bit sizes of $\sim$(25 nm)^2. To reduce the coercivity of this media temporarily while writing, HAMR heads are integrated with a laser delivery system that heats the media to $\sim$500 ^{o}C using a $\sim$20 nm FWHM laser. MAMR heads contain a Spin Torque Oscillator that bombards the media with a microwave field, lowering its coercivity during writing. These new components introduce additional thermal complications to the already challenging head-disk interface (HDI) design. In contemporary HDDs, the recording head slider, which contains the read/write transducers, "flies" in close proximity to the rotating disk ($<$ 5 nm). Such a low spacing is achieved via the Thermal Fly Height Control (TFC) technology, where an embedded joule heater locally protrudes the slider's trailing edge. With the addition of new components required for the energy-assist in HAMR/MAMR, head overheating is a major reliability concern for both these technologies. Moreover, laser heating of the disk during HAMR causes the $\sim$1 nm thick lubricant layer, that coats and protects the disk, to deform, evaporate and condense on the head. This disk-to-head lubricant transfer in turn causes detrimental issues such as write-induced head contamination. Therefore, there is a need to understand the flow and transfer of the lubricant and the nanoscale heat transfer in the HDI to develop robust HAMR/MAMR drives.

While the lubricant behavior is traditionally modelled using viscous lubrication theory in the HDD industry, experiments show that HDD lubricants are, in reality, viscoelastic fluids.

At the small timescales involved in HAMR writing (∼ns), the elastic mode of the lubricant can no longer be ignored. In this dissertation, we introduce a modification to the traditional (viscous) Reynolds lubrication equation using the linear Maxwell (viscoelastic) constitutive equation and a slip boundary condition. We study the deformation and recovery of the lubricant due to laser heating under the influence of thermocapillary (Marangoni) stress and disjoining pressure. When subjected to a 20 nm FWHM scanning laser spot, the lubricant profile consists of an elastic trough centered at the instantaneous laser location, followed by a viscous trail. When the laser is turned off, the elastic trough recovers instantaneously, leaving behind the viscous trail, which recovers over a time scale of μs.

Further, we develop viscous and viscoelastic models for the disk-to-head lubricant transfer during HAMR writing. These models simultaneously determine the deformation and evaporation of the lubricant film on the disk, the diffusion of the vapor phase lubricant in the HDI and the evolution of the condensed lubricant film on the slider. We investigate the effect of lubricant properties such as viscoelasticity, lubricant type (Zdol vs Ztetraol), molecular weight, slip length, disjoining pressure, and HAMR design parameters such as head/media temperature, lubricant thickness and laser FWHM on the lubricant transfer. We find a significant difference between the rates of transfer for Zdol (∼ns) vs Ztetraol (∼ μs). The viscous model overpredicts the amount of transfer compared to the viscoelastic model.

Traditionally, the heat transfer coefficient in the HDI is determined by estimating thermal conduction through air using the energy equation with temperature jump theory. However, with the minimum fly height of less than 5 nm in contemporary HDDs, energy transfer due to phonon conduction also becomes significant. We present a numerical model to simulate the head temperature due to heat transfer across a closing nanoscale gap between the head and the non-rotating media. Our model employs a spacing-dependent heat transfer coefficient due to the combined effects of air conduction and wave-based phonon conduction. We compare our simulations with static touchdown experiments performed with a TFC slider resting on three different media (Si, magnetic disks with AlMg and glass substrates). The TFC heater is powered to create a local protrusion, leading to head-media contact and a resistive sensor (Embedded Contact Sensor or ECS) is used to detect the head temperature change. With the introduction of intermolecular van der Waals forces between the head and the media, we demonstrate a good quantitative match with experiments for all of the media materials tested, at different head-media spacings and in different environments (air, vacuum).

Next, we develop a numerical model to predict the temperature profile and the fly height for a flying slider over a rotating disk. We compare our simulations with touchdown experiments performed with a flying TFC slider using the ECS to record the temperature change. To accurately predict the heat transfer and fly height at near-contact, we incorporate the effects of disk temperature rise, intermolecular adhesion & contact forces, air & phonon conduction heat transfer and friction heating in our model. We investigate the impact of each of these features on head temperature during flying. We find that simulation with all these features agrees well with the experiment.

To my wife, Anushka Gupta,
my parents, Vrinda & Vivek Sakhalkar
and Ketaki, Aditya & Anika Samant

This PhD is as much yours as it is mine, if not more.

Contents

List of Figures

List of Tables

List of Abbreviations

ABS	Air Bearing Surface
ASRC	Advanced Storage Research Consortium
CML	Computer Mechanics Laboratory
DLC	Diamond-Like-Carbon
ECS	Embedded Contact Sensor
FWHM	Full-Width at Half-Maximum
HAMR	Heat-Assisted Magnetic Recording
HDD	Hard Disk Drive
HDI	Head-Disk Interface
MAMR	Microwave-Assisted Magnetic Recording
NFT	Near-Field Transducer
PFPE	Perfluoropolyether
PMR	Perpendicular Magnetic Recording
SNR	Signal-to-Noise Ratio
SSD	Solid State Drive
STO	Spin Torque Oscillator
TE	Trailing Edge
TFC	Thermal Fly Height Control
vdW	van der Waals
VCM	Voice Coil Motor

Acknowledgments

First and foremost, I would like to sincerely thank my adviser, Prof. David B. Bogy for guiding and supporting me throughout my doctoral study at UC Berkeley. I am grateful to him for giving me the freedom to pursue my own research ideas and instincts while at the same time nudging me in the right direction when I felt lost or stuck. I have thoroughly enjoyed all my discussions with him about technical problems, career advice, research & writing style and even general topics like family, health, well-being and politics. It has been a great honor to have had him as my mentor and adviser.

I would also like to thank Profs. Shawn Shadden and Per-Olof Persson for serving on my qualifying exam committee and for reviewing my dissertation. I have thoroughly enjoyed taking classes at Berkeley and am grateful to all my teachers, including but not limited to Profs. Johnson, Dames, Shadden, Persson, Morris, Steigman, Papadopoulos, Evans and Collela. My coursework at Berkeley and discussions with my instructors has shaped my thought process and approach to solving problems and I am grateful for the same.

The research presented in this dissertation was supported by the Computer Mechanics Laboratory (CML) at UC Berkeley. I would like to thank my colleagues at CML: Dr. Soroush Sarabi, Dr. Yuan Ma, Dr. Haoyu Wu, Tholfaqar "Dolf" Mardan, Amin Ghafari, Yuying Wu, Qilong Cheng and Dr. Bair Budaev. My work on lubricant behavior during HAMR was influenced by Soroush's work and I thank him for sharing and explaining his research experience when I first joined the lab. My work on nanoscale heat transfer during static touchdown was influenced by Yuan's thesis and I thank him for sharing his experience with me. I have particularly enjoyed working closely with Amin and Qilong. In the last 2 years, we were the only 3 grad students at CML working in unison, with Qilong doing experiments, Amin working on nanoscale heat transfer theory and me working on simulations. I am especially grateful to Amin - discussions with him regarding computation techniques, heat transfer theory, PhD life and job search have been most fruitful.

My research would not have been possible without the support of Western Digital, SAE Magnetics and the Advanced Storage Research Consortium (ASRC). I would like to thank Dr. Robert Smith, Dr. JP Peng, Dr. Weidong Huang, Dr. Erhard Schreck, Dr. Sukumar Rajauria, Dr. Shaomin Xiong, Dr. Xinjiang Shen, Dr. Tan Trinh and Dr. Qing Dai of Western Digital and Dr. Huan Tang of Seagate for helpful discussions during ASRC meetings and CML Sponsors' Meetings. In particular, I would like to thank JP and Robert whose regular feedback and queries have helped improve my research work. I would also like to thank Dr. Alejandro Mendez from SAE Magnetics and Dr. Tom Karis from TEK Data Systems for helpful tips and suggestions.

In the summer of 2017, I was fortunate to work at Western Digital in San Jose and I would like to thank Jim O'Neill, Bob Reinhart and Dr. Manoj Keshavan for their support. I am especially thankful to Manoj for sharing his vast technical knowledge and hands-on experimental skills with me.

I would like to thank my friends at Berkeley: Milind Hegde, Koulik Khamaru, Shruti Bathia, Anamika Chowdhari, Satyaki Mukherjee, Niharika Gupta, Bala TK, Anurag Roy,

Vipul Gupta, Kristine Tan and Nick Bhattacharya. You made my life at Berkeley fun.

I would especially like to thank my best friends from undergrad - Sandeep Yogi, Atul Dukale and Prasanna Raut for supporting me from miles away. Your friendship means the world to me and phone calls with you have kept me sane at times of despair.

Finally, my accomplishments would not have been possible without the unconditional love, support and encouragement of my family. I am thankful to my grandparents; these words from my grandfather's doctoral thesis have inspired me in my own PhD, "This doctorate has given me the profound satisfaction of doing a truly unbiased research work, for which, I believe, there is no substitute in this material world." I would like to thank my parents, Vrinda and Vivek Sakhalkar for giving me the freedom to make my own decisions and pursue my own ambitions. I am most grateful to my mother. I know I don't say this a lot, but you mean the world to me. I never understand how she can so selflessly put the needs of me and my sister ahead of herself. I strive to be a better person everyday because of her. I am thankful to Ketaki, Aditya and Anika Samant for providing me a second home in the US. My sister, Ketaki has always been there for me growing up and whenever I had any problems during my PhD and I am most grateful. I could not have asked for a better sister. Spending time with her daughter, Anika has given me joy, like I have never experienced before. I would like to thank my in-laws family, Rekha Gupta, Vartika, Sumit and Kartikeya Gahoi for welcoming me with so much warmth and affection into their family. Their love and support means a lot to me. Lastly and most importantly, I would like to thank my wife, Anushka Gupta. You are my life, you are my world. You have seen me through everything - all the ups and the never-ending downs and you have always been there. I could never have done this PhD without you. I love you, for my life.

Chapter 1

Introduction

In today's digital world, data is indispensable. The amount of data generated has been growing significantly in the last few years and is expected to grow even more rapidly in the future. The International Data Corporation (IDC) predicts that the global datasphere (total amount of data created and consumed) will grow from approximately 50 ZB in 2020 to 175 ZB in 2025 (1 ZB (zettabyte) = 10^9 TB (terabyte)) [1]. Today most of the world's data is stored in two types of devices - Hard Disk Drives (HDDs) and NAND Flash (which includes NAND flash-based Solid State Drives (SSDs), USB flash drives, memory cards etc.) [2]. The advantage of flash is that it is much faster than HDDs in reading and writing data. However, flash is much more expensive than HDD - currently, the ratio of the price-per-TB of NAND flash to HDD is $\sim 9:1$ [2, 3]. While NAND flash has been dominating over HDDs in smartphones, laptops and other consumer electronics due to speed, this stark price margin makes HDDs the preferred storage medium in cloud data centers. For instance, in 2018, HDDs accounted for 76 % of all manufactured storage and NAND flash accounted for 20 % [2]. With the increasing emphasis on cloud-based storage in recent times for a myriad of applications ranging from storing photos on iCloud to performing complex simulations using cloud computing to saving genomic datasets on Amazon Web Services (AWS) to backing-up sensitive industry information on Box or Google Drive, HDDs are expected to retain their importance and dominance in the years to come.

The first commercial HDD launched by IBM in 1956 (IBM 350 [4]) had a capacity of just 3.75 MB (megabytes) and was leased for $ 3200 a month, which adjusting for inflation is equivalent to about $ 28,000 today! Moreover, it had a physcial volume of 1.9 m^3 (approximately the size of two medium-sized refrigerators) and a weight of 910 kg. Today, Seagate supplies a 16 TB HDD for just $ 400 that weighs only 670 g (physical volume of 390 cm^3) [5]. This dramatic increase in areal density (from around 2000 bits/in^2 in IBM 350 to 1.3 Tb(terabits)/in^2 in today's commercial HDDs) and decrease in cost per bit has been made possible due to significant technological breakthroughs in the last 50 years in the HDD industry. With the exploding data requirements in today's day and age, the HDD industry continues to push the limits in order to further increase the areal density of these devices to provide cheaper and better storage solutions.

1.1 Hard Disk Drive Technology and the Head-Disk Interface

The main components of a HDD are as follows (Figure 1.1):

- a magnetic disk (or media) that stores binary data
- a spindle motor that holds and rotates the disks at a high rotational speed (3600 - 10,000 RPM)
- a slider containing read/write transducers that magnetizes a local region on the disk to read or write data
- the suspension
- an actuator arm
- a Voice Call Motor (VCM)

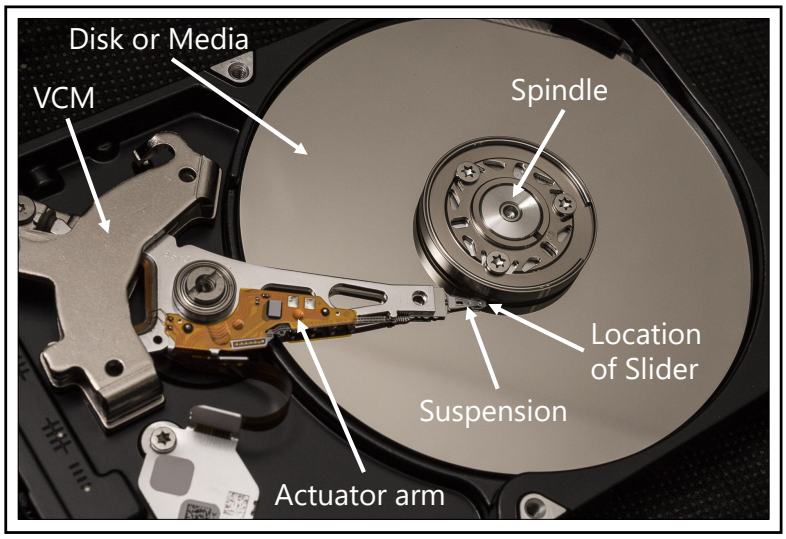

Figure 1.1: Basic structure and components of a hard disk drive

The disk stores binary data in a thin magnetic layer in the form of bits, which are magnetically oriented regions made up of tens or hundreds of grains with either "up" or "down" orientation. Contemporary Perpendicular Magnetic Recording (PMR) disks have a multi-layered structure comprising of the substrate (AlMg or glass), magnetic layers ($\sim$ 100 nm thick), a $\sim$2 nm thick Diamond-like-carbon (DLC) layer and a $\sim$1 nm thick lubricant layer (Figure 1.2). The hard DLC layer protects the soft magnetic layers from impact/wear/corrosion.

The lubricant layer reduces wear and friction between the slider and the disk and also protects the slider and the disk from damage due to intermittent contacts. We use the terms "disk" and "media" interchangeably in this dissertation.

The disk is divided into concentric radial segments called tracks. Each track is subdivided into several sectors where the magnetic bits are stored. A sector is the minimum storage unit on the disk (typically 512 bytes in size). The spindle motor (which is fixed to the HDD casing) rotates the disk platter at a high RPM, allowing the read/write transducers in the slider to have access to different sectors on a particular track.

The slider block is composed of two parts - AlTiC and the trailing edge (TE) portion that is made of Al_2O_3 (Figure 1.2). While the term "slider" refers to the entire block (AlTiC + Al_2O_3), the term "head" typically refers to the local TE portion which contains the read/write transducers. Like the disk, the surface of the slider facing the disk is also protected by a $\sim$2 nm thick DLC layer. The slider is attached to the end of the suspension which is in turn attached to the actuator arm. The VCM controls the actuator arm angle thereby enabling the head assembly to have access to different radial tracks on the rotating disk. Through the rotation of the disk and the actuator arm, the read/write transducers in the slider can access a particular disk sector on a specific track and read/write data by converting magnetic field transitions into electric current (read the disk) or vise versa (write on the disk).

In this dissertation, we are interesting in studying the reliability of the region between the head and the disk, called the Head-Disk Interface (HDI). During the operation of a HDD, the magnetic recording head with embedded read/write transducers "flies" over the rotating disk. The disk's rotation pulls air into the interface between the head and the disk, forming an air bearing. Compression of the air in the HDI generates an air pressure driven lift force on the the surface of the slider facing the disk called the Air Bearing Surface (ABS). The air bearing lift force opposes the applied suspension load and moments that push the slider towards the disk. In equilibrium, these two opposing forces balance each other allowing the slider to stably fly over the disk at a distance known as the fly height (Figure 1.2).

Perfluoropolyethers (PFPEs) are the widely used lubricants to coat and protect the disk in HDDs because of their beneficial properties such as low surface energy, low viscosity, low vapor pressure, chemical stability, thermal stability, transparency and lack of odor. PFPEs that have the Z type backbone chain are most commonly used in HDDs:

$$X - [(OCF_2)_m - (OCF_2CF_2)_n - (OCF_2CF_2CF_2)_p - (OCF_2CF_2CF_2CF_2)_q]_{x_0} - OX$$

where X is the end group. The earliest commercially available PFPEs had non-polar end groups (such as CF3) and are hence called nonpolar PFPEs [6]. Lately, polar PFPEs with functional end groups (such as hydroxyl) have become ubiquitous in HDDs. These polar end groups interact with the DLC through hydrogen bonding and provide an additional means to customize and improve the lubricant properties such as viscosity, vapor pressure and surface energy [6]. For example, three of the most common PFPEs are:

- Non-polar Fomlin Z with X = CF3

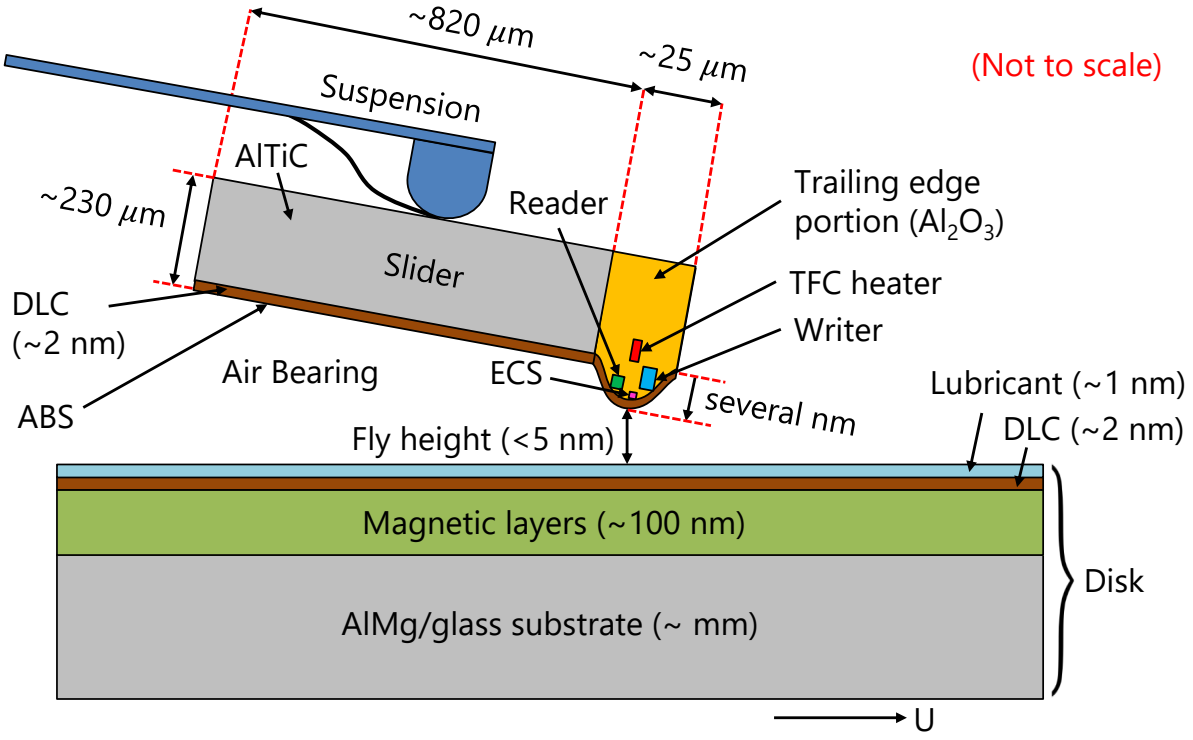

Figure 1.2: Schematic of the head-disk interface (HDI). The Thermal Fly Height Control (TFC) heater is powered, causing a local thermal protrusion (several nm in height and tens of microns in diameter) near the slider's trailing edge, thereby reducing the spacing between the read/write transducers in the head and the disk.

- Polar Zdol, which has 2 hydroxyl end-groups with $X = CF_2CH_2 - OH$
- Polar Ztetraol, which has 4 hydroxyl end groups with $X = CF_2CH_2OCH_2CH(-OH)CH_2-OH$

1.2 Thermal Fly-Height Control Technology (TFC) and its challenges

A major emphasis of the storage industry is to increase the areal data density - pack more and more data into the same disk area. This is achieved by reducing the size of the bits on the disk. The Wallace Spacing Loss equation states that the intensity of the read-back signal from the disk increases exponentially as the distance between the magnetic media and the read/write transducers is decreased [7]. Assuming that the media is sinusoidally magnetized with wavelength λ, Wallace showed that the magnetic flux detected by the reader is proportional to $\exp(-\frac{2\pi d}{\lambda})$, where d is the spacing between the magnetic media layer and

the read/write transducers in the head. For a storage disk, the recorded wavelength λ is proportional to the bit length. Therefore, as the bit length is decreased to increase storage density, the read-write head must be brought closer to the magnetic media to ensure a strong read-back signal and reliable read-write operations with a good signal to noise ratio (SNR) [8]. Hence, contemporary commercial PMR HDDs have a minimum fly height of less than 5 nm.

Traditionally, the slider fly height has been reduced in HDDs by modifying the ABS design or the suspension. However, this strategy becomes extremely challenging when the fly height needs to be reduced below 5 nm. At such small spacings, intermolecular forces between the slider and the disk become significant. These forces lead to dynamic instability and intermittent contact in the flying slider. Hence, a new technology is necessary to stably achieve an ultra-low fly height by minimizing these intermolecular forces and reducing the probability of occasional head-disk contact.

In contemporary sliders, a controlled head-disk spacing of less than 5 nm is achieved via the Thermal-Fly Height Control (TFC) technology [9]. A joule heater (see TFC heater in Figure 1.2) is embedded near the slider's ABS close its trailing edge. The TFC heater is powered, causing a local thermal protrusion near the slider's trailing edge, thereby reducing the spacing between the read/write transducers in the head and the disk. This thermal protrusion has a diameter of about tens of microns and a height of several nm (Figure 1.2). Due to the localized nature of this protrusion, most of the slider remains relatively far away from the disk ($>$ 10 nm), thereby minimizing intermolecular forces between the slider and the disk and avoiding any detrimental head-disk contact.

The actuation of the TFC and the resultant fly height reduction has been extensively studied in literature [10–16]. Contemporary TFC sliders also have a resistive Embedded Contact Sensor (ECS) near the ABS (Figure 1.2) that can be utilized to record the head surface temperature change during the actuation of the TFC and thereby indirectly detect head-disk contact that produces frictional heating [17].

Joule heating of the TFC heater in contemporary low-flying height PMR heads causes high temperatures in the head. The air bearing can act as a cooling agent by transferring heat from the head to the disk. Therefore, understanding head cooling via heat transfer in the HDI is a topic of utmost importance for HDD reliability.

Traditionally, the heat transfer coefficient in the HDI is determined solely due to thermal conduction through the pressurized air bearing by solving the continuum energy equation with temperature jump theory [18, 19]. However, with the minimum fly height of less than 5 nm in contemporary HDDs, contributions due to near field radiation and phonon conduction also become significant. Previous experimental studies [20, 21] and wave-based theories of radiation and phonon conduction [22–25] have shown that the heat transfer coefficient increases significantly at nanoscale gaps. In order to accurately predict head/media temperatures in contemporary low flying height HDDs, it is imperative to consider contributions due to near field-radiation and phonon conduction in addition to traditional air conduction.

1.3 Heat-Assisted Magnetic Recording (HAMR) and its challenges

Contemporary PMR drives have approached upto 1.3 Tb/in^2 storage density. Higher storage densities will soon no longer be possible with convectional recording technologies such as PMR due to the superparamagnetic limit: if the size of the media bits is further decreased, the bits will become thermally unstable (i.e. orientation of the magnetic grains would fluctuate randomly under thermal activation at room temperature, thereby corrupting the data). Heat-Assisted Magnetic Recording (HAMR) [26] offers to overcome this limitation by using a magnetic media material with a high coercivity (such as $L1_0$-FePt) [27]. Coercivity is the resistance of a material against change in its magnetic orientation. Its high coercivity enables the HAMR media to reliably store data at very small bit sizes of $\sim$(25 nm)^2. However, this poses an additional challenge - how do we write data onto this high coercivity media?

The coercivity of a material is temperature dependent. If the temperature of a magnetized material is increased above its Curie temperature, its coercivity becomes significantly lower, until it has cooled down. HAMR takes advantage of this property to write on the high coercivity media by locally heating the recording bit to its Curie temperature ($\sim$500 ^{o}C) within a few nanoseconds during writing. This is achieved by integrating an optical system into the slider comprising of a laser diode, a waveguide and a Near-Field Transducer (NFT) that is utilized to create the required $\sim$20 nm FWHM hotspot on the media. Once the write operation is completed, the laser is turned off, which allows the bit to cool down to room temperature, thereby "freezing" the data (see Figure 1.3). HAMR drives are projected to push the areal density of HDDs to 5 or even 10 Tb/in^2.

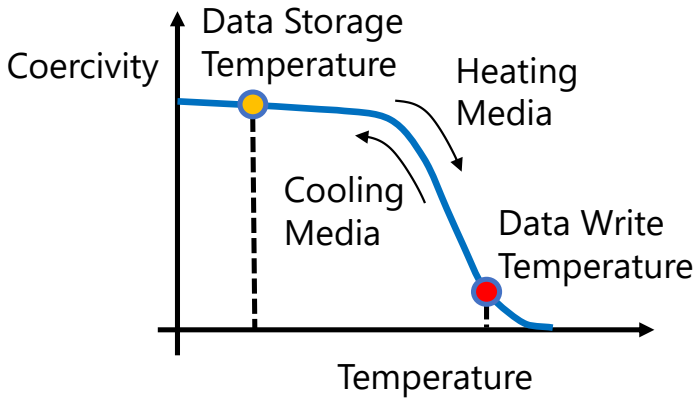

Figure 1.3: An illustration of the HAMR write process and material coercivity vs temperature. Inspired by Figure 1 of Ref. [26].

However, reliability of the head-disk interface (HDI) during high temperature transient laser heating still remains a major challenge that needs to be addressed before HAMR can be made into a robust commercial product [28]. Inside the head, the waveguide focuses

the size of laser beam generated by the laser diode from microns to ∼200-500 nm. The NFT further shrinks the laser beam size down to the required 20 nm through the plasmonic effect. However, this process is extremely inefficient and involves significant heat dissipation. Additionally, since the NFT is in close proximity to the media (< 5 nm), a thermal back heating is also possible from the high temperature disk to the NFT. These two effects together lead to high temperatures in the NFT (∼300 °C) [29]. NFT failure due to overheating is one of the biggest concerns for HAMR. Understanding nanoscale heat transfer in the HDI is therefore imperative to manage overheating not only for contemporary PMR drives but also for emerging technologies such as HAMR.

Moreover, the media including the DLC layer and the lubricant layer are exposed to very high temperature gradients ($\sim 10^{10}$ °C/m) and rapid laser heating and cooling cycles at a timescale of ∼ns while writing. This imposes numerous reliability problems for these materials. For instance, the high temperature gradient on the media causes the lubricant to deform and deplete under the influence of driving forces such as thermo-capillary stress (or Marangoni stress), evaporation and thermal degradation. The lubricant must be able to withstand this writing process and sufficiently recover the depletion and accumulation zones to ensure that the disk remains well-protected and the head flies stably. Additionally, the temperature difference between the disk (∼500 °C) and the head (∼300 °C) causes the lubricant to evaporate from the disk and condense on the relatively cooler head. The lubricant acts as a carrier, causing a continuous deposition of contaminants from all over the media at the head NFT. This write-induced head contamination is one of the major roadblocks to the commercialization of HAMR [29, 30]. Understanding the mechanism of disk-to-head lubricant transfer is necessary so as to mitigate head contamination and ensure reliable HDD operation.

While lubricant flow at the HDI has been traditionally modelled using viscous lubrication theory [31–35], experiments show that PFPE lubricants are, in reality, viscoelastic fluids [6]. A viscoelastic material can behave like a viscous fluid or an elastic solid or a combination of both depending on the flow timescale [36]. While PFPE lubricants exhibit viscous behavior in most typical applications, at small timescales involved in HAMR writing (∼ns), the elastic mode of the lubricant can no longer be ignored [37]. It is therefore necessary to account for lubricant viscoelasticity while studying the behavior of the lubricant during HAMR.

1.4 Microwave-Assisted Magnetic Recording (MAMR) and its challenges

Microwave-Assisted Magnetic Recording (MAMR) [38] is an alternative contender to achieving storage densities beyond 1 Tb/in^2 in HDDs. Like HAMR, MAMR also uses a high coercivity magnetic media to enable higher storage densities. To enable writing on the high coercivity media, MAMR heads contain a device called the Spin Torque Oscillator (STO), which bombards a microwave field on the magnetic media. This in turn reduces the coer-

civity of the media, allowing the head write data on the disk. However, the STO in MAMR heads experiences high current densities ($\sim 10^8$ A/cm^2) during writing leading to similar overheating problems (peak temperature of $> 200^o$ C) [39].

1.5 Objective of this Dissertation

Emerging technologies such as HAMR and MAMR are under rapid development to supplant PMR and achieve higher storage densities in HDDs. However, head failure due to overheating is a major reliability issue that needs to be addressed for both of these technologies. Moreover, the high media temperature gradient during HAMR writing causes the lubricant to deform and transfer to the slider, leading to detrimental reliability concerns such as write-induced contamination. The objectives of this dissertation are as follows:

- Develop a viscoelastic model to study the deformation and recovery of the lubricant on the disk during HAMR laser heating
- Study the lubricant transfer from the disk to the head during HAMR laser heating using viscous and viscoelastic models
- Develop accurate numerical models to predict head and disk temperatures due to nanoscale heat transfer in the HDI during static as well as flying conditions

1.6 Organization and Novel Contributions of this Dissertation

In this section, we highlight the novel contributions of each chapter in this dissertation. Chapter 2 presents a viscous model for lubricant transfer from the disk to the head during HAMR writing. This model simultaneously determines the thermocapillary shear stress-driven deformation and evaporation of the lubricant film on the disk, the convection and diffusion of the vapor phase lubricant in the air bearing and the evolution of the condensed lubricant film on the slider. The model also considers molecular interactions between disk–lubricant, slider–lubricant and lubricant–lubricant in terms of disjoining pressure. We investigate the effect of media temperature, head temperature, initial lubricant thickness, laser spot size and the fly-height on the lubricant transfer process.

In Chapter 3, we introduce a modification to the traditional (viscous) Reynolds lubrication equation using the linear Maxwell (viscoelastic) constitutive equation and a slip boundary condition. We study the deformation of the viscoelastic lubricant due to laser heating under the influence of thermocapillary stress and disjoining pressure.

Subsequently, in Chapter 4, we use this modified lubrication equation for the viscoelastic lubricant to develop a model that predicts the media-to-head lubricant transfer during HAMR. We investigate the effect of lubricant properties such as viscoelasticity, lubricant

type (Zdol vs Ztetraol), molecular weight, slip length, disjoining pressure, and HAMR design parameters such as head/media temperature, lubricant thickness and laser FWHM on the lubricant transfer. Finally, we also study the recovery of the viscoelastic lubricant after the HAMR laser is removed.

In Chapter 5, we present a numerical model to simulate the head temperature due to heat transfer across a closing nanoscale gap between the head and the media (non-rotating). Our model employs a spacing-dependent heat transfer coefficient due to the combined effects of air conduction and wave-based phonon conduction theory. We compare our simulations with static touchdown experiments performed with a TFC slider resting on three different media (Si, magnetic disks with AlMg, and glass substrates). With the introduction of intermolecular van der Waals forces between the head and the media, we demonstrate a good quantitative match with experiments for all of the media materials tested, at different initial head-media spacings and in different environments (air, vacuum).

In Chapter 6, we develop a numerical model to predict the slider temperature profile and the fly height for a flying slider over a rotating disk. We compare our simulations with touchdown experiments performed with a flying TFC slider. To accurately predict the heat transfer and fly height at near-contact, we incorporate the effects of disk temperature rise, intermolecular adhesion & contact forces, air & phonon conduction heat transfer and friction heating in our model. We investigate the impact of each of these features on head temperature during flying. We find that simulation with all these features agrees well with the experiment.

In Chapter 7, we develop a numerical model to predict the temperature profile of the media and its resultant thermal protrusion during HAMR laser heating. Chapter 8 gives a final summary of the research presented in this dissertation.

Chapter 2

Viscous Model for Disk-to-Head Lubricant Transfer During HAMR

2.1 Introduction

One of the tribological challenges in HAMR is the formation of write-induced head contamination at the near field transducer (NFT) [29]. This contamination forms only when the head NFT is energized and the media is heated to its Curie temperature. Kiely et. al. [29] reported measurements of contamination thickness as a function of write time for a variety of different heads in different operating conditions. They observed that the contamination begins very quickly after the laser power is turned on (< 1 second) and grows over time until the contamination height reaches the head-disk clearance. Once the head contamination contacts the media surface, the disk motion generates a smear down-track of the NFT.

One possible mechanism that has been proposed for HAMR contamination is lubricant desorption from the disk and adsorption on the head through thermodynamic driving forces [29]. During HAMR, the media is locally heated to its Curie temperature ($\sim$ 500 °C). The head also locally reaches a high temperature due to heat dissipation in the NFT and back-heating from the disk, however, the peak temperature of the head is lower than that of the disk ($\sim$ 310 °C) [29]. This temperature difference causes the lubricant to evaporate from the disk and condense on the relatively cooler head. The lubricant acts as a carrier, causing a continuous deposition of contaminants originating from the media at the head NFT. Alternatively, the contaminants themselves may be desorbed and adsorbed by a similar thermodynamic mechanism. Either way, once the contaminants are deposited on the NFT, they possibly undergo thermo-chemical reactions (pyrolysis) at high temperature, leaving a non-volatile residue on the NFT.

Xiong et. al. [30] also reported deposition of materials on the head after HAMR writing. They observed that after the NFT was turned off and the head-media temperature difference was inverted, material was transfered from the head back to the media. This indicates that the temperature difference between the head and the media is one important mechanism for

the material transfer. However, they also reported that the trace of the head deposits lasts about 1 μs, which is close to the mechanical transient of the NFT protrusion, but longer than the thermal response of the head and media. Thus mechanical interaction is an additional mechanism leading to material transfer from the media to the head.

Understanding the mechanism of disk to head lubricant and contaminant transfer is crucial in order to eliminate or control its effect and to develop reliable HAMR drives. There have been several studies on transfer of perfluoropolyether (PFPE) lubricant from the disk to the slider due to evaporation/condensation for non-HAMR drives [40] [41] and HAMR drives [42] [43]. Ma and Liu [42] studied the effect of disk temperature and lubricant molecular weight on lubricant depletion and head transfer in HAMR. However, their model assumed a uniform disk lubricant film and a uniform temperature distribution, ignoring the effect of spatial temperature gradient on lubricant evolution. Yang et. al. [43] reported lubricant accumulation on the media surface after the laser was turned off. They proposed a simple lubricant equilibrium model assuming uniform temperatures and lubricant thicknesses to explain their results. Existing continuum models for disk-to-head lubricant transfer by evaporation/condensation have involved over-simplifications and have not been able to quantitatively predict the actual disk-to-head lubricant transfer process in HAMR. Wu [44] developed a model to predict the lubricant transfer from the disk to the head considering coupled evaporation condensation and migration dynamics. In that study, a model was proposed that can predict the lubricant partial vapor phase distribution within the air bearing layer, which is imperative to quantitatively describe the disk to slider lubricant transfer. However, that study was performed for non-HAMR drives and the evolution of the disk lubricant profile was not considered.

There have been several studies on lubricant transfer from the disk to the slider caused by mechanical interactions. Ambekar et. al. [45] reported experimental data suggesting the existence of a critical clearance between the head and disk below which significant lubricant transfer takes place. They explained this phenomenon through a disjoining pressure model that accounts for the influence of the slider to predict the onset of dewetting. Other studies have also used similar disjoining pressure models considering disk-lubricant, slider-lubricant and lubricant-lubricant interactions in order to explain lubricant instability at low clearances [46] [47] [48] [49]. Both temperature difference driven evaporation/condensation and molecular interactions based mechanical transfer are important mechanisms causing lubricant transfer in HAMR and the influence of both of these must be considered in order to predict the lubricant transfer process.

The deformation of the disk lubricant film during HAMR laser heating has been well studied in the literature. Viscous continuum models and molecular dynamics models have been developed to predict the lubricant profile under the influence of the driving forces including surface tension gradient, disjoining pressure, evaporation and thin film viscosity [32] [31] [50] [33]. While the effects of dispersive and polar disjoining pressure for different PFPE lubricants have been studied [35], the effects of the slider and slider lubricant on the disjoining pressure have not been modeled. The migration of the slider lubricant film caused by air shear stress and pressure has also been studied [51]. However, to our knowledge, there

is no existing continuum model that considers the deformation of the disk lubricant film under HAMR heating while predicting the lubricant transfer process. The evolution of the deposited lubricant film on the slider under the temperature gradient at the NFT has also not been studied.

During HAMR writing, there is a continuous circulation of lubricant between the disk, the air bearing and the slider. The depletion and deformation of disk lubricant, diffusion and convection of the vapor phase and the evolution of the deposited slider lubricant are strongly coupled and must be modeled simultaneously to understand the physics of the transfer process. In this chapter, we present a viscous continuum model that predicts the evolution of the disk lubricant film, the lubricant vapor phase in the air bearing and the slider lubricant layer during HAMR writing. We investigate the effects of media temperature, head temperature and initial lubricant thickness on the lubricant transfer process. We also study the effects of slider-lubricant and lubricant-lubricant molecular interactions on the disk-to-head lubricant transfer.

2.2 Continuum Mechanics vs Molecular Dynamics

The first question that needs to be answered in order to study the behavior of the nanoscale lubricant films is if continuum mechanics can actually be used to describe the lubricant flow. This question has been addressed extensively in literature by Mate et al. [52], Karis et al. [53] and Scarpulla et al. [54]. These references studied the flow of molecularly thin lubricant films under air shear and found that the flow can still be described by continuum theory with the adoption of an effective viscosity, which is dependent on the lubricant film thickness. For example, Karis et al. measured lubricant spin-off rates from rotating disks at high RPMs (5000-10000 RPM) due to air shear. They found that the spin-off process can be well-modeled by the traditional viscous Reynolds lubrication equation, with the adoption of a film-thickness dependent effective viscosity.

Lubricant transfer at the head-disk interface has been studied using molecular dynamics (MD) [55–58]. Dai et al. predicted the formation of a lubricant bridge between the disk and the slider due to HAMR heating using MD simulations [55]. Marchon & Saito [33] presented fluid dynamics simulation results of unfunctionalized lubricant Z on the disk under HAMR laser heating that agreed well with much more computationally expensive MD simulations. Continuum mechanics offers a cost-effective yet accurate method to study lubricant behavior with realistic domain sizes and simulation times.

2.3 Viscous Model for Disk-to-Head Lubricant Transfer

During HAMR writing, the media is locally heated to its Curie Temperature ($T_{max,d} \sim 500^oC$). The high spatial temperature gradient (∇T_d) causes the lubricant film on the disk

(thickness h_d) to deform and evaporate. Lubricant evaporation causes the partial pressure of the lubricant vapor in the air bearing, p_v to rise. Some of this lubricant vapor condenses on the relatively cooler slider surface (maximum head temperature $T_{max,s} \sim 310^oC$) [29], depositing a thin lubricant film of thickness h_s. The spatial temperature gradient on the slider (∇T_s) causes this deposited lubricant film to deform. A schematic of this disk to slider lubricant transfer process is shown in Figure 2.1. Thus, we have three unknowns in this problem - $h_d(x, y, t)$, $h_s(x, y, t)$ and $p_v(x, y, t)$. In this study we apply this simulation tool to the PFPE lubricant Zdol 2000.

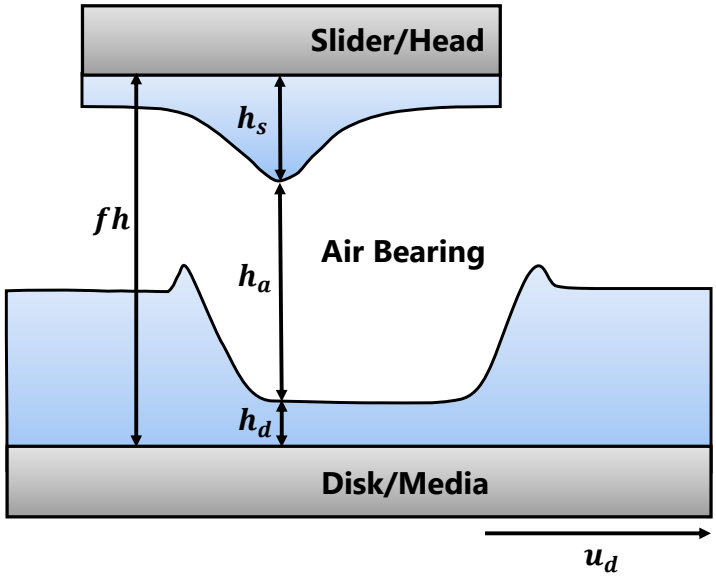

Figure 2.1: HAMR Lubricant Transfer Schematic: Disk Lubricant of thickness $h_d(x, y, t)$ is subjected to a 20 nm FWHM laser spot. The disk lubricant evaporates to form vapor having partial pressure $p_v(x, y, t)$ in the HDI. The vapor condenses on the slider to form a film of thickness $h_s(x, y, t)$.

Viscous Lubrication Theory

The flow of the disk lubricant film can be modelled using viscous lubrication theory. We consider the problem of a thin incompressible lubricant film of thickness $h_d(x, y, t)$ on a flat substrate (disk), moving at a constant linear speed u_d. The co-ordinate system is defined such that the z axis is along the lubricant thickness and the x axis is along the direction of the disk velocity. The top surface of the lubricant ($z = h_d$) is free to evolve under the influence of external shear stress $\boldsymbol{\tau_d}(x, y, t) = \tau_{x,d}\boldsymbol{e_x} + \tau_{y,d}\boldsymbol{e_y}$ and external pressure $p_{ext}(x, y, t)$ (Figure 2.2).

The fundamental assumption of lubrication theory is that the characteristic dimension in the thickness direction h_0 is much smaller than the characteristic dimension in the length

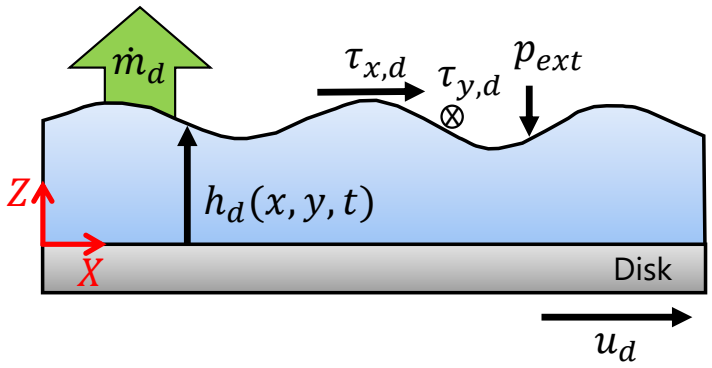

Figure 2.2: HAMR Disk Lubricant Deformation Schematic: Lubricant of thickness $h_d(x, y, t)$ is coated on the disk, which moves at a constant linear speed u_d. The top surface of the lubricant is free to evolve under the influence of external shear stress $\boldsymbol{\tau_d} = \tau_{x,d}\boldsymbol{e_x} + \tau_{y,d}\boldsymbol{e_y}$ and external pressure p_{ext}. Some lubricant is removed from the film via evaporation ($\dot{m}_d$).

and width directions, L (i.e. $h_0 \ll L$). Additionally, the inertial terms in the Navier Stokes equations are neglected compared to the viscous terms (i.e. low Reynolds number flow) and the effect of gravity is ignored.

With the lubrication approximation, the traction boundary condition at $z = h_d$ can be expressed as:

$$\mu_d \frac{\partial v_x}{\partial z}\bigg|_{z=h_d} = \tau_{x,d} \quad \mu_d \frac{\partial v_y}{\partial z}\bigg|_{z=h_d} = \tau_{y,d} \quad p_d\Big|_{z=h_d} = p_{ext} \tag{2.1}$$

Here v_x, v_y are the lubricant velocity components along x, y, μ_d is the effective lubricant viscosity and p_d is the lubricant pressure. Further, we assume the no-slip and no-penetration boundary condition for the lubricant velocity components v_x, v_y, v_z at $z = 0$

$$v_x|_{z=0} = u_d \quad v_y|_{z=0} = 0 \quad v_z|_{z=0} = 0 \tag{2.2}$$

Although PFPE lubricants exhibit viscoelastic behavior [6] and may undergo slippage on the surface of the disk at high shear strains, as a first attempt to understand disk-to-head transfer, we employ a purely viscous model with the no-slip boundary condition in this chapter. The effects of viscoelasticity and slippage will be explored in subsequent Chapters 3 and 4.

With these approximations, the Navier Stokes equations simplify to: [59, 60]

$$\begin{aligned} \frac{\partial p_d}{\partial x} &= \frac{\partial}{\partial z}\left(\mu_d \frac{\partial v_x}{\partial z}\right) \\ \frac{\partial p_d}{\partial y} &= \frac{\partial}{\partial z}\left(\mu_d \frac{\partial v_y}{\partial z}\right) \\ \frac{\partial p_d}{\partial z} &= 0 \end{aligned} \tag{2.3}$$

Further, integrating the continuity equation for incompressible fluids $\nabla \cdot \boldsymbol{v} = 0$ across the film thickness h_d, we get the following equation (a derivation can be found in Ref. [59]).

$$\frac{\partial h_d}{\partial t} + \frac{\partial}{\partial x}\left(\int_0^{h_d} v_x dz\right) + \frac{\partial}{\partial y}\left(\int_0^{h_d} v_y dz\right) + \frac{\dot{m}_d}{\rho_l} = 0 \tag{2.4}$$

Here ρ_l is the constant lubricant density and $\dot{m}_d$ is the mass flux due to evaporation from the disk. Integrating Eq. (2.3) using the boundary conditions (2.1), (2.2), we obtain the following velocity profiles:

$$\begin{aligned} v_x &= \frac{1}{\mu_d}\frac{\partial p_d}{\partial x}\left(\frac{1}{2}z^2 - h_d z\right) + \frac{\tau_{x,d}}{\mu_d}z + u_d \\ v_y &= \frac{1}{\mu_d}\frac{\partial p_d}{\partial y}\left(\frac{1}{2}z^2 - h_d z\right) + \frac{\tau_{y,d}}{\mu_d}z \end{aligned} \tag{2.5}$$

Substituting these velocity profiles into Eq. (2.4), we arrive at the following equation: [32, 59, 60]

$$\frac{\partial h_d}{\partial t} + u_d\frac{\partial h_d}{\partial x} + \frac{\partial}{\partial x}\left[-\frac{h_d^3}{3\mu_d}\frac{\partial p_d}{\partial x} + \frac{h_d^2}{2\mu_d}\tau_{x,d}\right] + \frac{\partial}{\partial y}\left[-\frac{h_d^3}{3\mu_d}\frac{\partial p_d}{\partial y} + \frac{h_d^2}{2\mu_d}\tau_{y,d}\right] + \frac{\dot{m}_d}{\rho_l} = 0 \tag{2.6}$$

Eq. (2.6) is the governing equation for the unknown disk lubricant thickness h_d and is commonly known as the Reynolds lubrication equation. It is worthwhile to note that with the lubrication approximation we assume that the lubricant pressure $p_d \equiv p_d(x, y, t)$ is uniform along the film thickness (i.e. $\frac{\partial p_d}{\partial z} = 0$). Thus, using Eq. (2.1), the lubricant pressure is obtained as $p_d(x, y, t) = p_{ext}$.

Surface Tension

A liquid molecule in the interior experiences intermolecular interactions from other liquid molecules (cohesive forces) from all possible directions. However, a liquid molecule on the surface experiences cohesive intermolecular interactions only from one side (bottom side). On the top side, it experiences intermolecular interactions from air and/or vapor molecules (adhesive forces). Hence, in order to bring a liquid molecule from the interior to the surface an additional energy γ per unit added area of the surface needs to be provided. For liquids, this surface energy may be interpreted as a tangential surface force per unit length, called surface tension.

The resultant stress on the lubricant due to surface tension can be decomposed into two components: a component that acts tangential to the lubricant surface and occurs due to spatial variation of surface tension (Marangoni stress) and a component that acts normal to the lubricant surface and occurs due to the curvature of the surface (Laplace pressure) [61].

The Marangoni stress occurs due to any spatial non-uniformity of surface tension. As the temperature increases, cohesive forces decrease due to an increase of molecular thermal

activity. Hence, surface tension of most liquids decreases with temperature. During HAMR laser heating, the spatial temperature gradient on the lubricant surface causes the surface tension to vary spatially. In this case, the Marangoni stress is also called "thermocapillary shear stress" and can be expressed as:

$$\boldsymbol{\tau_d} = \nabla\gamma - (\nabla\gamma \cdot \boldsymbol{n})\boldsymbol{n} \tag{2.7}$$

With the quasi-parallel film assumption ($|\nabla h| \ll 1$,$\boldsymbol{n} \approx \boldsymbol{e_z}$) and additionally assuming that the surface tension decreases linearly with temperature, the resultant shear stress on the disk lubricant can be expressed as:

$$\boldsymbol{\tau_d} = \tau_{x,d}\boldsymbol{e_x} + \tau_{y,d}\boldsymbol{e_y} = \frac{\partial\gamma}{\partial x}\boldsymbol{e_x} + \frac{\partial\gamma}{\partial y}\boldsymbol{e_y} = -c\left(\frac{\partial T_d}{\partial x}\boldsymbol{e_x} + \frac{\partial T_d}{\partial y}\boldsymbol{e_y}\right) \tag{2.8}$$

Here, $c \equiv -\frac{d\gamma}{dT}$ is assumed to be constant and equal to 0.06 $mN/(m^oC)$ for Zdol 2000 [32]. We note that in general the resultant shear stress on the lubricant $\boldsymbol{\tau_d} = \tau_{x,d}\boldsymbol{e_x} + \tau_{y,d}\boldsymbol{e_y}$ in Eq. (2.6) also has a contribution due to shear stress caused by the air bearing flow. However, we ignore the effect of air shear stress compared to the thermocapillary stress in this study.

The Laplace pressure p_{lap} contributes to the net external pressure applied to the lubricant p_{ext} and is given by the following expression:

$$p_{lap}\boldsymbol{n} = (-\gamma\nabla \cdot \boldsymbol{n})\boldsymbol{n} = (\gamma\nabla^2 h_d)\boldsymbol{n} \tag{2.9}$$

Previous studies by Dahl and Bogy [32] and Sarabi and Bogy [35] have shown that the Laplace pressure has a negligible impact on lubricant evolution during HAMR laser heating, particularly for thin lubricant films ($\leq$ 1.2 nm). Hence, we ignore the effect of Laplace pressure on the lubricant evolution in this study.

Disjoining Pressure

Effectively, intermolecular forces (such as van der Waals and electrostatic forces) have a finite range of influence r, beyond which these forces become negligibly small. For nanoscale liquid films, as the film thickness becomes comparable to r (see Figure 2.3), the molecules in the solid substrate interact with the lubricant molecules resulting in an additional normal force on a surface element of the lubricant (additional to the force due to Laplace pressure (Eq. (2.9)) and ambient gas pressure, p_{gas}). This extra force is the resultant of all intermolecular interactions in the gas-liquid-solid system acting on the area element dA and is defined as the disjoining force. This force acts normal to the interface, is directly proportional to the surface area dA and depends on the film thickness h_d. Thus, the disjoining force can be expressed as $\Pi_d(h_d)\boldsymbol{n}dA$. Here $\Pi_d(h_d)$ is defined as the disjoining pressure. In general, Π_d could be positive (solid repels the lubricant-air interface) or negative (solid attracts the lubricant-air interface) [62]. Balancing the normal forces on the surface element dA, the

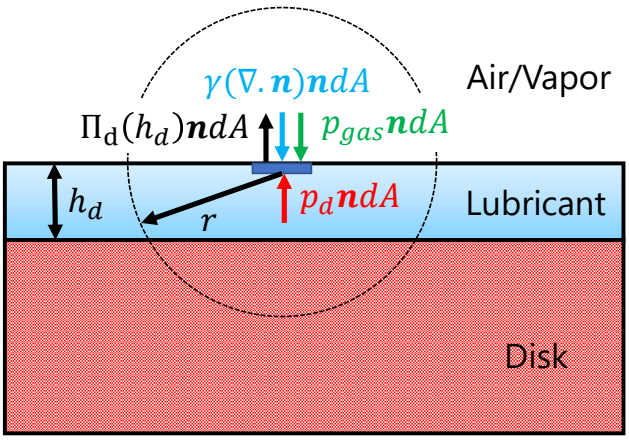

Figure 2.3: The next external pressure on the lubricant p_{ext} has contributions due to the ambient gas pressure p_{gas}, the Laplace pressure $\gamma\nabla\cdot\boldsymbol{n}$ and the Disjoining pressure Π_d. Disjoining pressure is an equivalent pressure acting on a lubricant surface element due to the resultant of all intermolecular interactions in the gas-liquid-solid system

lubricant pressure p_d in Eq. (2.6) is obtained as:

$$\begin{aligned} p_d = p_{ext} &= p_{gas} - \Pi_d(h_d) + \gamma\nabla\cdot\boldsymbol{n} \\ &= p_{gas} - \Pi_d(h_d) - \gamma\nabla^2 h_d \end{aligned} \tag{2.10}$$

Eq. (2.10) is known as the augmented Young-Laplace equation, since it contains a supplementary pressure (disjoining pressure) which augments the classical Young-Laplace equation ($p_d = p_{gas} + \gamma\nabla\cdot\boldsymbol{n}$).

As indicated by Eq. (2.10), the external normal pressures applied to the lubricant film are the air bearing pressure, disjoining pressure and laplace pressure. Of these, the disjoining pressure has a dominant effect on lubricant diffusion. The timescale of lubricant deformation during HAMR is of the order of ns, while the effect of the air bearing pressure (p_{gas}) is expected to be on the order of seconds [63] and can be ignored [31]. As noted previously, the effect of Laplace pressure on the lubricant film evolution is also small for thin films. Thus the lubricant pressure p_d in Eq. (2.6) is obtained as:

$$p_d = -\Pi_d(h_d) \tag{2.11}$$

For a one-component liquid, the disjoining pressure may be determined as the derivative of the free energy per unit area of a thin layer, which arises from the effect of surface forces. Based on this definition, some researchers have tried to obtain appropriate expressions for the disjoining pressure of PFPE lubricants [64] [65] according to the following equation:

$$\Pi_d(h_d) = -\frac{\partial\gamma_d^d}{\partial h_d} - \frac{\partial\gamma_d^p}{\partial h_d} = \Pi_d(h_d)^d + \Pi_d(h_d)^p = \frac{A_{VLS}}{6\pi(h_d+d_0)^3} + \Pi_d(h_d)^p \tag{2.12}$$

Here we consider two components of disjoining pressure and use the mischaracterizing nomenclature common in hard drive lubricant literature [46] - dispersive Π_d^d and polar Π_d^p, based on the corresponding components of the thin film surface energy γ_d^d and γ_d^p. The dispersive disjoining pressure Π_d^d is a consequence of van der Waals interactions and has a $1/h^3$ dependence. Here A_{VLS} is the Hamaker constant for the vapor-liquid-solid system. d_0 is a constant introduced to account for the molecular effect of the finite size of the atoms and molecules within the lubricant film. The oscillating polar component Π_d^p is due to structural effects or non-van der Waals interactions introduced by the functional end-groups and is typically represented by a polynomial expansion. The coefficients of dispersive disjoining pressure ($A_{VLS} = 4.59 \times 10^{-20}$ J, $d_0 = 0.172$ nm) and polar disjoining pressure (curve-fitting parameters for polynomial expansion) of Zdol 2000 can be found in Ref. [35]. These coefficients are based on the methodology described by Karis and Tyndall [64] and the experimental data of surface energy of unannealed Zdol 2000 given by Tyndall et. al. [65].

Some researchers [46] have questioned the assumptions made in the widely used contact angle method used to determine disjoining pressure in Refs. [64], [65]. However, in the absence of an accurate method for measuring disjoining pressure for actual lubricant/disk systems, we use the contact angle measurements in Ref. [65] in this study.

At nanometer scale head-disk clearances, the disk lubricant disjoining pressure is also influenced by the presence of the slider and the lubricant layer on the slider. Several previous works [66], [45] and [46] consider the influence of the slider on the disk lubricant disjoining pressure, while ignoring the liquid-liquid interactions. However, as the amount of lubricant accumulation on the slider increases, the liquid-liquid interactions can no longer be neglected. The resulting expression for the disk lubricant disjoining pressure is given by: [67], [68], [69]

$$\Pi_d(h_d, h_s) = \frac{A_{VLS}}{6\pi(h_d + d_0)^3} + \Pi_d(h_d)^p + \frac{A_{VLS}}{6\pi(fh - h_d - d_0)^3} + \frac{A_{LVL}}{6\pi(fh - h_d - h_s - 2d_0)^3} \quad (2.13)$$

Here A_{LVL} is the Hamaker constant for the liquid-liquid interactions through vapor. In this study, we assume that $A_{LVL} = 3 \times 10^{-20}$ J [70] [66]. A detailed derivation of Eq. (2.13) can be found in Ref. [68]. It is worthwhile to note that in the characterization of disjoining pressure in Eq. (2.13), we define Hamaker constants such that $A_{VLS} > 0$ and $A_{LVL} > 0$. Defining A_{SVL} as the Hamaker constant for solid-liquid interactions through vapor and assuming $A_{SVL} \approx A_{VLS} + A_{LVL}$ [66], Eq. (2.13) can be equivalently expressed as:

$$\begin{aligned} \Pi_d(h_d, h_s) = &\left[\frac{A_{VLS}}{6\pi(h_d + d_0)^3} + \Pi_d(h_d)^p\right] + \left[\frac{A_{SVL}}{6\pi(fh - h_d - d_0)^3}\right] \\ &+ \left[\frac{A_{LVL}}{6\pi(fh - h_d - h_s - 2d_0)^3} - \frac{A_{LVL}}{6\pi(fh - h_d - d_0)^3}\right] \end{aligned} \quad (2.14)$$

In Eq. (2.14), the first term represents the disjoining pressure of the disk lubricant due to van der Waals and polar interactions with the disk, the second term represents the influence of the slider on the disk lubricant disjoining pressure and the third term represents the influence of the slider lubricant film on the disk lubricant disjoining pressure. We note

that the expression for disjoining pressure found in Refs. [66], [45] and [46] is the same as Eq. (2.14), if we ignore the last term (liquid-liquid interaction).

Thin Film Viscosity

As noted in Section 2.2, viscous lubrication theory can be used to model the flow of the nanoscale lubricant film on the disk, provided an effective film-thickness dependent viscosity is employed. Intermolecular forces between paricles in a fluid resist the shearing motion of the fluid and this resistance causes viscosity. As the temperature increases, the strength of intermoelecular forces in a liquid decreases due to an increase in molecular thermal activity. Hence, the viscosity of most liquids decreases with an increase in temperature. Karis [53] applied Eyring's rate theory to develop a thin film viscosity model for hard disk drive lubricants including temperature and film thickness dependence and gave the following equation:

$$\mu_d(h_d) = \frac{N_A h_P}{V_l} exp\left(\frac{\Delta E_{vis}(h_d) - T_d \Delta S_{vis}(h_d)}{RT_d}\right) \tag{2.15}$$

where N_A is Avogadro's number, h_P is Planck's constant, V_l is the molar volume of the lubricant, $\Delta E_{vis}(h_d)$ is the film thickness dependent flow activation energy, $\Delta S_{vis}(h_d)$ is the film thickness dependent flow activation entropy, R is the universal gas constant and T_d is the disk lubricant temperature. We use the same $\Delta E_{vis}(h_d)$ and $\Delta S_{vis}(h_d)$ values as those found in Ref. [53] for Zdol [32].

Evaporation

Dahl and Bogy [32] used the method of Karis [6] to calculate the bulk vapor pressure of Zdol $p_{vap,\infty}(T, M_w)$ with the Clapeyron equation and ideal gas law. With the bulk vapor pressure known, the equilibrium thin film vapor pressure is determined using the following expression [32, 59, 71]:

$$\frac{p_{vap,film}(h_d, h_s)}{p_{vap,\infty}} = exp\left(\frac{M_w}{\rho_l RT_d}[-\pi_d(h_d, h_s)]\right) \tag{2.16}$$

Next, the net evaporation rate is determined using the Hertz-Knudsen-Langmuir model [72] as:

$$\dot{m}_d(h_d, h_s, p_v) = \alpha\sqrt{\frac{M_w}{2\pi RT_d}}(p_{vap,film}(h_d, h_s) - p_v) \tag{2.17}$$

where $\dot{m}_d$ is the net evaporation mass flux from the disk, M_w is the lubricant molecular weight, R is the molar universal gas constant, T_d is the disk lubricant temperature and α is the accommodation constant (assumed to be 1 in this study). $p_{vap,film}$ is the equilibrium thin film vapor pressure and p_v is the partial pressure of the lubricant vapor in the air bearing. Previous works on lubricant deformation under HAMR conditions [32] [35] [31] [50] have assumed p_v to be 0. However, when the media is heated to its Curie temperature, significant evaporation of the lubricant is expected to occur. As a result, the partial pressure of the

lubricant vapor in the air bearing can not be ignored and must be studied using a separate evolution equation. This equation will be discussed in the subsequent section "Lubricant Vapor in the Air Bearing".

Governing Equation for the Disk Lubricant

The governing equation for the disk lubricant can be obtained by substituting Eqs. (2.8), (2.11), (2.13), (2.15) and (2.17) in Eq. (2.6):

$$\frac{\partial h_d}{\partial t} + u_d \frac{\partial h_d}{\partial x} + \frac{\partial}{\partial x}\left[\frac{h_d^3}{3\mu_d}\frac{\partial \pi_d}{\partial x} - \frac{h_d^2}{2\mu_d} c \frac{\partial T_d}{\partial x}\right] + \frac{\partial}{\partial y}\left[\frac{h_d^3}{3\mu_d}\frac{\partial \pi_d}{\partial y} - \frac{h_d^2}{2\mu_d} c \frac{\partial T_d}{\partial y}\right] + \frac{\dot{m}_d}{\rho_l} = 0 \quad (2.18)$$

We use the same non-dimensionalization scheme as Dahl and Bogy [32].

$$\begin{aligned} h_d* = h_d h_{0,d} \quad x* = xL \quad y* = yL \\ \mu_d* = \mu_0 \mu_d \quad T_d* = T_d \Delta T_d + T_0 \end{aligned} \quad (2.19)$$

Here $h_{0,d}$ is the initial disk lubricant thickness, L is the disk temperature profile FWHM, T_0 is the ambient temperature, ΔT_d is the maximum prescribed disk temperature rise $T_{max,d} - T_0$ and $\mu_0 = \mu(T_0, h_{0,d})$. This choice of non-dimensional variables implies the following scales and coefficients:

$$\begin{aligned} t* = t t_s \quad \pi_d* = \pi_d p_s \quad t_s \equiv \frac{2\mu_0 L^2}{h_{0,d} c \Delta T_d} \\ p_s \equiv \frac{3}{2}\frac{c\Delta T_d}{h_{0,d}} \quad C_u \equiv \frac{2\mu_0 L u_d}{h_{0,d} c \Delta T_d} \quad S \equiv \frac{2\mu_0 L^2 \dot{m}_d}{h_{0,d}^2 c \Delta T_d \rho_l} \end{aligned} \quad (2.20)$$

We now switch to a notation where quantities with an asterisk are dimensional and quantities without an asterisk are non-dimensional. The final non-dimensional governing equation for the disk lubricant is:

$$\frac{\partial h_d}{\partial t} + C_u \frac{\partial h_d}{\partial x} + \frac{\partial}{\partial x}\left[\frac{h_d^3}{\mu_d}\frac{\partial \pi_d}{\partial x} - \frac{h_d^2}{\mu_d}\frac{\partial T_d}{\partial x}\right] + \frac{\partial}{\partial y}\left[\frac{h_d^3}{\mu_d}\frac{\partial \pi_d}{\partial y} - \frac{h_d^2}{\mu_d}\frac{\partial T_d}{\partial y}\right] + S_d = 0 \quad (2.21)$$

The initial condition is a uniform film of lubricant of prescribed thickness $h_{0,d}$. We use Neumann boundary conditions on the ends of our domain.

Governing Equation for the Slider Lubricant

Similarly, the final non-dimensional governing equation for the slider lubricant can be expressed as:

$$\frac{\partial h_s}{\partial t} + \frac{\partial}{\partial x}\left[\frac{h_s^3}{\mu_s}\frac{\partial \pi_s}{\partial x} - \frac{h_s^2}{\mu_s}\frac{\partial T_s}{\partial x}\right] + \frac{\partial}{\partial y}\left[\frac{h_s^3}{\mu_s}\frac{\partial \pi_s}{\partial y} - \frac{h_s^2}{\mu_s}\frac{\partial T_s}{\partial y}\right] + S_s = 0 \quad (2.22)$$

The initial condition is a uniform film of lubricant of thickness $h_{0,s}$. We use Neumann boundary conditions on the ends of our domain. It is worthwhile to highlight that h_s is nondimensionalized with respect to $h_{0,d}$ and T_s is non-dimensionalized with respect to ΔT_d. Also, we assume that the FWHM of disk and slider temperature profiles are the same and equal to L.

Lubricant Vapor in the Air Bearing

Consistent with the lubrication approximation, we assume that the density of the lubricant vapor in the air bearing ρ_v is independent of the normal co-ordinate z, i.e., $\rho_v \equiv \rho_v(x, y)$. The governing equation for the lubricant vapor can be obtained by integrating the continuity equation along the normal co-ordinate z and applying Fick's Law of Diffusion [44].

$$\frac{\partial}{\partial t}(\rho_v h_a) + \frac{\partial}{\partial x}(\rho_v q_x) + \frac{\partial}{\partial y}(\rho_v q_y) = \frac{\partial}{\partial x}\left(D h_a \frac{\partial \rho_v}{\partial x}\right) + \frac{\partial}{\partial y}\left(D h_a \frac{\partial \rho_v}{\partial y}\right) + \dot{m}_d + \dot{m}_s \quad (2.23)$$

In this equation, $h_a(h_s, h_d) \equiv (fh - h_s - h_d)$ is the height of the air bearing where fh is the constant head-disk spacing at the NFT (Refer Figure 2.1). $q_x \equiv \int_{h_d}^{h_d+h_a} v_{a,x} dz$ and $q_y \equiv \int_{h_d}^{h_d+h_a} v_{a,y} dz$ are the volume flow rates per unit length in the x and y directions, obtained by integrating the air bearing velocity $v_{a,x}$ and $v_{a,y}$ in the z direction across the air bearing clearance. D is the lubricant vapor diffusivity in air and $\dot{m}_d$ and $\dot{m}_s$ are the net evaporation mass fluxes from the disk and slider lubricant films respectively. Eq. (2.23) also assumes that the lubricant vapor in air is a dilute mixture so that the binary mixture velocity can be approximated by the air bearing velocity $v_{m,x} \approx v_{a,x}$ and $v_{m,y} \approx v_{a,y}$ and that the mixture density ρ_m is approximately constant over the scale on which ρ_v varies.

The first term in Eq. (2.23) models the unsteady lubricant vapor density change and dynamic air bearing height change. The next two terms on the LHS of Eq. (2.23) model the vapor convection effect due to the air bearing velocity. The effect of lubricant vapor diffusion in the air bearing layer is modeled by the first two terms on the RHS of (2.23). Finally, lubricant evaporation/condensation from the disk/slider is modeled by the last two terms of Eq. (2.23).

In this study, we assume that the effects of the lubricant vapor on the air bearing pressure, temperature and velocity can be neglected. Also, the lubricant as well as air bearing temperature is simply assumed to be equal to the average of the disk and slider temperatures $T_v \equiv (\frac{T_s+T_d}{2})$. Finally, the lubricant vapor density and partial pressure are assumed to be related by the ideal gas law:

$$P_v = \frac{\rho_v R T_v}{M_w} \quad (2.24)$$

where R is the molar universal gas constant and M_w is the lubricant molecular weight.

Convection and Diffusion

The lubricant convection model in Eq. (2.23) requires the air bearing velocity profiles in the x and y directions near the location of the NFT. Theoretically, this velocity profile can be obtained from an air bearing model for HAMR like CMLAir HAMR [73, 74]. However, the air bearing model in [73, 74] is rather coarsely meshed near the NFT location. Hence, due to the lack of accurate air velocity profiles very close to the NFT, we assume the following simple model for volume fluxes q_x and q_y:

$$q_x = u_d(fh - h_{0,d} - h_{0,s}) \quad q_y = 0 \tag{2.25}$$

Karis [6] used the Hirschfelder approximation [75] to obtain the lubricant vapor phase diffusion coefficient:

$$D = 1.858 \times 10^{-4} \left(\frac{1}{M_w} + \frac{1}{M_a} \right)^{0.5} \frac{T_v^{1.5}}{P_a \sigma_i \Omega} \tag{2.26}$$

where M_a and M_w are the air and lubricant molecular weights and P_a is the air bearing pressure. Expressions for collision diameter σ_i and collision integral Ω can be found in [6].

Governing Equation for the Lubricant Vapor

We use the following non-dimensionalization for the lubricant vapor equation (2.23):

$$\begin{gathered} \rho_v* = \rho_v \rho_l \quad h_a* = h_a h_{0,d} \quad q_x* = q_x q_0 \quad q_y* = q_x q_0 \\ D* = D D_0 \quad q_0 \equiv \frac{L h_{0,d}}{t_s} \quad C_D \equiv \frac{t_s D_0}{L^2} \end{gathered} \tag{2.27}$$

Here ρ_l is the density of the liquid lubricant and D_0 is the diffusivity at ambient temperature T_0 and pressure p_0 ($D_0 \equiv D(T_0, p_0)$). The spatial and temporal non-dimensionalization is the same as that for the disk/slider lubricant Eq. (2.19) and (2.20). We now switch to a notation where quantities with an asterisk are dimensional and quantities without an asterisk are non-dimensional. The final non-dimensional governing equation for the lubricant vapor is:

$$\frac{\partial}{\partial t}(\rho_v h_a) + \frac{\partial}{\partial x}(\rho_v q_x) + \frac{\partial}{\partial y}(\rho_v q_y) = \frac{\partial}{\partial x}\left(C_D D h_a \frac{\partial \rho_v}{\partial x} \right) + \frac{\partial}{\partial y}\left(C_D D h_a \frac{\partial \rho_v}{\partial y} \right) + S_d + S_s \tag{2.28}$$

Numerical Scheme

Equations (2.21), (2.22) and (2.28) are three coupled partial partial differential equations in the three unknows h_s, h_d and ρ_v (or equivalently P_v through (2.24)). Equations (2.22) and (2.28) are discretized using a finite volume method (Hybrid Scheme) [76]. For the disk lubricant equation (2.21), we follow the method used by Dahl and Bogy [32] - the non-advective part of the equation is discretized using the Hybrid Scheme and the advective part is solved using the Cubic Interpolation Spline (CIP) scheme [77], [78]. The resulting set of non-linear, coupled algebraic equations are solved iteratively to obtain the three solution profiles.

2.4 Results

Lubricant Transfer during HAMR

For the baseline simulation, we assume an initially uniform film of Zdol 2000 (M_w = 2 kg/mol) of thickness $h_{0,d}$ = 1.2 nm on the disk. The ambient conditions are assumed to be T_0 = 25 °C and p_0 = 101325 Pa. The disjoining pressure experimental data is valid in the thickness range 0.2-2 nm, hence we assume the initial lubricant thickness on the slider ($h_{0,s}$) to be 0.2 nm. We prescribe a Gaussian temperature profile with a peak of 500 °C and FWHM of 20 nm on the disk. The slider temperature profile has the same FWHM but a peak of 310 °C. The head-disk clearance fh is set to 4 nm, so that the initial air bearing height ($h_{a,0}$) is 2.6 nm. We consider a disk speed U_d of 12.5 m/s (correspoding to disk rotational velocity of 5400 RPM and radial distance of 22.215 mm) and a simulation time t_f of 2 ns. The air bearing pressure at the NFT is set to 2.2 MPa. The peak disk/slider temperature, head-disk spacing and air bearing pressure data are approximately based on 15 mW TFC (Thermal Fly Height Control) Power and 2 mW NFT Power simulations using the CML HAMR code [73, 74]. We consider the same slider Air Bearing Surface (ABS) design for the HAMR air bearing simulations as [73, 74].

Figure 2.4 shows the time evolution of the lubricant profile on the disk and the slider in the cross-track and down-track directions. We see a central trough of depth 0.6 nm and side ridges of height 0.2 nm in the cross-track disk lubricant profile, similar to those seen in previous works [32]. The disk lubricant trough depth does not change much over time, however, the length of the depleted region continues to increase due to the disk motion in the down-track direction. As disk lubricant depletion increases with time, lubricant accumulation on the slider also grows. Starting with a uniform film of 0.2 nm on the slider, the simulation predicts a peak lubricant height of 0.83 nm at the end of 2 ns of illumination.

Figure 2.5 shows the partial pressure of the lubricant vapor in the air bearing in the cross-track direction. The lubricant vapor pressure is less than 0.1 MPa, while the air pressure at the NFT is 2.2 MPa, thereby justifying the dilute vapor assumption. At the NFT location (origin of co-ordinate system), the disk and slider lubricant thicknesses at the end of 2 ns are 0.59 nm and 0.83 nm respectively. The thin film equilibrium vapor pressure (Eq. (2.16)) at film thickness of 0.59 nm (h_d) and temperature of 500 °C (T_d) is 0.3 MPa and at 0.83 nm (h_s) and 310 °C (T_s) is 5 x 10^{-4} MPa. The partial pressure of the lubricant vapor phase at the origin (p_v) is 0.07 MPa. Thus, the large difference between the equilibrium vapor pressure of the disk lubricant and the head lubricant causes this relatively large mass flux from the disk to the head through the air bearing.

Figure 2.6 shows the dynamic air bearing height ($h_a = fh - h_d - h_s$) in the cross-track direction. At the origin (NFT location), the slider lubricant thickness reaches its peak value, however, the disk lubricant depletion is also maximized here. This causes a local maxima in the air bearing cross-track thickness profile. Two pairs of local minima are seen in the air bearing thickness profile. One pair of minima is seen at y = ± 11 nm, which corresponds to the ridges on the disk lubricant thickness profile. Another pair of minima are seen at y = ±

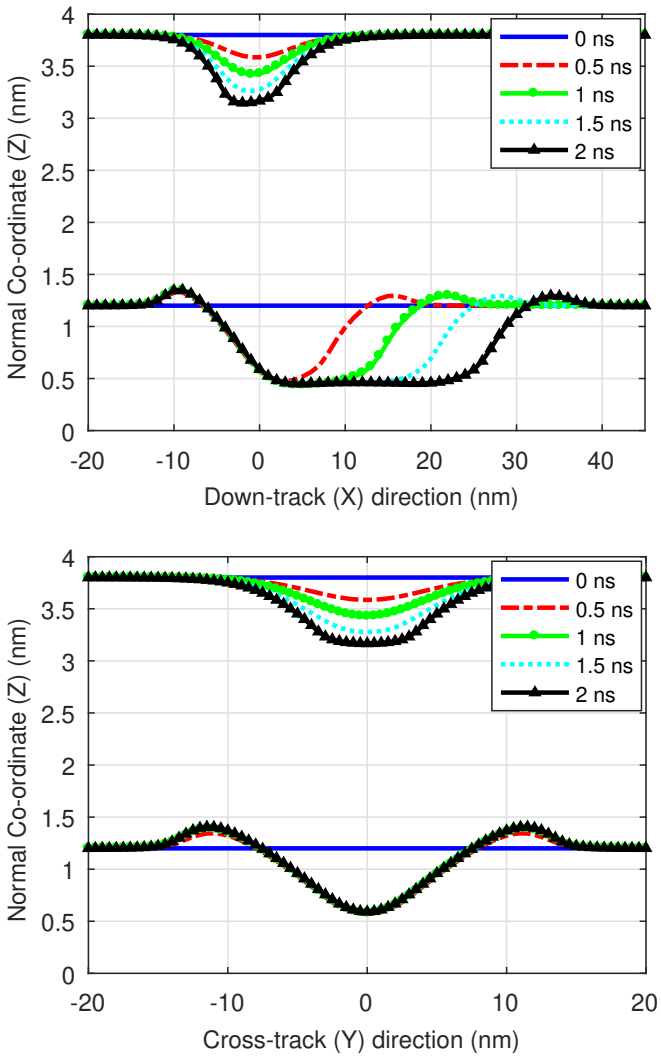

Figure 2.4: Cross-track and down-track Lubricant Profile on Disk and Slider at different times of laser illumination. $T_{max,d}$ = 500 °C, $T_{max,s}$ = 310 °C, U_d = 12.5 m/s, fh = 4 nm, FWHM = 20 nm. Origin ($X = 0$, $Y = 0$) is at NFT center.

3.5 nm. This location corresponds to the optimal point for the tradeoff between the rates of disk lubricant depletion and slider lubricant accumulation.

Effect of Disk Temperature

In this section, we investigate how the lubricant transfer process changes with maximum disk temperature, a consequence of varying the laser power, for fixed initial disk and slider

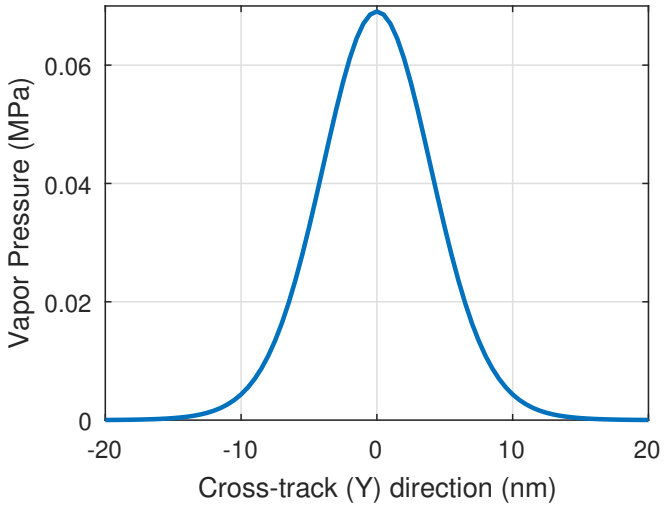

Figure 2.5: Cross-track profile of lubricant vapor phase partial pressure at the end of 2 ns of laser shine. $T_{max,d}$ = 500 °C, $T_{max,s}$ = 310 °C, U_d = 12.5 m/s, fh = 4 nm, FWHM = 20 nm. Origin ($X = 0$, $Y = 0$) is at NFT center.

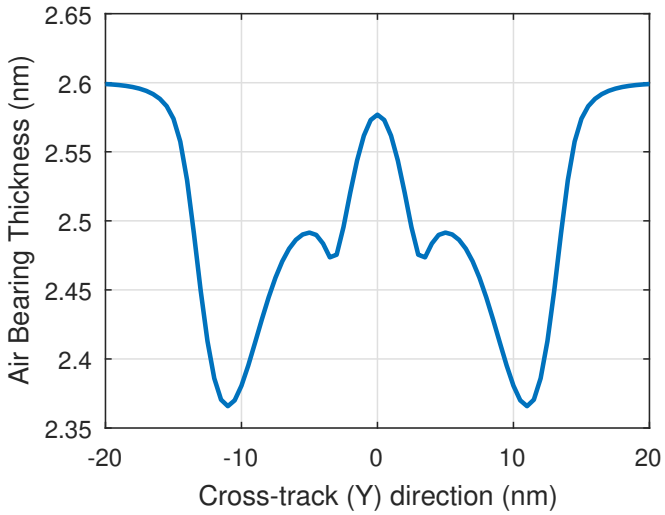

Figure 2.6: Cross-track profile of air bearing thickness at the end of 2 ns of laser shine. $T_{max,d}$ = 500 °C, $T_{max,s}$ = 310 °C, U_d = 12.5 m/s, fh = 4 nm, FWHM = 20 nm. Origin ($X = 0$, $Y = 0$) is at NFT center.

lubricant thicknesses of 1.2 nm and 0.2 nm respectively. We illuminate the lubricant with a 20 nm FWHM thermal spot scanning at a speed of 12.5 m/s for 2 ns. The maximum head temperature is kept constant at 310 °C and the maximum disk temperature is varied: 400 °C, 450 °C, 475 °C, 500 °C and 525 °C.

Figure 2.7 shows the cross-track and down-track profile of the disk and slider lubricant thicknesses for the different disk temperatures. The increase in maximum disk temperature

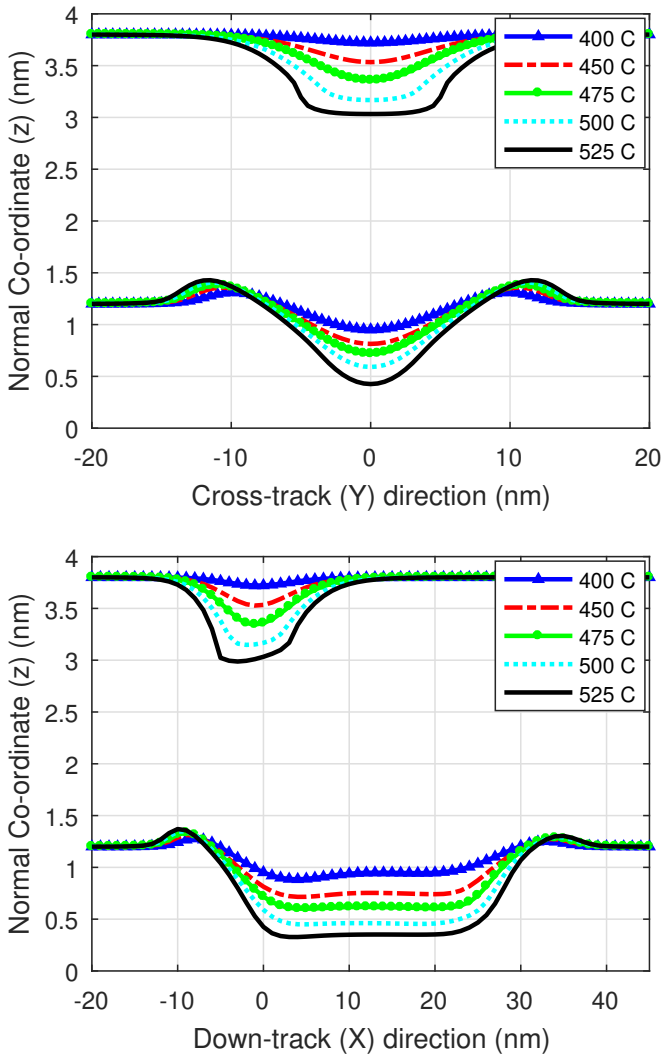

Figure 2.7: Cross-track and down-track lubricant profile on the disk and slider at different maximum disk temperatures. Dramatic increase in the slider's lubricant accumulation is predicted with increase in disk temperature. $T_{max,s} = 310$ °C, $U_d = 12.5$ m/s, fh = 4 nm, FWHM = 20 nm, $t_f = 2$ ns. Origin ($X = 0$, $Y = 0$) is at NFT center.

has two effects on the physics of disk lubricant deformation - the rate of evaporation increases and the thermocapillary shear stress becomes stronger (due to higher temperature gradient). At 400 °C, we see some small deformation in the disk lubricant profile, however, there is hardly any accumulation of lubricant on the slider. What little deformation is present at this temperature is due to thermocapillary shear stress. As shown in Figure 2.7, as the disk temperature is increased, the central trough (caused largely by evaporation) becomes wider as well as deeper. The height of the side ridges caused by thermocapillary shear stress also increases. The increased rate of evaporation from the disk causes the lubricant accumulation on the slider to rise.

Figure 2.10a plots the slider's lubricant accumulation ΔV_{slider} (defined as the difference between the initial and final volume of slider lubricant) as a function of maximum disk temperature. Not only does the lubricant accumulation increase with increase in disk temperature, but the slope of the accumulation versus disk temperature curve also increases at higher temperatures.

Effect of Slider Temperature

In this section, the maximum disk temperature is kept constant at 500 °C and the maximum slider temperature is varied: 200 °C, 250 °C, 310 °C, 350 °C and 400 °C. All other variables (initial lube thickness, disk speed, laser FWHM, simulation time, head-disk spacing, etc.) are kept the same as in the section on "Effect of Disk Temperature".

As shown in Figure 2.8, change in maximum slider temperature has a minor effect on the disk lubricant profile. As the slider's temperature increases, the amount of lubricant accumulation on the slider decreases, but the effect is relatively small. This is highlighted in Figures 2.10a and 2.10b which compare the effects of disk and slider temperatures on the lubricant transfer process. A variation in disk temperature from 400 °C to 525 °C causes the accumulation to increase from a meager 8 nm^3 to 118.8 nm^3. On the other hand, varying the slider's temperature from 200 °C to 400 °C causes only a small change in slider lubricant accumulation from 83.7 nm^3 to 77.9 nm^3.

Effect of Initial Lubricant Thickness

Here we study how the lubricant transfer process changes with initial disk lubricant thickness, for fixed disk and slider temperatures. Four cases of disk lubricant thickness: 0.6 nm, 0.8 nm, 1 nm and 1.2 nm are considered. Higher lubricant thicknesses are avoided so as to avoid the effect of dewetting and the influence of Laplace pressure. All other variables (initial slider lubricant thickness, disk speed, laser FWHM, simulation time, head-disk spacing, etc.) are kept the same as in the section on "Effect of Disk Temperature".

As shown in Figure 2.9, similar to the maximum disk temperature study, an increase in lubricant thickness causes the depth as well as width of the central trough on the disk to increase. For a disk temperature of 500 °C and slider temperature of 310 °C, thicker lubricant films of 1.2 nm and 1 nm have a peak accumulation thickness of 0.85 nm and

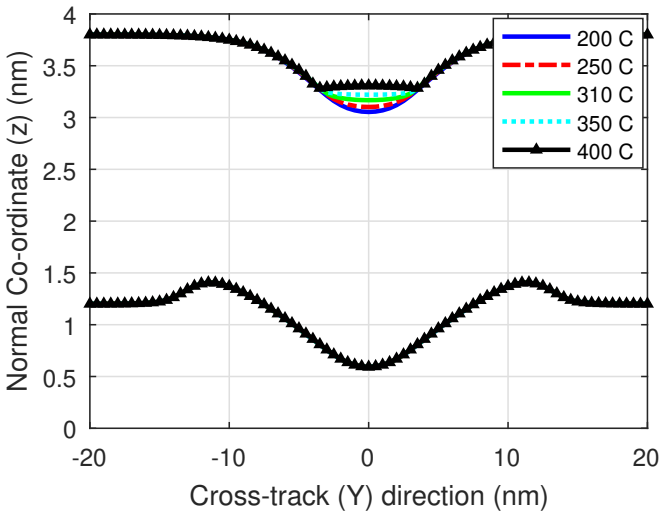

Figure 2.8: Cross-track lubricant profile on disk and slider at different maximum Slider Temperatures. $T_{max,d}$ = 500 °C, U_d = 12.5 m/s, fh = 4 nm, FWHM = 20 nm, t_f = 2 ns. Origin ($X = 0$, $Y = 0$) is at NFT center.

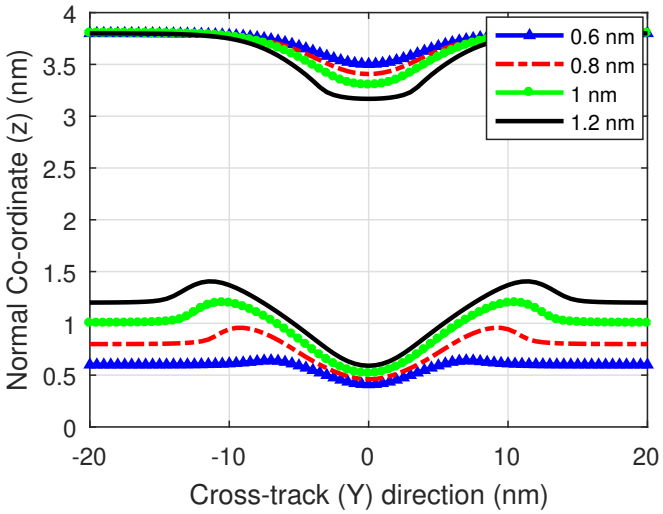

Figure 2.9: Cross-track lubricant profile on disk and slider at different initial lube thicknesses. $T_{max,d}$ = 500 °C, $T_{max,s}$ = 310 °C, U_d = 12.5 m/s, fh = 4 nm, FWHM = 20 nm, t_f = 2 ns. Origin ($X = 0$, $Y = 0$) is at NFT center.

0.71 nm, respectively, while the thinner lubricant films of 0.6 nm and 0.8 nm have a peak accumulation thickness of 0.6 nm and 0.5 nm, respectively. An increased amount and slope

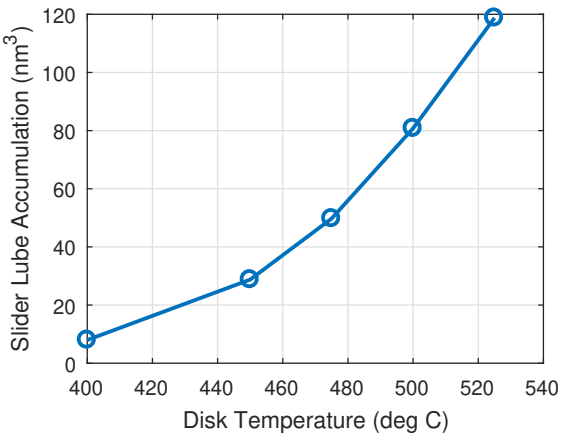

(a) Disk Temperature Study

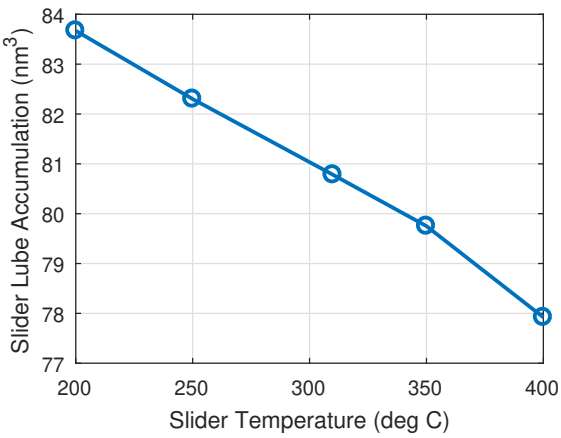

(b) Slider Temperature Study

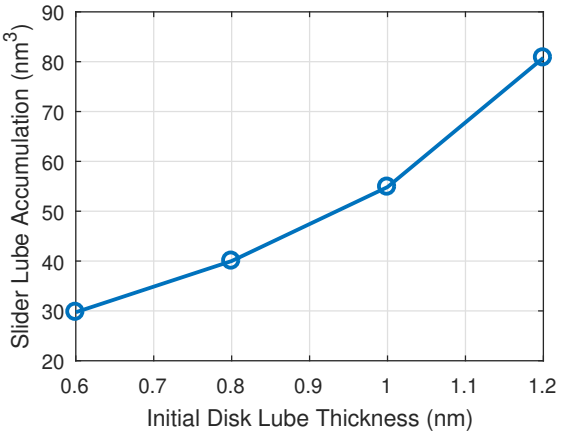

(c) Initial Lube Thickness Study

Figure 2.10: Lubricant Accumulation on the slider (nm^3) as a function of disk temperature, slider temperature and initial lube thickness. Increase in the disk temperature and initial lubricant thickness causes the slider lube accumulation to rise. Change in head temperature has a minimal effect on the accumulation.

(with respect to thickness) of lubricant accumulation on the slider is predicted, as highlighted in Figure 2.10c.

Effect of Air Bearing Convection and Diffusion

In this section, we investigate the effect of the air convection and diffusion model on the lubricant transfer process. We illuminate the disk lubricant with a 20 nm FWHM thermal spot scanning at a speed of 12.5 m/s for 1 ns. The maximum disk and slider temperatures

are kept constant at 500°C and 310°C respectively. We consider four cases - (a) without convection and diffusion (b) with convection, without diffusion, (c) without convection, with diffusion and (d) with convection and diffusion.

As shown the Figure 2.11, cases (a) and (b) (without diffusion, without/with convection) have similar solution profiles, as do cases (c) and (d) (with diffusion, without/with convection). Thus, the air convection model does not seem to have a significant effect on the lubricant transfer process. This can be justified by the following simple calculation. Kinetic energy of a vapor molecule is given by $\frac{1}{2}mv^2$, where $m = 2000 \times 1.66 \times 10^{-27}$ kg for Zdol 2000. The thermal energy of a vapor molecule can be estimated as $\frac{3}{2}kT$, where k is the Boltzmann constant. Equating these at a disk temperature of 773 K, we find that the speed of a vapor molecule ejected from the disk is of the order of 100 m/s [79]. This is almost 8 times the disk velocity. Thus the rate of ejection of lubricant molecules is much higher than the rate of convection, which explains why air convection has a negligible impact on the lubricant transfer process.

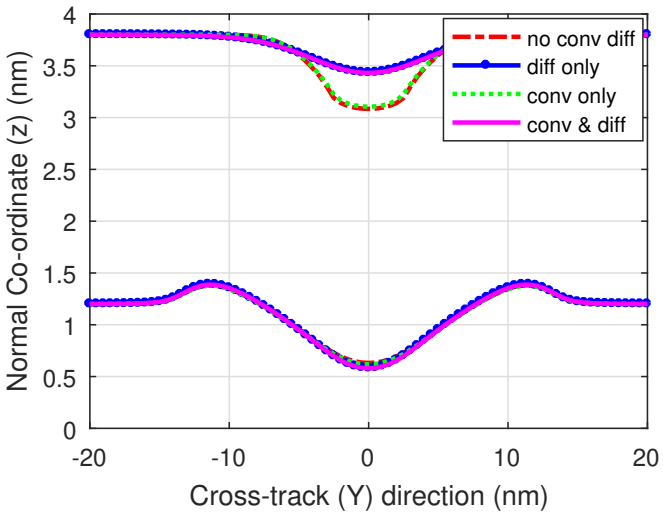

Figure 2.11: Effect of convection and diffusion on lubricant profile on the disk and slider. Convection has a small effect on the profile, diffusion causes the accumulation profile to spread-out. $T_{max,d} = 500$ °C, $T_{max,s} = 310$ °C, $U_d = 12.5$ m/s, fh = 4 nm, FWHM = 20 nm, $t_f = 1$ ns. Origin ($X = 0$, $Y = 0$) is at NFT center.

Diffusion, on the other hand, has a significant impact on the profile of the deposited slider lubricant film. For the cases where diffusion was ignored (a) and (b), the slider lubricant film has a much steeper slope and narrow width. Inclusion of the vapor diffusion effect causes the slider lubricant profile to spread out - the profile is wider but shorter in height, which is a direct consequence of the diffusion of the lubricant vapor pressure profile. However, the

volume of accumulation in all four cases was found to be almost unchanged (less than 6% change).

Laser Spot Size Study

Here we study the effect of the laser spot size on the lubricant transfer process. We consider four thermal spot sizes - 20 nm, 50 nm, 100 nm and 1 μm. To directly compare the amount of slider lubricant accumulation during the 2 ns of laser illumination, a normalized volume quantity needs to be determined. We follow the method used by Dahl and Bogy [32] and define "normalized slider lubricant accumulation" as:

$$\overline{\Delta V}_{slider} \equiv \frac{\Delta V_{slider}}{L^2}$$

where ΔV_{slider} is the slider's lubricant accumulation defined in the Section "Effect of Disk Temperature".

Figure 2.12 plots the normalized slider lubricant accumulation as a function of time for different spot sizes. For the shorter illumination time, $\overline{\Delta V}_{slider}$ for larger spot sizes is greater than that for smaller spot sizes. However, the trend reverses for larger simulation times. This implies that, on a relative scale, slider lubricant accumulation is more significant for larger spot sizes at small illumination times. However, for larger illumination times, slider lubricant accumulation is more significant for smaller spot sizes.

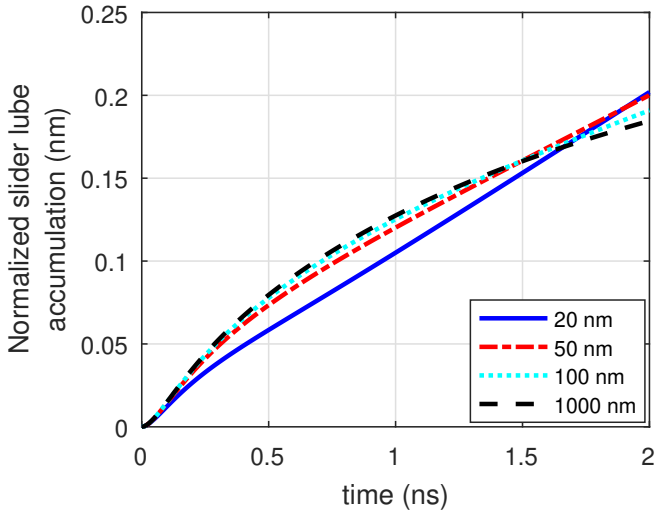

Figure 2.12: Normalized lubricant accumulation on slider (nm^3) versus time for different Laser Spot Sizes. On a relative scale, small laser spot sizes show larger accumulation for long simulation times. $T_{max,s}$ = 310 °C, U_d = 12.5 m/s, fh = 4 nm, FWHM = 20 nm.

Disjoining Pressure Study (Mechanical Transfer)

As described in Eq. (2.14), the disk lubricant disjoining pressure Π_d depends on the disk lubricant thickness h_d, slider lubricant thickness h_s and the head-disk spacing fh. Figure 2.13 plots the variation of disk lubricant disjoining pressure Π_d and its derivative $\frac{\partial \Pi_d}{\partial h_d}$ with h_s at $fh = 3$ nm and $h_d = 1.2$ nm. When only the disk-lubricant and/or slider-lubricant interactions are considered, the disk disjoining pressure is independent of h_s. However, when lubricant-lubricant interactions are considered, as h_s increases, both Π_d and $\frac{\partial \Pi_d}{\partial h_d}$ increase.

The increase in Π_d would result in the suppression of the evaporation rate from the disk according to Eqs. (2.16) and (2.17). Figure 2.13 shows that $\frac{\partial \Pi_d}{\partial h_d}$ becomes 0 at h_s of 0.77 nm and is positive for larger h_s. Hence, we expect that dewetting of the disk lubricant film would occur beyond this stage of lubricant accumulation on the slider. As the slider lubricant accumulation increases with time, the rate of evaporation decreases, while the dewetting instability of the disk lubricant film increases. This causes a change in the lubricant transfer mechanism from thermal (evaporation/condensation driven) to mechanical or molecular interactions driven (dewetting instability driven).

In order to demonstrate this phenomenon, we illuminate the disk lubricant with a 20 nm FWHM thermal spot scanning at a speed of 12.5 m/s at a head-disk spacing of 3 nm. The maximum disk and slider temperatures are kept constant at 500°C and 310°C, respectively. We consider two cases - (a) Effect of Slider and Slider Lubricant on Disk Disjoining Pressure are ignored, (b) Effect of Slider and Slider Lubricant on Disk Disjoining Pressure are considered. Figure 2.14 plots the cross-track and down-track lubricant profiles for the disk and slider after of 1.5 ns of illumination. Until this stage, the amount of lubricant transfer from the disk to the slider is higher for case (a) than case (b). When the influence of the slider and slider lubricant on the disjoining pressure are considered (Case (b)), the evaporation rate is lower due to higher disjoining pressure, leading to less transfer by the "thermally activated" mechanism. If the illumination of the disk is continued beyond 1.5 ns, the disjoining pressure and its derivative both continue to increase (in case (b)) due to the increase in the slider's lubricant height. Finally, at a simulation time of 1.9 ns, the disjoining pressure derivative becomes 0. The simulation becomes unstable beyond this stage due to dewetting. Any small perturbations in the system would continue to grow, causing the simulation to blow up. If the laser illumination is continued beyond 1.9 ns, we expect a significant pick-up of the disk lubricant caused by the temperature gradient on a dewetting lubricant film.

A similar effect is observed on decreasing the head-disk spacing. Figure 2.15 plots the variation of Π_d and $\frac{\partial \Pi_d}{\partial h_d}$ with fh at $h_s = 0.2$ nm and $h_d = 1.2$ nm. When only the disk-lubricant interactions are considered, Π_d is independent of fh. However, when the slider-lubricant and lubricant-lubricant interactions are considered, as fh decreases, both Π_d and $\frac{\partial \Pi_d}{\partial h_d}$ increase; $\frac{\partial \Pi_d}{\partial h_d}$ becomes 0 at fh of around 2.5 nm. At relatively higher head-disk spacing (~ 4 nm), the disk to slider lubricant transfer mechanism is largely thermally activated. On the other hand, for lower head-disk spacings (~ 2.5 nm), the transfer mechanism is largely driven by dewetting instability.

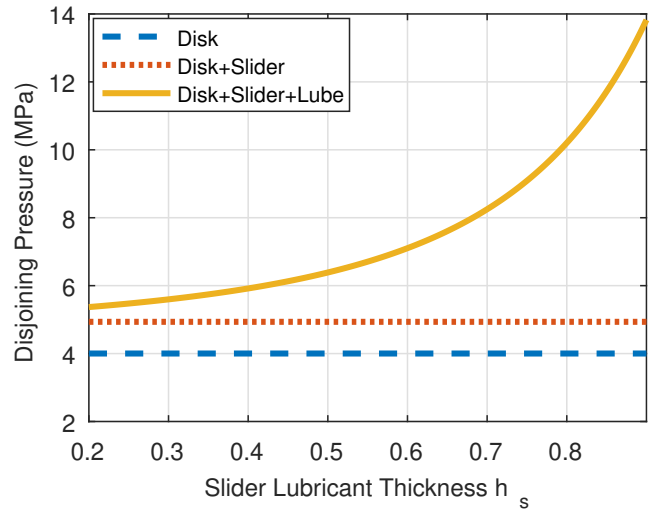

(a) Π_d

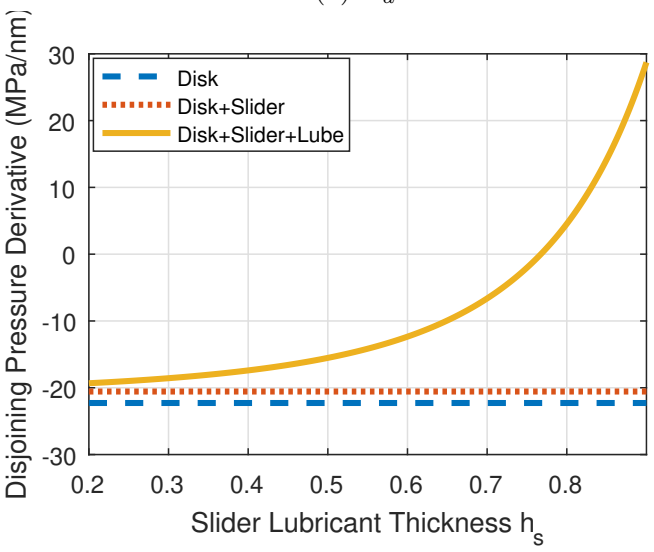

(b) $\frac{\partial \Pi_d}{\partial h_d}$

Figure 2.13: Effect of Slider Lubricant Thickness (h_s) on Disk Disjoining Pressure. When lubricant-lubricant interactions are considered, both Π_d and $\frac{\partial \Pi_d}{\partial h_d}$ increase rapidly with h_s.

2.5 Discussion

We have shown that several angstroms of lubricant accumulation on the slider is possible after 2 ns of disk lubricant illumination. At head-disk spacings of $\sim$ 3 - 4 nm, the head-disk lubricant transfer is initially largely caused by temperature difference driven evaporation/condensation. Lubricant accumulation grows much more with increase in temperature.

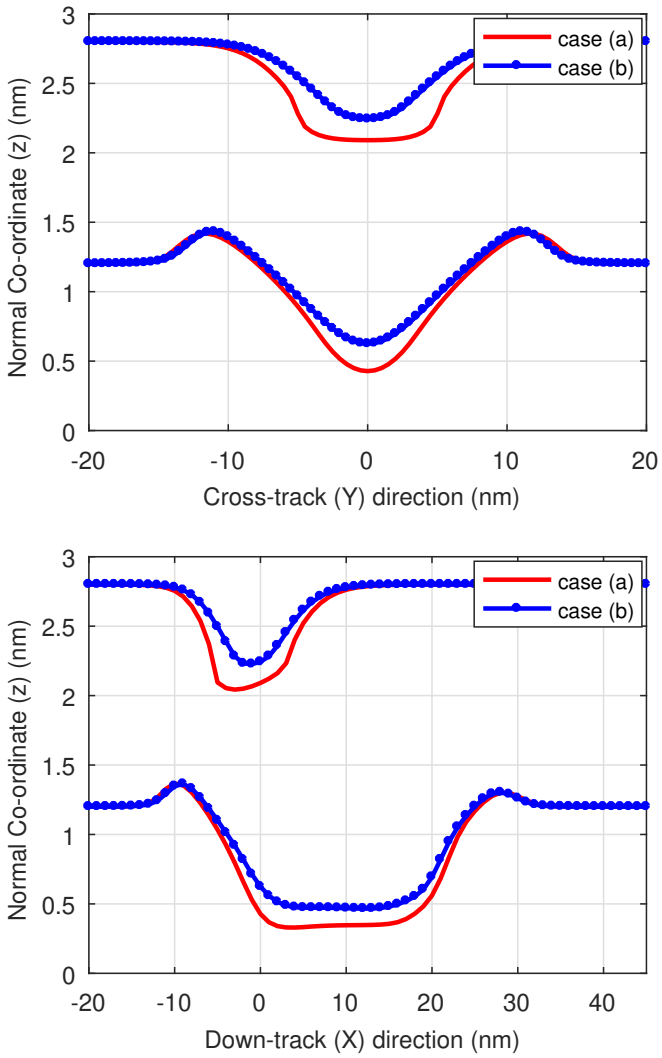

Figure 2.14: Disjoining Pressure Study: Case (a) Only disk-lubricant interactions are considered, Case (b) disk-lubricant, slider-lubricant and lubricant-lubricant interactions are considered. Increase in Π_d when all interactions are considered causes the amount of lube transfer due to evaporation to decrease. $T_{max,d} = 500$ °C, $T_{max,s} = 310$ °C, $U_d = 12.5$ m/s, fh = 4 nm, FWHM = 20 nm, $t_f = 1.5$ ns. Origin ($X = 0$, $Y = 0$) is at NFT center.

When an initial disk lubricant film of 1.2 nm is subjected to a maximum disk temperature of 400°C, the slider lubricant accumulation is merely 8 nm^3, whereas at a peak temperature of 525°C, the accumulated volume is 118.8 nm^3. Moreover, close to the HAMR target temperature, even small changes in the maximum disk temperature can help in reducing the lubricant transfer to the head. For example, reducing the peak temperature from 525°C to

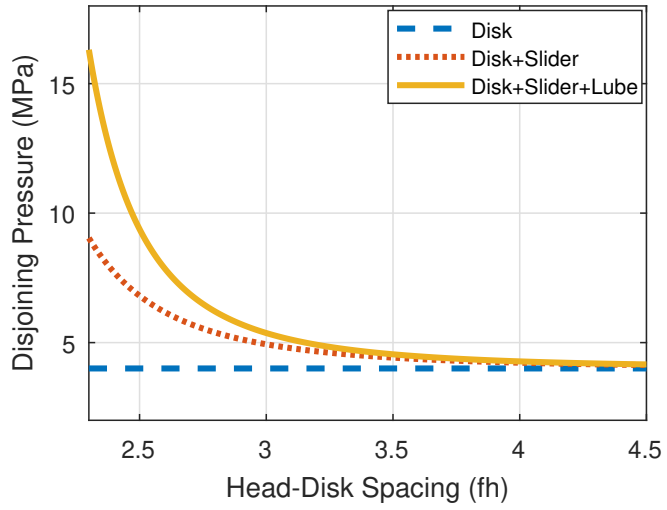

(a) Π_d

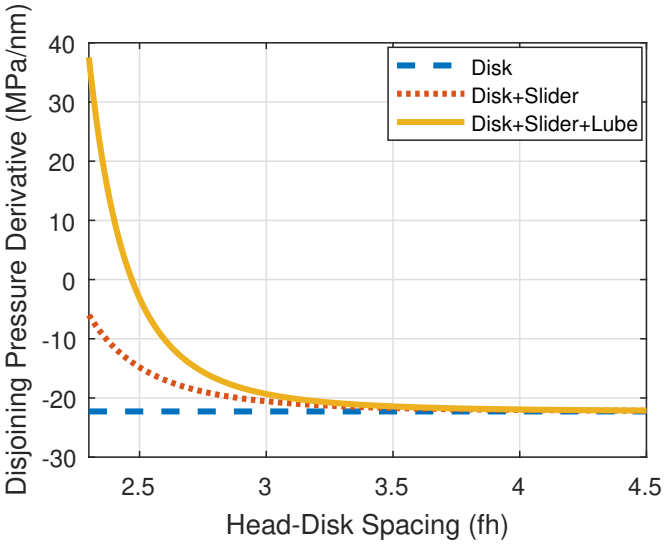

(b) $\frac{\partial \Pi_d}{\partial h_d}$

Figure 2.15: Effect of Head-Disk Spacing (fh) on Disk Disjoining Pressure. When the slider-lubricant and lubricant-lubricant interactions are considered, both Π_d and $\frac{\partial \Pi_d}{\partial h_d}$ increase rapidly as h_s decreases.

500°C and further to 475 °C reduces the accumulated volume on the slider from 118.8 nm^3 to 80.8 nm^3 and further to 49.8 nm^3. The corresponding drop in the peak slider lubricant height is 1 nm to 0.85 nm and further to 0.65 nm for 525°C, 500°C and 475°C, respectively. While it was expected that a drop in media temperature would result in a lower transfer,

the high sensitivity of the slope of the lubricant accumulation curve (Figure 2.10a) near the HAMR target temperature of 500 °C is a crucial insight towards managing lubricant and material transfer during HAMR writing.

Comparatively, the head temperature has a small impact on the amount of lubricant transfer. Variation in the maximum head temperature from a high of 400°C to a low of 200°C (with the disk being maintained at a peak temperature of 500°C) resulted in a rise in the slider lubricant accumulation from 77.9 nm^3 to only 83.7 nm^3. The corresponding variation in peak slider lubricant height is 0.77 nm to 0.97 nm. Thinner lubricant films have larger disjoining pressures and effective viscosities and are much more resistive to deformation and evaporation. Reducing the thickness of the initial lubricant film coated on the disk can also help in reducing the amount of lubricant pick-up.

While the lubricant transfer is initially dominated by evaporation/condensation, as the amount of lubricant accumulation on the slider increases, the influence of the slider-lubricant and lubricant-lubricant molecular interactions becomes increasingly important. There exists a critical value of accumulated slider lubricant thickness at which the disjoining pressure derivative becomes zero and significant lubricant transfer is expected originating from dewetting instability. Figure 2.16a plots this critical slider lubricant thickness as a function of disk lubricant thickness at different head-disk spacings. We see that for higher disk lubricant thickness, the critical slider lubricant thickness for the onset of dewetting is lower. The critical slider lubricant thickness also decreases as the head-disk spacing is reduced. In fact, at very low head-disk spacings ($\sim$ 2.5 nm), lubricant dewetting occurs at almost no slider lubricant accumulation. This is highlighted in Figure 2.16b, which plots the critical head-disk spacing at which the dewetting of disk lubricant occurs without any accumulation of slider lubricant (h_s was set equal to 0.2 nm) as a function of disk lubricant thickness. At such low spacings, we expect to see lubricant pick-up even before the initiation of laser heating. This phenomenon was demonstrated experimentally by Ambekar et. al [45].

Few numerical studies have been presented in the literature on lubricant transfer in HAMR, however, those models may not be sufficiently accurate due to some unrealistic assumptions, such as a uniform disk lubricant film and uniform temperature distribution. Ma and Liu [42] studied lubricant transfer in HAMR without considering the effect of spatial temperature gradient on lube evolution. While their model qualitatively predicted that lube thinning rate increases dramatically with rise in temperature, they predicted significantly lower lube thinning rates - time for 1 nm disk lube in the area from 20 to 40 mm radius to uniformly thin 1Å was on the order of seconds for Zdol 2000 under a 100 nm laser spot at 450°C. Our model and previous works [32] predict several angstroms of local lube deformation and transfer in a time scale of nanoseconds due to spatial temperature variation at similar peak media temperatures and laser spot sizes.

In this study, we have not considered the effects of thermal decomposition or lubricant polydisperity. Experiments suggest that the thermal decomposition of Zdol occurs at temperatures above 600 K [80]. Hence, in addition to evaporation, thermal decomposition could be another potential mechanism contributing towards desorption of lubricant molecules from the disk at high temperatures. PFPE lubricants are not chemically pure materials, but

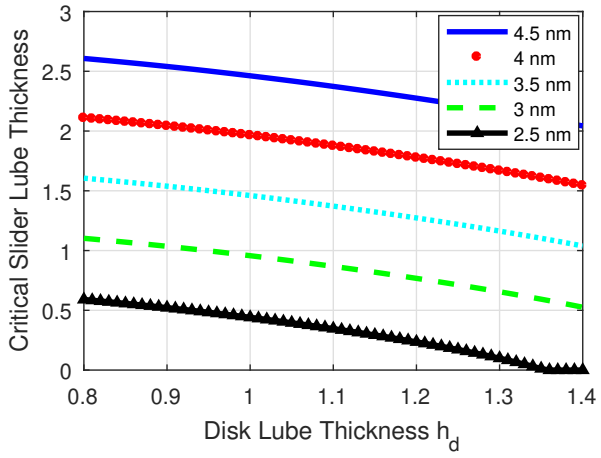

(a) Critical accumulated head lubricant thickness for the onset of dewetting versus disk lubricant thickness at different head-disk spacings. Critical head lube thickness decreases with an increase in the disk lube thickness and decrease in head-disk spacing.

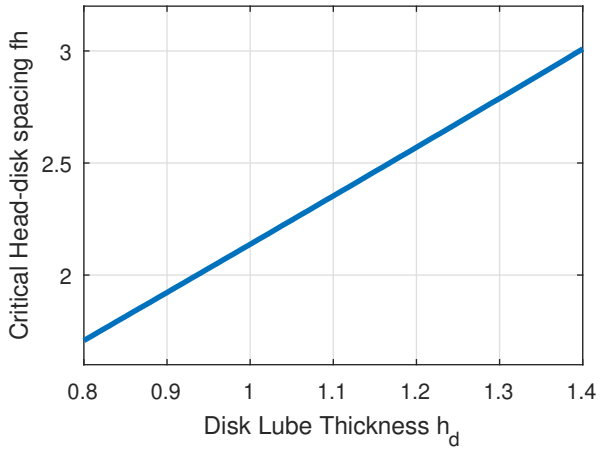

(b) Critical Head-disk spacing for the onset of dewetting instability as a function of disk lubricant thickness. At head-disk spacings below the critical value, lubricant pick-up is expected to occur even before the laser is turned on.

Figure 2.16: Critical h_s and fh for onset of Dewetting Instability

rather are a mixture of different molecular weight components. Since the rate of evaporation is a strong function of molecular weight, the degree of polydisperity will determine how the evaporation rate varies as lighter molecules will evaporate first [81].

The same physics of molecular interactions and their changes with temperature applies to surface tension and interfacial energetics. Marchon and Saito [33] considered the effect of a temperature dependent Hamaker constant on lubricant thermo-diffusion under laser heating. The model developed here can be improved by considering the effect of temperature on the Hamaker constants A_{VLS}, A_{LVL} and A_{SVL}.

The lubricant is assumed to be a viscous, Newtonian fluid in this study. In reality, PFPE lubricants exhibit viscoelastic behavior [6]. We present an improved version of this model which considers the effect of viscoelasticity on lubricant deformation and disk-to-head transfer in subsequent chapters 3 and 4 of this thesis.

The governing equation for the disk/slider lubricant film used in this study assumes a quasi-parallel film. Though the results presented are only for 2 ns of laser illumination, we performed simulations with this model for longer laser shine times ($\sim$ 10 ns). We found that as the amount of slider accumulation increases with time, the slope of the slider lubricant profile becomes very high, violating the quasi-parallel film assumption. In order to predict the lubricant transfer process for high volumes of accumulation, the governing equations need to be modified to allow high slopes. The expression for disjoining pressure also needs to be updated to consider the impact of film curvature [82].

2.6 Conclusion

We have developed a continuum mechanics based viscous model that predicts the lubricant transfer from the disk to the slider during HAMR writing. The model simultaneously determines the deformation and evaporation of the lubricant film on the disk, the convection and diffusion of the vapor phase lubricant in the air bearing and the evolution of the condensed lubricant film on the slider. The model also accounts for molecular interactions between the disk-lubricant, slider-lubricant and lubricant-lubricant in terms of disjoining pressure.

We found that at head-disk spacings of $\sim$ 3 - 4 nm, the disk-to-head transfer mechanism is initially largely thermally driven. Hence, the amount of lubricant accumulation on the slider can be significantly reduced by decreasing the media temperature. However, as lubricant accumulation increases with time, we see a change in the transfer mechanism from thermally driven to molecular interactions driven (dewetting instability). A similar change in transfer mechanism from thermal to mechanical is predicted as we reduce the head-disk spacing. There exists a critical value of head-disk spacing and a critical value of head lubricant height at which dewetting of the disk lubricant begins, leading to enhanced lubricant pick-up.

This chapter presents work published in Tribology Letters (reprinted by permission from Springer Nature (Tribology Letters) [83], Copyright (2017))

Chapter 3

Viscoelastic Model for Disk Lubricant Deformation During HAMR

3.1 Introduction

During HAMR, a complex laser delivery system exposes the magnetic media to a high temperature in order to reduce its coercivity during writing. The high temperature gradient on the media causes the lubricant to deform and deplete under the influence of driving forces such as thermo-capillary stress and evaporation. It is imperative for the lubricant to withstand this writing process and sufficiently recover post-writing to ensure that the disk remains well-protected and the head flies stably.

In Chapter 2, we studied the behavior of the lubricant film on the disk and its transfer to the head during HAMR writing using a continuum model, while assuming the lubricant to be a purely viscous material. Numerous other works in the literature have also investigated lubricant behavior during HAMR using viscous continuum models [31–34]. However, experiments show that perfluoropolyether (PFPE) lubricants are viscoelastic fluids [6, 84, 85] and can behave like viscous fluids or elastic solids or a combination of both depending on the flow timescale [36]. Sarabi & Bogy studied the effect of viscoelasticity on lubricant behavior during HAMR using a Finite Element implementation of the Linear Maxwell model in ANSYS [37]. They found that the lubricant exhibits elastic behavior with instantaneous deformations. However, this model solves the complete 3D equations of motion, failing to take advantage of the lubrication approximation. Moreover, disjoining pressure was linearized to ease computation speed and the effect of evaporation was not included.

In this chapter, we introduce a modified Reynolds lubrication equation (2D) for the viscoelastic fluid using the Linear Maxwell model and demonstrate similar results to the 3D ANSYS model developed by Sarabi & Bogy [37]. Our model uses non-linear disjoining pressure and includes evaporation. Experiments by Mate et al. on lubricant migration on the slider suggest that slippage might be a dominant mechanism when the lubricant is subjected to high shear stresses [86]. Accordingly, we also investigate the effect of inclusion of a slip

boundary condition on lubricant behavior under high thermo-capillary stress during HAMR.

3.2 Lubricant Rheology

Linear Viscoelasticity and Deborah Number

Under small deformation gradients, viscoelastic fluids exhibit linear behavior. The most basic model for a linear viscoelastic fluid is the Linear Maxwell model (single stage), which is described by the following equation:

$$\begin{aligned} \boldsymbol{\sigma} &= -p\boldsymbol{I} + \boldsymbol{\tau} \\ \frac{\boldsymbol{\tau}}{\eta} + \frac{1}{G}\frac{\partial \boldsymbol{\tau}}{\partial t} &= \nabla \boldsymbol{v} + (\nabla \boldsymbol{v})^T \end{aligned} \tag{3.1}$$

Here $\boldsymbol{\sigma}$ is the Cauchy stress, p is the pressure of the incompressible fluid, $\boldsymbol{\tau}$ is the extra stress and $\boldsymbol{v}$ is the velocity. Viscosity η and shear modulus G are related to Maxwell relaxation time λ by $\eta = G\lambda$.

A viscoelastic fluid can exhibit viscous or elastic behavior depending on the flow timescale. In order to characterize this behavior, the non-dimensional parameter "Deborah number" is introduced by normalizing the maxwell relaxation time by the flow timescale: $De = \frac{\lambda}{t_s}$. When $De \ll 1$, the material behaves like a viscous fluid, when $De \gg 1$ it behaves like an elastic solid and for $De \sim 1$ the material has both viscous and elastic characteristics. For the lubricant under HAMR, the flow time scale may be defined as $t_s = \frac{L}{U}$, where L is the laser FWHM (set as 20 nm in this study) and U is the disk velocity ($\sim$ 10 m/s), thus $De = \frac{\lambda U}{L}$ [37].

Bulk Lubricant Rheology

Bulk rheological properties of PFPE lubricants have been studied by measuring their viscosity (η), storage modulus ($G^{'}$), loss modulus ($G^{"}$) via steady-shear and dynamic oscillation measurements using rotational rheometers [6, 84, 85]. Kono et al. investigated the rheological properties of PFPEs with different molecular weights and end-groups [84]. Karis measured the dynamic moduli of several PFPEs including Zdol 2500 and Ztetraol 2000 between 1 and 100 rad/s at temperatures from -20 to 100 °C [6]. The PFPEs were found to be linear viscoelastic at these conditions (dynamic strain amplitude of 5%). The data measured at low temperatures was transformed to high frequency through time-temperature superposition with Williams Landel Ferry (WLF) Coefficients:

$$log(a_{T_0}) = \frac{-C_1(T - T_0)}{C_2 + (T - T_0)} \tag{3.2}$$

Here reference temperature T_0 is the glass transition temperature of the PFPE and C_1 and C_2 are WLF coefficients with respect to T_0. Upto 3 linear Maxwell elements (i.e. 3 sets

of shear moduli G_i and Maxwell relaxation times τ_i) were derived for each PFPE from the data for $G^{'}$, $G^{"}$ versus ωa_{T_0}. The measurements for τ_i and G_i show that for these multistage models, one of the stages is dominant ($\tau_1 \gg \tau_2, \tau_3$). To simplify calculations, we consider only the dominant stage and reduce Karis' model to a single-stage one (i.e. Linear Maxwell model - Eq. (3.1)) with shear modulus G_{bulk} ($= G_1$) and viscosity η_{bulk}. Accordingly the viscosity as a function of temperature is given by:

$$\eta_{bulk}(T) = \eta_{bulk}(T_0) a_{T_0}(T) \tag{3.3}$$

where $\eta_{bulk}(T_0)$ is the viscosity at the reference temperature T_0 and $a_{T_0}(T)$ is given by Eq. (3.2). The Maxwell relaxation time can be obtained as: $\lambda_{bulk} = \frac{\eta_{bulk}}{G_{bulk}}$. The Maxwell relaxation time and viscosity have the same temperature shift function and thus the shear modulus is independent of temperature. T_0, C_1, C_2, $\eta_{bulk}(T_0)$, G_{bulk} for Zdol 2500 and Ztetraol 2000 are tabulated in Table 6.1. Viscosity of Ztetraol as a function of temperature using Eqs. (3.2), (3.3) is plotted in Figure 3.1.

Lubricant	Zdol 2500	Ztetraol 2000
T_0	-113.6 °C	-112.2 °C
C_1	13.62	23.22
C_2	59.72	45.81
$\eta_{bulk}(T_0)$	4.16e+8 Pa-s	2.34e+17 Pa-s
G_{bulk}	51.9 kPa	36.6 kPa

Table 3.1: Glass transition temperature T_0, WLF coefficients C_1, C_2, viscosity η_{bulk} at T_0 and shear modulus G_{bulk} for Zdol 2500 and Ztetraol 2000 [6]

Thin Film Lubricant Rheology

Ruths & Granick measured the dynamic moduli $G^{'}$, $G^{"}$ of thin unfunctionalized and functionalized PFPE films (2.8 nm Z03, 3.3 nm Zdol 2100, 6.6 nm Zdol 4000) at normal pressures of 1 and 3 MPa and shear rates of 10^{-2} to 10^{5} s^{-1} [87]. The properties were measured by shearing the films between two mica surfaces using a surface force apparatus (SFA). They found that the unfunctionalized Z03 displayed elastic behavior in the entire frequency range of 1.3-130 Hz with large, frequency independent moduli (in the regime of linear response i.e. small-amplitude oscillatory shear). Zdol 2100 also exhibited elastic behavior with frequency independent moduli ($G^{'} \sim 1$ MPa, $G^{"}$ was one order of magnitude smaller) at higher normal pressure of 3 MPa. Under large deformations, the moduli dropped significantly due to shear thinning/slip. These results suggest that the Maxwell relaxation time and zero-shear viscosity of nano-scale films are several orders of magnitude higher than the bulk values. More recently Itoh et al. measured the dynamic moduli of Z03 and Zdol at higher frequencies

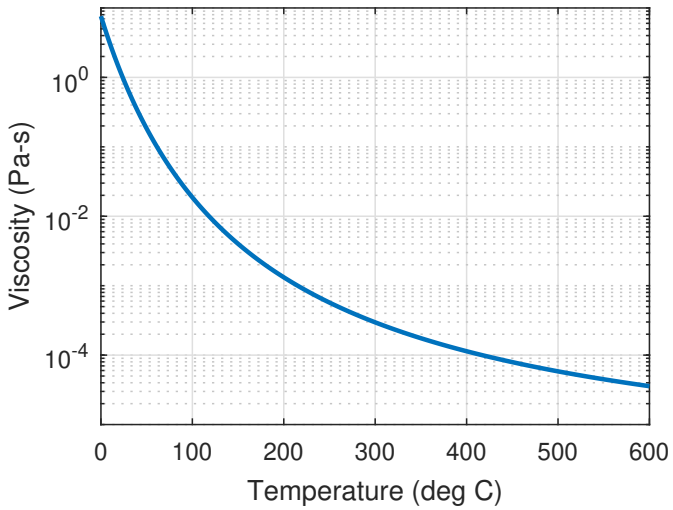

Figure 3.1: Bulk Ztetraol viscosity (Pa-s) versus temperature (°C) using oscillatory measurements and time-temperature superposition (Eqs. (3.2), (3.3)) [6]

using a Fiber Wobbling Method (FWM) [88, 89]. They found that as the film thickness decreases, both the viscosity and elasticity of the lubricant increase.

Mate & Marchon studied the shear response of similar unfunctionalized PFPE films when subjected to air shear stress of 20 - 200 Pa (comparable shear rates to SFA) using a blow-off technique [52]. They found that molecularly thin films partially confined by a single solid surface do not solidify (unlike SFA results) and display viscous behavior. They attributed the "solid like behavior" in the SFA experiment to confinement of molecules between two solid surfaces with applied pressure. Scarpulla et al. [54] studied the shear properties of molecularly thin films of the functionalized lubricant Zdol using blow-off and found that its flow can be described by an enhanced effective viscosity (larger than the bulk viscosity for functionalized lubricants). Karis et al. studied lubricant spin-off from magnetic disks and reported that the effective viscosity of Zdol increases exponentially with decrease in thickness [53].

More recently Marchon et al. [90] and Mate et al. [86] studied the migration of the functionalized lubricant Ztetraol on the head under higher air shear stresses ($\sim$ 500 kPa in [90], $\sim$ 10 kPa in [86]). They found that the effective thin-film viscosity is either similar to or smaller than the bulk viscosity (in contrast with previous studies [53, 54] where the effective viscosity was larger than the bulk viscosity). Moreover, the effective viscosity was found to decrease with decreasing lubricant thickness. This apparent discrepancy was attributed to slip caused by high shear stresses. As the film thickness is reduced, slip becomes a more dominant migration mechanism, which would manifest itself within the viscous flow simulation as a lower viscosity.

Experiments on lubricant films on a solid substrate under air shear demonstrate that the behavior of thin films confined by a single solid and confined between two solids are significantly different. Dynamic properties from SFA/FWM experiments cannot be directly used to study the behavior of lubricant under HAMR laser heating (confined by a single solid - the disk). Hence we use the bulk rheological properties from Table 6.1 with appropriate thin-film enhancement factors. Karis et al. [53] found a viscosity enhancement factor of ∼13 for 1 nm thick Zdol 4000. Accordingly, we assume that the effective viscosity for both Zdol and Ztetraol is 13 times the bulk viscosity determined using Eq. (3.3) (i.e. $\eta_{eff} = 13 \times \eta_{bulk}$). To account for slippage caused by high shear stresses, we apply the Navier slip boundary condition, which assumes that the slip velocity $\boldsymbol{v_{slip}}$ is directly proportional to the wall shear stress $\boldsymbol{\tau_{wall}}$:

$$\boldsymbol{v_{slip}} = \frac{b}{\eta}\boldsymbol{\tau_{wall}} \tag{3.4}$$

Here b is the slip length. Other non-linear slip boundary conditions are also available such as power-law dependence on wall shear stress or a threshold-type slip [91]. However, the Navier slip boundary condition is the simplest one and is commonly used to study the combined effect of slip and viscoelasticity on thin polymer film evolution [92, 93]. Since no quantitative data is available in literature about the effect of confinement (by a single solid) on the Maxwell relaxation time, we assume that $G_{eff} = 13 \times G_{bulk}$ and $\lambda_{eff} = \lambda_{bulk}$ in the baseline simulation (so that $\eta_{eff} = G_{eff}\lambda_{eff}$). We also perform a sensitivity analysis to see how the lubricant behavior changes if the enhancement factor of 13 is partially absorbed by λ_{eff} and G_{eff} (Refer Section 3.5: "Effect of Shear Modulus").

3.3 Lubrication Theory based on Linear Maxwell Model

Lubrication Equation Derivation

We consider the generic problem of a thin lubricant film of thickness $h(x, y, t)$ on a flat substrate, moving at a constant linear speed U. The frame of reference is moving along with the substrate (so that the substrate appears to be rest). The co-ordinate system is defined such that the z axis is along the lubricant thickness and the x axis is along the direction of the substrate velocity. The top surface of the lubricant ($z = h$) is free to evolve under the influence of external shear stress $\boldsymbol{\tau_b}(x, y, t) = \tau_{b,x}\boldsymbol{e_x} + \tau_{b,y}\boldsymbol{e_y}$ and external pressure $p_b(x, y, t)$.

We assume that the characteristic dimension in the z direction, h_0 is much smaller than the characteristic dimension in the x and y directions, L. The inertial terms in the equation of motion are assumed to be small compared to the extra stress terms. We also assume that the stresses τ_{xx}, τ_{xy}, τ_{yy}, τ_{zz} are smaller than or comparable to τ_{xz}, τ_{yz}. With these assumptions, the Cauchy equation of motion, the constitutive law (Eq. (3.1)) and the continuity equation

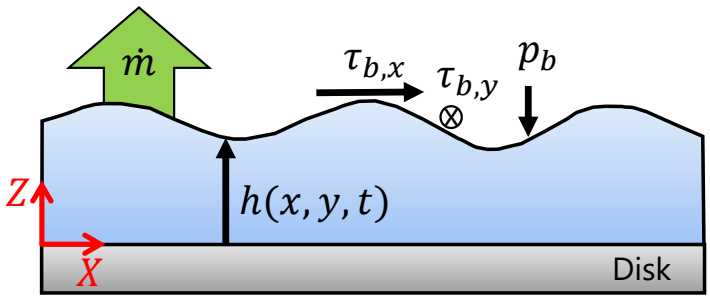

Figure 3.2: Lubricant film of thickness $h(x, y, t)$ evolves under the influence of external shear stress $\boldsymbol{\tau_b} = \tau_{b,x}\boldsymbol{e_x} + \tau_{b,y}\boldsymbol{e_y}$ and external pressure p_b acting on its top surface. Some lubricant is removed from the film via evaporation ($\dot{m}$).

simplify to [36]:

$$\begin{aligned} -\frac{\partial p}{\partial x} + \frac{\partial \tau_{xz}}{\partial z} &= 0 \\ -\frac{\partial p}{\partial y} + \frac{\partial \tau_{yz}}{\partial z} &= 0 \\ \frac{\partial p}{\partial z} &= 0 \end{aligned} \tag{3.5}$$

$$\begin{aligned} \frac{\tau_{xz}}{\eta} + \frac{1}{G}\frac{\partial \tau_{xz}}{\partial t} &= \frac{\partial v_x}{\partial z} \\ \frac{\tau_{yz}}{\eta} + \frac{1}{G}\frac{\partial \tau_{yz}}{\partial t} &= \frac{\partial v_y}{\partial z} \end{aligned} \tag{3.6}$$

$$\frac{\partial h}{\partial t} + \frac{\partial}{\partial x}\left(\int_0^h v_x dz\right) + \frac{\partial}{\partial y}\left(\int_0^h v_y dz\right) + \frac{\dot{m}}{\rho} = 0 \tag{3.7}$$

Eq. (3.7) is obtained by integrating the continuity equation across the film thickness (a derivation can be found in Ref. [59]). Here ρ is the lubricant density and $\dot{m}$ is the evaporation mass flux per unit time. v_x, v_y are the lubricant velocity components along x and y respectively and p is the lubricant pressure. Integrating Eq. (3.5) subject to boundary condition at $z = h$ ($\tau_{xz}|_{z=h} = \tau_{b,x}$, $\tau_{yz}|_{z=h} = \tau_{b,y}$, $p|_{z=h} = p(x, y, t) = p_b$), we obtain these shear stress profiles:

$$\begin{aligned} \tau_{xz} &= \frac{\partial p}{\partial x}(z - h) + \tau_{b,x} \\ \tau_{yz} &= \frac{\partial p}{\partial y}(z - h) + \tau_{b,y} \end{aligned} \tag{3.8}$$

We consider the linear Navier slip boundary condition (Eq. (3.4)) at $z = 0$ (with constant slip length b)

$$\begin{aligned} v_x|_{z=0} &= \frac{b}{\eta}\tau_{xz}|_{z=0} = \frac{b}{\eta}\left(-\frac{\partial p}{\partial x}h + \tau_{b,x}\right) \\ v_y|_{z=0} &= \frac{b}{\eta}\tau_{yz}|_{z=0} = \frac{b}{\eta}\left(-\frac{\partial p}{\partial y}h + \tau_{b,y}\right) \end{aligned} \tag{3.9}$$

Inserting the shear stress profiles from Eq. (3.8) into Eq. (3.6) and integrating using the boundary condition at $z = 0$, we obtain the following velocity profiles:

$$\begin{aligned} v_x &= \frac{1}{\eta}\left[\frac{\partial p}{\partial x}\left(\frac{z^2}{2} - hz - bh\right) + \tau_{b,x}\left(z + b\right)\right] + \frac{1}{G}\left[\frac{\partial^2 p}{\partial t \partial x}\left(\frac{z^2}{2} - hz\right) - \frac{\partial p}{\partial x}\frac{\partial h}{\partial t}z + \frac{\partial \tau_{b,x}}{\partial t}z\right] \\ v_y &= \frac{1}{\eta}\left[\frac{\partial p}{\partial y}\left(\frac{z^2}{2} - hz - bh\right) + \tau_{b,y}\left(z + b\right)\right] + \frac{1}{G}\left[\frac{\partial^2 p}{\partial t \partial y}\left(\frac{z^2}{2} - hz\right) - \frac{\partial p}{\partial y}\frac{\partial h}{\partial t}z + \frac{\partial \tau_{b,y}}{\partial t}z\right] \end{aligned} \tag{3.10}$$

Inserting the velocity profiles from Eq. (3.10) into the integrated continuity Eq. (3.7), we arrive at the governing equation for the viscoelastic lubricant:

$$\begin{aligned} &\frac{\partial h}{\partial t} + \frac{\partial}{\partial x}\left(-\frac{h^3}{3\eta}\frac{\partial p}{\partial x} + \frac{h^2}{2\eta}\tau_{b,x} - \frac{h^2 b}{\eta}\frac{\partial p}{\partial x} + \frac{hb}{\eta}\tau_{b,x}\right) + \frac{\partial}{\partial x}\left(-\frac{h^3}{3G}\frac{\partial^2 p}{\partial t \partial x} - \frac{h^2}{2G}\frac{\partial p}{\partial x}\frac{\partial h}{\partial t} + \frac{h^2}{2G}\frac{\partial \tau_{b,x}}{\partial t}\right) \\ &\quad + \frac{\partial}{\partial y}\left(-\frac{h^3}{3\eta}\frac{\partial p}{\partial y} + \frac{h^2}{2\eta}\tau_{b,y} - \frac{h^2 b}{\eta}\frac{\partial p}{\partial y} + \frac{hb}{\eta}\tau_{b,y}\right) + \frac{\partial}{\partial y}\left(-\frac{h^3}{3G}\frac{\partial^2 p}{\partial t \partial y} - \frac{h^2}{2G}\frac{\partial p}{\partial y}\frac{\partial h}{\partial t} + \frac{h^2}{2G}\frac{\partial \tau_{b,y}}{\partial t}\right) \\ &\quad + \frac{\dot{m}}{\rho} = 0 \end{aligned} \tag{3.11}$$

In this equation, $q_{viscous,x} = \left(-\frac{h^3}{3\eta}\frac{\partial p}{\partial x} + \frac{h^2}{2\eta}\tau_{b,x}\right)$ is the viscous volumetric flow rate per unit width (originating from the viscous part of the constitutive Eq. (3.6)), $q_{slip,x} = \left(-\frac{h^2 b}{\eta}\frac{\partial p}{\partial x} + \frac{hb}{\eta}\tau_{b,x}\right)$ is the volumetric flow rate per unit width due to slip (originating from the slip boundary condition: Eq. (3.9)) and $q_{elastic,x} = \left(-\frac{h^3}{3G}\frac{\partial^2 p}{\partial t \partial x} - \frac{h^2}{2G}\frac{\partial p}{\partial x}\frac{\partial h}{\partial t} + \frac{h^2}{2G}\frac{\partial \tau_{b,x}}{\partial t}\right)$ is the elastic volumetric flow rate per unit width (originating from the elastic part of the constitutive Eq. (3.6)). In the limit $De \ll 1$ and $b = 0$, i.e. $q_{elastic,x} = 0$ and $q_{slip,x} = 0$, this equation reduces to the classical Reynolds lubrication equation for viscous fluids (i.e. Eq. (2.6) in Chapter 2).

We note that the term $u_d \frac{\partial h_d}{\partial x}$ which is present in Eq. (2.6) in Chapter 2 is missing in Eq. (3.11). This is because Eq. (3.11) assumes a frame of reference moving along with the substrate at linear speed U (so that the substrate appears to be rest). On the other hand, Eq. (2.6) in Chapter 2 used the ground frame of reference, in which the substrate moved a linear speed u_d.

Lubricant Driving Forces during HAMR Writing

The deformation of the lubricant during HAMR writing is driven by the thermo-capillary shear stress caused by the spatial temperature gradient (see Subsection "Surface Tension" in Section 2.3 from Chapter 2). Assuming that surface tension γ decreases linearly with temperature, the external shear stress $\boldsymbol{\tau_b} = \tau_{b,x}\boldsymbol{e_x} + \tau_{b,y}\boldsymbol{e_y}$ in Eq. (3.11) for a quasi-parallel film ($|\nabla h| \ll 1$, $\boldsymbol{n} \approx \boldsymbol{e_z}$) is given by

$$\boldsymbol{\tau_b} = \frac{\partial \gamma}{\partial x}\boldsymbol{e_x} + \frac{\partial \gamma}{\partial y}\boldsymbol{e_y} = -c\left(\frac{\partial T}{\partial x}\boldsymbol{e_x} + \frac{\partial T}{\partial y}\boldsymbol{e_y}\right) \tag{3.12}$$

We assume $c \equiv -\frac{d\gamma}{dT} = 0.06\ mN/(m^oC)$ [32]. The co-ordinate system is attached to the moving disk. In this frame, the disk appears to be stationary and the scanning thermal spot moves with speed U. Thus, the disk temperature profile is assumed to be a Gaussian curve with FWHM of 20 nm, moving with linear speed U. To keep the time derivatives finite, we apply the initial rise in temperature as a ramp of 2 ns.

Next, we consider contributions to external pressure p_b. Since lubricant pressure p is independent of z, $p = p_b$. The normal pressures applied to the film are the air bearing pressure, disjoining pressure and laplace pressure (see Figure 2.3 from Chapter 2). Of these, the disjoining pressure has a dominant effect on lubricant diffusion. The timescale of lubricant deformation during HAMR is of the order of ns, while the effect of the air bearing pressure is expected to be on the order of seconds [63] and can be ignored. The laplace pressure can also be ignored unless the surface profile shows a sharp spatial variation [32, 35]. The van der Waals component of disjoining pressure is given by $\Pi_{vdw}(h) = \frac{A_{VLS}}{6\pi(h+d_0)^3}$ [46]. Here A_{VLS} is the Hamaker constant for the vapor-liquid-solid system. d_0 is a constant introduced to account for the finite size of the atoms and molecules within the lubricant film. We use the following values in this study: $A_{VLS} = 1 \times 10^{-19}J$, $d_0 = 0.3$ nm [46]. For lubricants with reactive end-groups, the total disjoining pressure also has electrostatic and structural components [46]. However, for thin films (≤ 1 nm, far from the typical dewetting thickness), the van der Waals component becomes dominant. Thus, p in Eq. (3.11) is given by

$$p = -\Pi(h) = -\frac{A_{VLS}}{6\pi(h+d_0)^3} \tag{3.13}$$

Finally, high temperatures during HAMR writing cause lubricant depletion due to evaporation and degradation. These effects are not considered in this section. The effect of evaporation will be discussed in Chapter 4.

Eq. (3.11) along with Eqs. (3.12), (3.13) describe the evolution of the lubricant height $h(x, y, t)$ under HAMR writing. We first discretize the time derivatives in Eq. (3.11) using the Implicit Euler method. The spatial derivatives are then discretized using the second order accurate finite difference schemes [94].

3.4 Non-linear Viscoelastic Effects

The Linear Maxwell model is not frame invariant and is valid only for small deformation gradients [69]. It is not clear if the linear model is a reasonable approximation to predict the lubricant deformation during HAMR. In order to convincingly answer this question, one would have to simulate the lubricant behavior using a non-linear viscoelastic constitutive equation (for example, differential model like the upper-convected Maxwell model [95] or integral model like the K-BKZ model) and compare the results with the linear model. When De $\gg 1$, Tanner suggests using a non-linear elastic model to predict the rapid deformation behavior of the viscoelastic material [36]. In fact, most non-linear viscoelastic models including the upper-convected Maxwell model and K-BKZ model reduce to some non-linear elastic model when $De \to \infty$. Hence, as a quick check, we compare the results of the Linear Maxwell model in the elastic limit (viscous terms suppressed), with the simplest non-linear elastic model - the incompressible neo-hookean model, which is described by the following equation:

$$\boldsymbol{P} = -p\boldsymbol{F}^{-T} + G\boldsymbol{F} \tag{3.14}$$

Here $\boldsymbol{P}$ is the first Piola-Kirchhoff stress tensor and $\boldsymbol{F}$ is the deformation gradient. G is the shear modulus and p is the pressure (Lagrange multiplier). Eq. (3.14) along with the Cauchy equation of motion (in referential form) and the incompressibility condition form the governing system of equations for the neo-hookean solid:

$$\begin{aligned} \rho_0 \boldsymbol{a} &= \mathrm{Div}\boldsymbol{P} \\ \det\boldsymbol{F} &= 1 \end{aligned} \tag{3.15}$$

Here ρ_0 is the referential density, $\boldsymbol{a}$ is the acceleration. Body forces are ignored. We simulate the behavior of the neo-hookean lubricant under HAMR using an ANSYS FEM model. We compare the results of this model with the prediction of the modified lubrication equation for the Linear Maxwell fluid, with viscous terms suppressed. The idea is to check if the prediction of the Linear Maxwell model (in elastic limit) is close to the neo-hookean result. If this is the case, it would be some justification for the assumption that the effect of the non-linear terms in the general viscoelastic case is small.

3.5 Results

Lubricant Deformation during HAMR: Viscous vs Viscoelastic Behavior

For the baseline simulation, we assume an initially uniform film of Ztetraol of thickness $h_0 =$ 1 nm on the disk. The slip length b is set to 0. The lubricant is subjected to a moving laser spot of FWHM 20 nm at 10 m/s. At t = 0 the laser spot is centered at x = 0, y = 0, hence

at t = 20 ns, the laser spot is at x = 200 nm, y = 0. The resultant temperature profile on the disk is a Gaussian with a peak of 500 °C. Figure 3.3a shows a 3D plot of the lubricant profile after 15 ns of laser heating. Projection of the lubricant profile along the cross-track (y) direction at x = 150 nm is shown in Figure 3.3b. We plot the lubricant profile in the down-track (x) direction (h vs x at y = 0) at 10 ns and 20 ns in Figure 3.4.

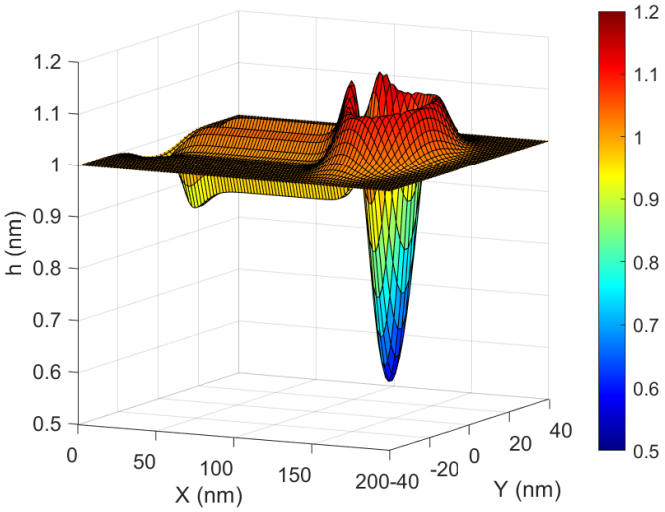

(a) 3D plot of the disk lubricant profile

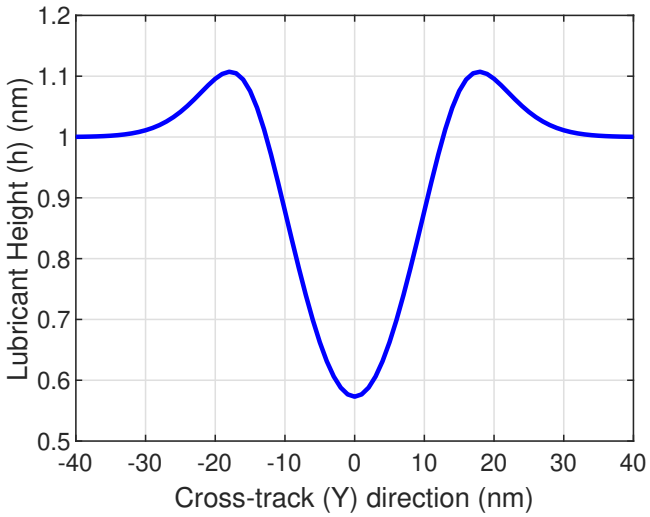

(b) Cross-track disk lubricant profile (at x = 150 nm)

Figure 3.3: Disk lubricant profile (Ztetraol) after 15 ns of laser heating. The moving laser spot is centered at x = 150 nm, y = 0 at t = 15 ns. T_{max} = 500 °C, U = 10 m/s, FWHM = 20 nm, b = 0.

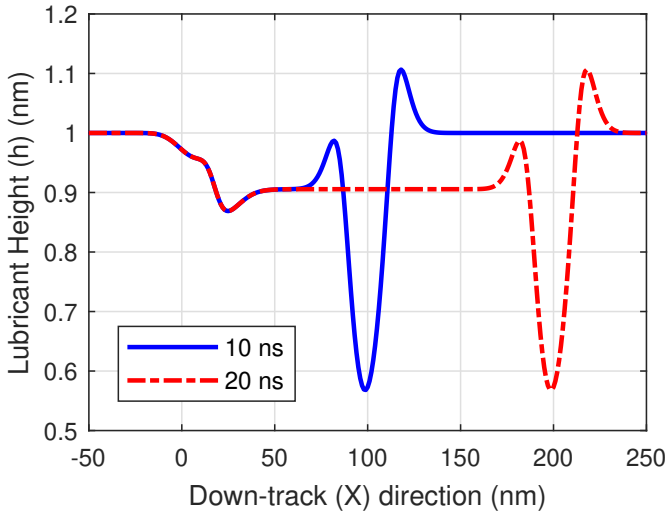

Figure 3.4: Down-track lubricant (Ztetraol) profile (at y = 0) after 10 ns and 20 ns of laser irradiation. T_{max} = 500 °C, U = 10 m/s, FWHM = 20 nm, b = 0.

The lubricant profile is composed of a trough of depth 0.43 nm centered at the instantaneous laser position, with a trail of depth 0.1 nm. As the laser moves forward from x = 100 nm (at 10 ns) to x = 200 nm (at 20 ns), the trough follows the laser instantaneously, thus displaying an elastic behavior. The trail length keeps increasing as the laser moves forward, displaying a characteristic viscous behavior.

In order to distinguish between these two contrasting behaviors, we performed simulations for the viscous limit (elastic terms artificially suppressed: $q_{elastic} = 0$ in Eq. (3.11)) and elastic limit (viscous terms artificially suppressed: $q_{viscous} = 0$ in Eq. (3.11)). We plot the down-track (x) and cross-track (y) profiles of the viscoelastic, viscous and elastic solutions in Figures 3.5a & 3.5b at the end of 15 ns of laser heating. The down-track profile (h vs x) is plotted at y = 0 and the cross-track profile (h vs y) is plotted at x = 150 nm (i.e. at the instantaneous position of the laser at t = 15 ns). The down-track profile shows that the purely elastic solution is composed of an instantaneously moving trough with no trail, whereas the purely viscous solution has no instantaneous trough (just a trail). The viscoelastic solution is a combination of both. The cross-track profile shows that the deformed lubricant width for the elastic/viscoelastic solution is much larger (almost twice) the width of the purely viscous solution. The purely elastic solution leaves behind a small residual trough of depth 0.05 nm between x = -10 nm and x = 40 nm. This trough was found to be a consequence of the initial temperature ramp from t = 0 to t = 2 ns. However, this trough does not affect the solution at later times (the trough moves instantaneously with no trail apart from this initial residual trough) and thus can be ignored for the long term solution.

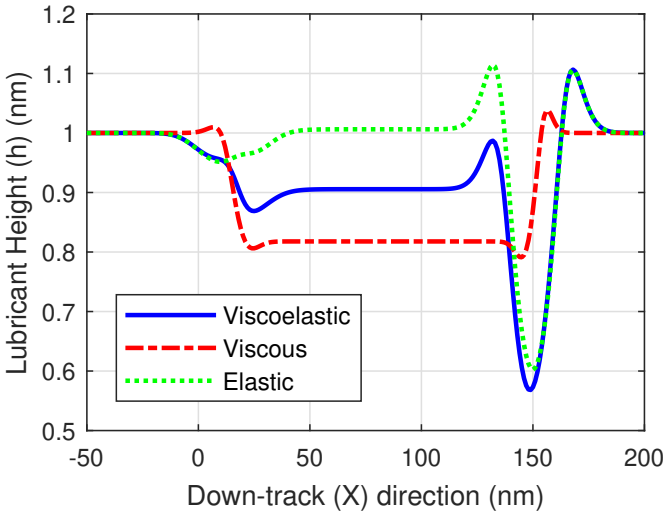

(a) Down-track lubricant profile (at y = 0)

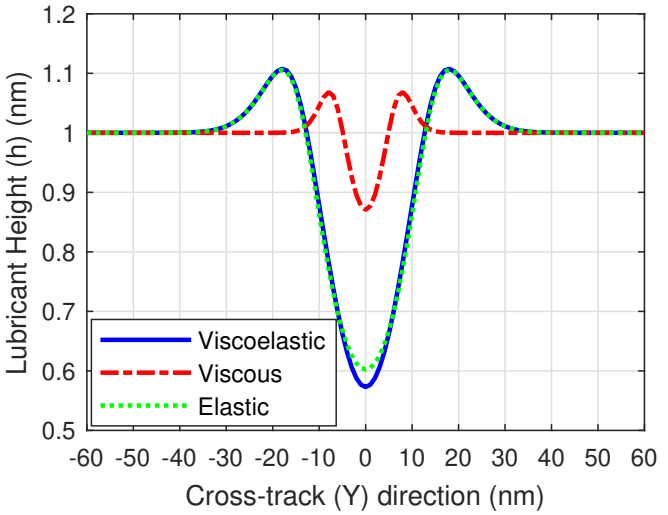

(b) Cross-track lubricant profile (at x = 150 nm)

Figure 3.5: Lubricant profile (Ztetraol) after 15 ns of laser heating - viscous, elastic and viscoelastic profiles. T_{max} = 500 °C, U = 10 m/s, FWHM = 20 nm, b = 0.

Comparison with Sarabi & Bogy

Sarabi & Bogy [37] used a Finite Element ANSYS model to describe the lubricant evolution during HAMR using the integral form of the Linear Maxwell model. This model solves the complete 3D Cauchy equations of motion without the simplifications arising from the lubrication approximation. Here we compare the results of our modified lubrication equation

(3.11) with the ANSYS model proposed in [37]. The ANSYS model uses a lagrangian description of the equations of motion with the initial undeformed lube as the referential configuration. Combining this approach with the lubrication approximation in Section 3.3, we arrive at the following Lagrangian description of lubricant height $h(X,t)$ (assuming no slip i.e. b = 0, no evaporation):

$$\begin{aligned}\frac{\partial h}{\partial t}+\frac{\partial}{\partial X}\left(-\frac{h_0^3}{3\eta}\frac{\partial p}{\partial X}+\frac{h_0^2}{2\eta}\tau_{b,x}\right)+\frac{\partial}{\partial X}\left(-\frac{h_0^3}{3G}\frac{\partial^2 p}{\partial t\partial X}+\frac{h_0^2}{2G}\frac{\partial \tau_{b,x}}{\partial t}\right)\\ +\frac{\partial}{\partial Y}\left(-\frac{h_0^3}{3\eta}\frac{\partial p}{\partial Y}+\frac{h_0^2}{2\eta}\tau_{b,y}\right)+\frac{\partial}{\partial Y}\left(-\frac{h_0^3}{3G}\frac{\partial^2 p}{\partial t\partial Y}+\frac{h_0^2}{2G}\frac{\partial \tau_{b,y}}{\partial t}\right)=0\end{aligned} \tag{3.16}$$

Here h_0 is the initial uniform (undeformed) lubricant height and X, Y are the spatial co-ordinates in the reference configuration (as opposed to x, y from Eq. (3.11) which are the spatial co-ordinates in the current configuration).

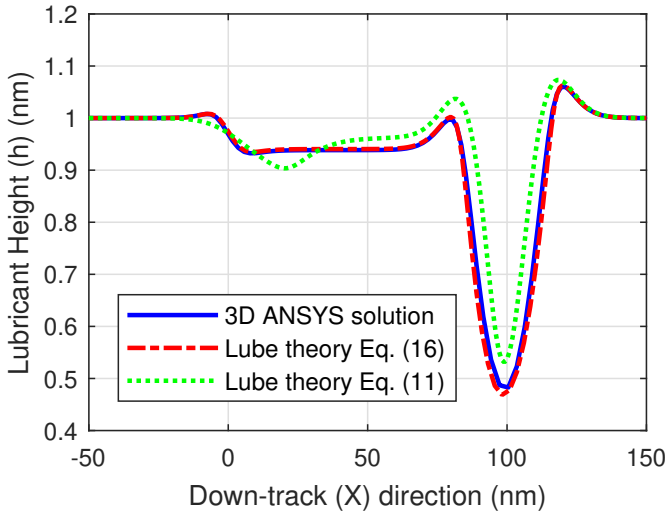

Figure 3.6: Down-track lubricant (Ztetraol) profile (at y = 0) after 10 ns of laser irradiation - Comparison between 3D ANSYS solution [37] and lubrication theory solution using Eqs. (3.11) and (3.16). T_{max} = 500 °C, U = 10 m/s, FWHM = 20 nm, b = 0.

We simulate the deformation of a 1 nm (= h_0) lube under a Gaussian temperature profile with a peak of 500 °C and FWHM of 20 nm, moving at a linear speed U of 10 m/s. Lubricant profiles in the down-track direction (at y = 0) at the end of 10 ns using Eq. (3.11), Eq. (3.16) and the ANSYS model from [37] are plotted in Figure 3.6. The disjoining pressure (given by Eq. (3.13)) is modeled as a linear spring with constant stiffness per unit area of 1.95e+16 N/m^3 (= value of $\frac{\partial p}{\partial h}$ at h = 0.65 nm) in all three models [37]. The ANSYS solution and the solution of Eq. (3.16) agree almost exactly, which confirms the validity of the lubrication

approximation. The solution of Eq. (3.11) has a smaller width and depth than Eq. (3.16). This difference is attributed to the additional approximations involved in deriving Eq. (3.16) as opposed to Eq. (3.11). (Eq. (3.16) assumes that $\frac{\partial}{\partial X} \approx \frac{\partial}{\partial x}$).

Comparison between Linear Maxwell Model in Elastic Limit and Neo-hookean Model

In order to estimate the magnitude of non-linear viscoelastic effects, we study the lubricant deformation during HAMR using the neo-hookean model and compare the results with the solution using the Linear Maxwell model, in the limit $De \to \infty$ (i.e. viscous terms artificially set to 0). To simplify the calculations, we consider a 2D form of the actual 3D problem (in the X-Z plane), where all quantities are assumed to be uniform in the Y direction. The effects of slip, evaporation and disjoining pressure are also ignored for simplicity. Accordingly, the governing equation for lubricant height $h(x,t)$ using the Linear Maxwell model is given by:

$$\frac{\partial h}{\partial t} + \frac{\partial}{\partial x}\left(\frac{h^2}{2G}\frac{\partial \tau_{b,x}}{\partial t}\right) = 0 \tag{3.17}$$

We simulate the deformation of a 1 nm lube for a peak disk temperature of 500 °C and laser

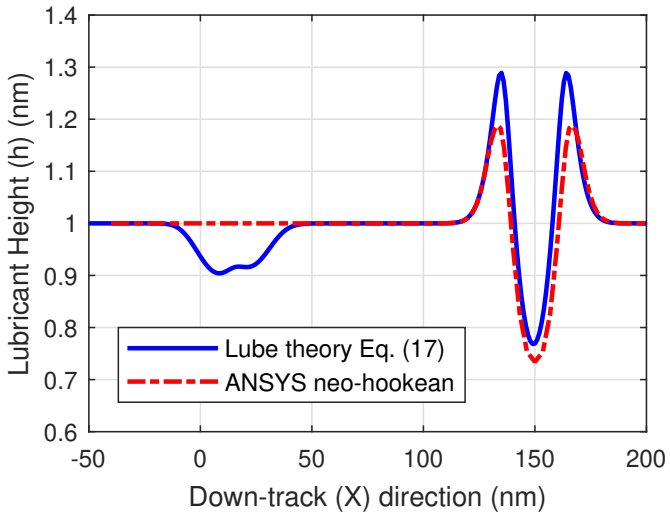

Figure 3.7: Down-track lube profile (Ztetraol) after 5 ns of laser heating. Comparison between ANSYS neo-hookean solution and lubrication theory solution using Eq. (3.17). T_{max} = 500 °C, U = 30 m/s, FWHM = 20 nm, b = 0.

FWHM of 20 nm. The laser speed U is kept high (30 m/s) so that the Deborah number is high and the error by setting the viscous terms to 0 is small. The lubricant profile in the

down-track direction (x) at the end of 5 ns using Eq. (3.17) and the 2D neo-hookean ANSYS model is plotted in Figure 3.7. We see that both solutions show the same behavior - an elastic trough centered at the instantaneous laser spot, with no trail. The only difference is that the Linear Maxwell solution leaves behind a small residual trough of depth $\sim$ 0.1 nm between x = -10 nm and x = 40 nm, as explained in section "Lubricant Deformation during HAMR: Viscous vs Viscoelastic Behavior". Both solutions have nearly the same trough width ($\sim$ 30 nm) and similar trough depths (min h is 0.77 nm for Linear Maxwell solution vs 0.74 nm for neo-hookean solution). The height of the side ridges is slightly larger for the neo-hookean model (max. h is 1.29 nm for Linear Maxwell solution vs 1.19 nm for neo-hookean solution). These differences are expected to be even smaller after including disjoining pressure in both models. We thereby argue that the modified lubrication Eq. (3.11) is a reasonable approximation to predict lubricant deformation during HAMR.

Effect of Slip

In this section, we investigate the effect of slip length b on the lubricant behavior. The viscous and the slip volume flow rate (per unit width) terms in the governing Eq. (3.11) can be coupled together as: $q_{x,net-viscous} = \left(-\frac{h^3}{\eta}\frac{\partial p}{\partial x}\left(\frac{1}{3}+\frac{b}{h}\right)+\frac{h^2}{\eta}\tau_{b,x}\left(\frac{1}{2}+\frac{b}{h}\right)\right)$. We observe that b increases the magnitude of the viscous terms and does not (explicitly) affect the magnitude of the elastic terms. This is because the slip boundary condition (3.9) assumes that the slip velocity depends linearly on the wall shear stress $\tau_{xz}|_{z=0}$, $\tau_{yz}|_{z=0}$ (and not on the shear stress rate $\frac{\partial \tau_{xz}}{\partial t}|_{z=0}$, $\frac{\partial \tau_{yz}}{\partial t}|_{z=0}$). A memory slip boundary condition in which slip velocity depends on the history of the wall shear stress would affect both the viscous and elastic terms [96]. We plot the lubricant thickness after 10 ns of laser irradiation for four values of slip length: 0, 1, 3, 5 nm in Figs. 3.8a & 3.8b. As b is increased, we observe larger deformations, in particular, a larger viscous trail in the down-track profile, as expected. The cross-track profile depth also increases (i.e. larger deformation) on increase in b, but the profile width reduces. The reduction in cross-track profile width is another indicator of a change from elastic to viscous behavior (Refer Figure 3.5b), on increase in slip length.

Effect of Shear Modulus

In this section, we keep the thin-film viscosity $\eta_{eff}(T)$ fixed ($\eta_{eff} = 13 \times \eta_{bulk}$) and vary the shear modulus G_{eff} from 0.5 MPa to 0.1 MPa. A shear modulus of 0.5 MPa assumes that the maxwell relaxation time of the thin film lubricant is the same as the bulk lubricant (i.e. $\eta_{eff} = 13 \times \eta_{bulk}$, $G_{eff} = 13 \times G_{bulk}$, $\lambda_{eff} = \lambda_{bulk}$). As G_{eff} is decreased, the enhancement factor of 13 is partially absorbed by the Maxwell relaxation time and partially by the shear modulus. In particular, for $G_{eff} = 0.1$ MPa, $G_{eff} = 2.8 \times G_{bulk}$ and $\lambda_{eff} = 4.6 \times \lambda_{bulk}$). As the shear modulus is decreased and the maxwell relaxation time is increased, the elastic deformation increases significantly (Figure 3.9).

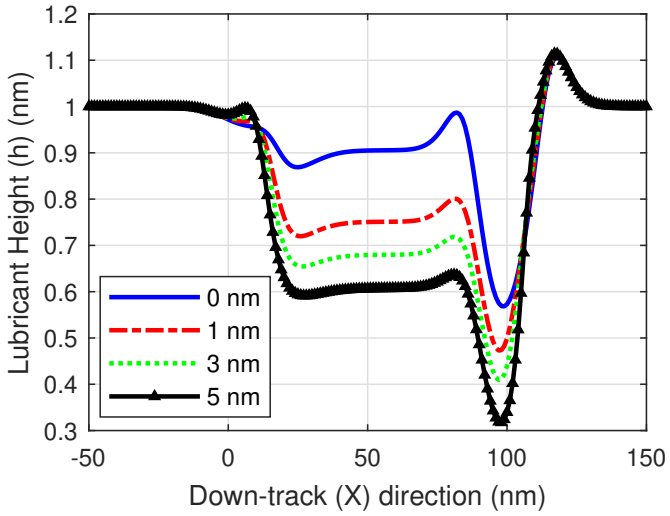

(a) Down-track lubricant profile (at y = 0)

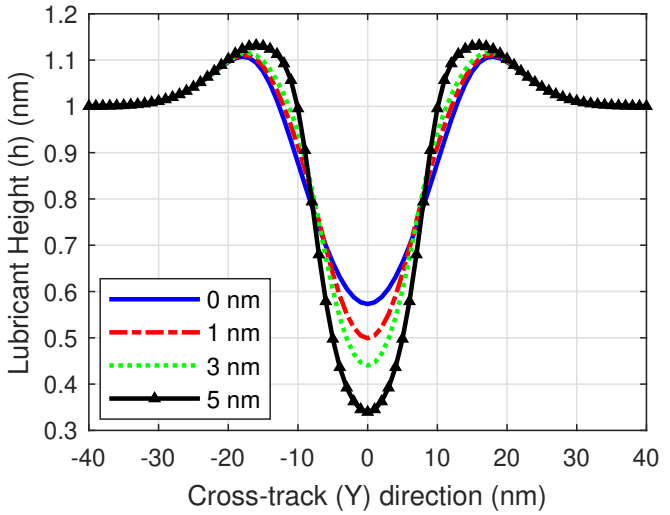

(b) Cross-track lubricant profile (at x = 100 nm)

Figure 3.8: Lubricant profile (Ztetraol) after 10 ns of laser heating. Slip Length b is varied from 0 to 5 nm. T_{max} = 500 °C, U = 10 m/s, FWHM = 20 nm.

Effect of Disk Velocity

Here we study the effect of varying the laser speed (i.e. disk velocity) on the lubricant profile, a consequence of varying the disk rotational speed. All other parameters such as disk temperature (i.e. laser power), laser FWHM and slip length were kept fixed. As the laser speed increases, the Deborah number increases ($De = \frac{\lambda U}{L}$) and hence the lubricant

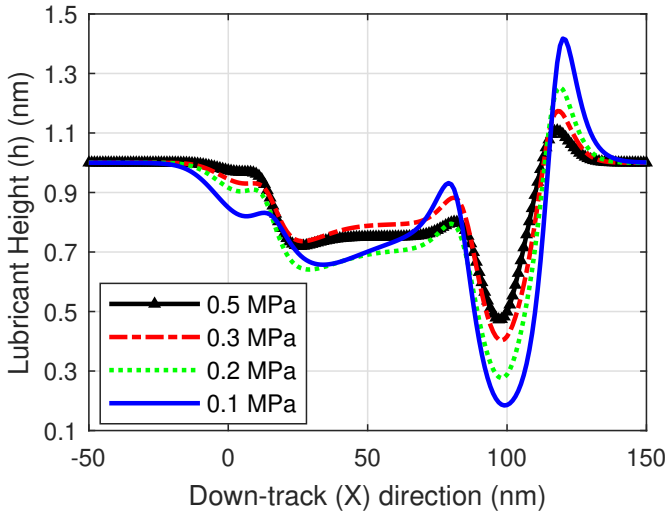

Figure 3.9: Down-track lube (Ztetraol) profile (at y = 0) after 10 ns of laser heating. Shear Modulus G_{eff} is varied from 0.1 to 0.5 MPa with $\eta_{eff}(T)$ kept fixed. T_{max} = 500 °C, U = 10 m/s, FWHM = 20 nm, b = 1 nm.

is expected to behave more elastically and less viscously. Figure 3.10 shows plots of the lubricant profiles for four laser speeds: U = 5 m/s, 10 m/s, 20 m/s, 40 m/s after $\frac{150}{U}$ ns (U in m/s) of laser heating. As U is increased, the depth of the viscous trail behind the elastic trough decreases. At lower disk speeds, the lubricant has more time to respond to the laser excitation and hence leaves a larger viscous trail behind the moving laser spot.

3.6 Discussion

Our simulations indicate that PFPE lubricants exhibit a combination of viscous and elastic behavior at the timescale of HAMR. When subjected to a scanning laser spot of 20 nm FWHM at 10 m/s, the disk lubricant profile consists of an elastic trough centered at the instantaneous laser location, followed by a viscous trail (Figure 3.4). The viscous vs elastic behavior of the lubricant is a function of the Deborah number, De = $\frac{\lambda U}{L}$. As the laser velocity (U) is increased from 5 m/s to 40 m/s a change in lubricant behavior from viscous to elastic is observed (Figure 3.10).

In order to estimate the magnitude of non-linear viscoelastic effects, we compared the lubricant deformation using the non-linear elastic neo-hookean model with our Linear Maxwell model, in the limit $De \to \infty$ (Figure 3.7). Our results suggest that the non-linear effects are relatively small in the elastic limit; nevertheless, the model presented here can be improved by using a non-linear viscoelastic constitutive equation. We also compare the results of our modified lubrication equation with the 3D ANSYS model proposed by Sarabi & Bogy [37].

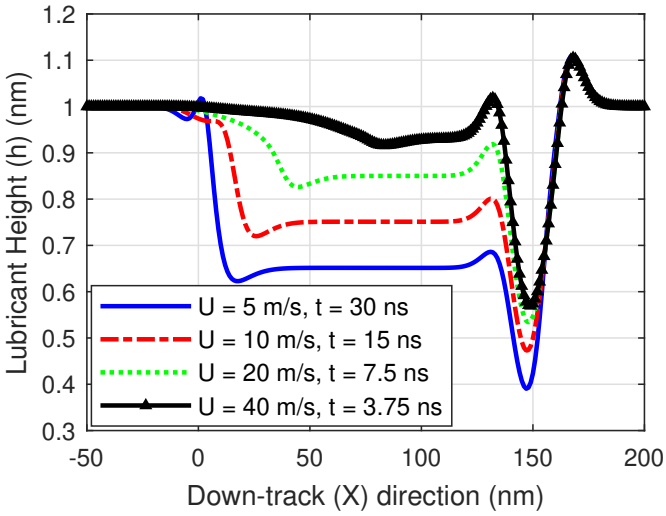

Figure 3.10: Down-track lube (Ztetraol) profile (at y = 0) after $\frac{150}{U}$ ns of laser heating, U is varied from 5 to 40 m/s. T_{max} = 500 °C, FWHM = 20 nm, b = 1 nm.

We find a good agreement between both models, validating the lubrication approximation (Figure 3.6).

The high thermo-capillary stress on the lubricant during HAMR would likely be effective at debonding the functional groups from the disk, thereby promoting lubricant slippage [86]. Due to the lack of experimental data for the value of slip lengths at the HDI, we conduct a parametric study of the effect of slip on lubricant deformation. As the slip length is increased, the lubricant flow rate increases, causing larger deformations (Figures 3.8a & 3.8b). With the Navier slip boundary condition (linear dependence of slip velocity on shear stress), slip increases the net viscous flow rate, causing a change in behavior from elastic to viscous.

3.7 Conclusion

We have introduced a modification to the traditional Reynolds lubrication equation using the Linear Maxwell constitutive equation and a slip boundary condition. We have used this equation to predict the deformation of the disk lubricant due to HAMR laser heating under the influence of thermo-capillary stress and disjoining pressure. When subjected to a 20 nm FWHM scanning laser spot, the lubricant profile consists of an elastic trough centered at the instantaneous laser location, followed by a viscous trail. Slippage increases the flow rate of the lubricant, causing larger viscous deformations.

This chapter presents work published in Tribology Letters (reprinted by permission from Springer Nature (Tribology Letters) [97], Copyright (2018)) and IEEE Transactions on Magnetics (© 2018 IEEE. Reprinted, with permission, from [98]).

Chapter 4

Viscoelastic model for Disk-to-Head Lubricant Transfer and Disk Lubricant Recovery During HAMR

4.1 Introduction

As noted in Chapter 2, a major tribological challenge in HAMR is the creation of write-induced head contamination at the near field transducer (NFT) [29, 30, 43, 99–101]. A likely cause of this contamination is lubricant desorption from the disk and adsorption on the head through thermodynamic driving forces [29]. During HAMR, the media is locally heated to its Curie temperature (~ 500 °C), causing the disk lubricant to evaporate and form vapor in the air bearing. The peak temperature of the head is lower than that of the disk (~ 300 °C). This temperature difference causes the lubricant to evaporate from the disk and condense on the relatively cooler head. The lubricant acts as a carrier, causing a continuous deposition of media contaminants at the NFT. To test this hypothesis, Tani et al. used a pin-on-disk test to demonstrate smear growth on the pin surface when lubricated disk with adsorbed contaminant, siloxane was exposed to laser heating [101].

In Chapter 2, we presented a viscous continuum model that predicts the media-to-head lubricant transfer during HAMR for the PFPE lubricant, Zdol. This model determines the thermo-capillary stress driven deformation and evaporation of the lubricant film on the disk, the convection/diffusion of the lube vapor in the air bearing and the evolution of the condensed lubricant on the head. However, this model assumes a viscous constitutive law for the lubricant, which in reality is a viscoelastic fluid.

In this chapter, we improve the viscous disk-to-head lubricant transfer model from Chapter 2 to include the effect of viscoelasticity and slip on lubricant transfer. We utilize the viscoelastic lubricant model presented in Chapter 3 to develop a viscoelastic disk-to-head lubricant transfer model for HAMR writing. We study the effect of lubricant type (Zdol vs Ztetraol), molecular weight, slip length, disjoining pressure, head/media temperatures,

initial lubricant thickness and laser spot size on the transfer process.

Finally, it is also vital for the lubricant to sufficiently recover the depletion and accumulation zones after the HAMR laser is removed to ensure stable flying heights and reliable read/write performance. Hence, we also study the recovery of the viscoelastic lubricant after removal of the HAMR laser.

4.2 Viscoelastic Model for Disk-to-Head Lubricant Transfer

During HAMR writing, the media is locally heated to its Curie Temperature ($T_{max,d} \sim 500^oC$), causing the disk lubricant (thickness h_d) to deform and evaporate. Evaporation increases the partial pressure of the lubricant vapor in the air bearing, p_v. Some of this vapor condenses on the relatively cooler slider surface ($T_{max,s} \sim 300^oC$), depositing a film of thickness h_s. Thus, we have three unknown profiles - $h_d(x, y, t)$, $h_s(x, y, t)$ and $p_v(x, y, t)$. A schematic of this media-to-head lubricant transfer is shown in Fig. 4.1.

We consider two frames of reference: frame 1, which is attached to the disk and frame 2, which is attached to the slider. In frame 1, the disk is stationary and the head (and the laser spot) move with speed U along the down-track (x) direction (Figure 4.1). In frame 2, the head is stationary and the disk moves (backwards) with speed U. In this study, we investigate lubricant transfer of two PFPE lubricants - Zdol (M_w = 1.5, 2, 2.5 kg/mol) and Ztetraol (M_w = 2.7 kg/mol).

Governing Equation for Disk Lubricant

The governing equation for the disk lubricant profile $h_d(x, y, t)$ is given by Eq. (3.11), along with Eqs. (3.12), (3.13) (from Chapter 3) in frame 1 (h replaced by h_d). The net evaporation rate $\dot{m}_d$ from the disk in Eq. (3.11) is determined using the Hertz-Knudsen-Langmuir law:

$$\dot{m}_d = \sqrt{\frac{M_w}{2\pi R T_d}} \left(p_{vap,thin} - p_v\right) \tag{4.1}$$

Here M_w is the lubricant molecular weight, R is the molar universal gas constant, T_d is the disk lubricant temperature, $p_{vap,thin}$ is the equilibrium vapor pressure of the thin-film lubricant, p_v is the partial pressure of the lubricant vapor in the air bearing. $p_{vap,thin}$ is given by the following equation: [32]

$$p_{vap,thin} = p_{vap,\infty} exp\left(-\frac{M_w}{\rho R T_d}\pi(h_d)\right) \tag{4.2}$$

Here $p_{vap,\infty}$ is the bulk vapor pressure of the lubricant, ρ is the (liquid) lubricant density and $\pi(h_d)$ is the disjoining pressure (see Eq. (3.13) from Chapter 3). The equation for p_v

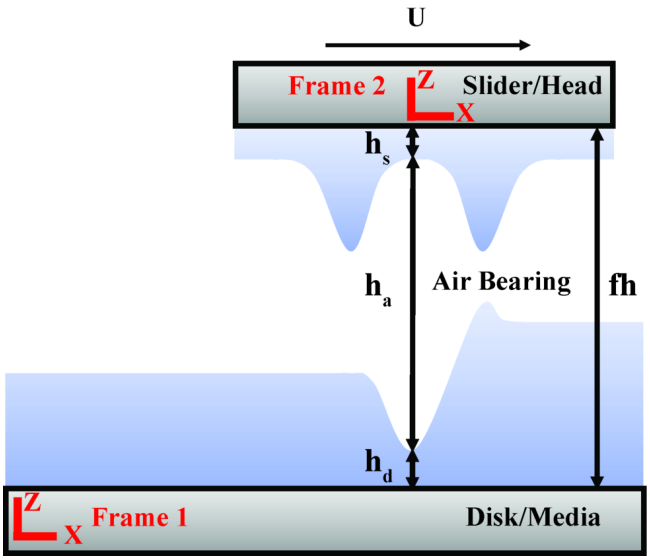

Figure 4.1: HAMR lubricant transfer schematic (as seen from frame 1, which is attached to the disk): Disk lubricant of thickness h_d is subjected to a scanning laser spot of speed U. The disk lubricant evaporates to form vapor having partial pressure p_v in the HDI. The vapor condenses on the slider to form a film of thickness h_s.

will be discussed in the subsequent section "Governing Equation for Lubricant Vapor".

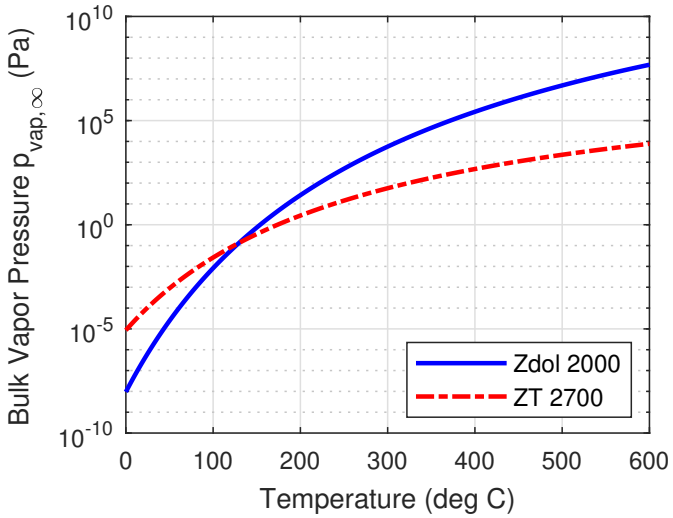

Figure 4.2: Bulk equilibrium vapor pressure $p_{vap,\infty}$ versus temperature for Zdol 2000 [6] and Ztetraol 2700 [79, 102].

Karis gives the bulk vapor pressure $p_{vap,\infty}$ of Zdol as a function of temperature and molecular weight using the Clausius-Clapeyron equation [6]. This evaporation model for Zdol has been used in previous numerical studies [32] and was also used in Chapter 2. The temperature dependent $p_{vap,\infty}$ for Ztetraol 2700 is obtained with parameters extracted using the Clausius-Clapeyron equation and the measured data in Ref [102], which yields a heat of vaporization of 68.112 kJ/mol and a pre-exponential term of 685,415 Torr. This model was used by Jones et al. [79] to predict lubricant depletion in Ztetraol 2700 and was found to agree well with experimental data. $p_{vap,\infty}$ for Zdol and Ztetraol is plotted versus temperature in Figure 4.2.

Governing Equation for Lubricant Vapor

Consistent with the lubrication approximation, we assume that the density of the lubricant vapor in the air bearing, ρ_v is independent of z, i.e., $\rho_v \equiv \rho_v(x, y, t)$. The governing equation for the lubricant vapor can be obtained by integrating the continuity equation along z and applying Fick's Law of Diffusion [44].

$$\begin{aligned} &\frac{\partial}{\partial t}(\rho_v h_a) + \frac{\partial}{\partial x}(\rho_v q_x) + \frac{\partial}{\partial y}(\rho_v q_y) = \\ &\frac{\partial}{\partial x}\left(D h_a \frac{\partial \rho_v}{\partial x}\right) + \frac{\partial}{\partial y}\left(D h_a \frac{\partial \rho_v}{\partial y}\right) + \dot{m}_d + \dot{m}_s \end{aligned} \tag{4.3}$$

Here $h_a \equiv (fh - h_s - h_d)$ is the air bearing height where fh is the constant head-disk spacing at the NFT (Refer Fig. 4.1). $q_x \equiv \int_{h_d}^{h_d+h_a} v_{a,x} dz$ and $q_y \equiv \int_{h_d}^{h_d+h_a} v_{a,y} dz$ are the volume flow rates per unit length in the x and y directions, obtained by integrating the air bearing velocity $v_{a,x}$ and $v_{a,y}$ (in frame 1) along z across the air bearing clearance. D is the lubricant vapor diffusivity in air and $\dot{m}_d$, $\dot{m}_s$ are the net evaporation mass fluxes from the disk and slider lubricant films respectively. We note that the same equation was used in our viscous disk-to-head lubricant transfer model presented in Chapter 2.

We assume that the effects of the lubricant vapor on the air bearing pressure, temperature and velocity can be neglected. Also, the lubricant as well as air bearing temperature is simply assumed to be equal to the average of the disk and slider temperatures: $T_v \equiv (\frac{T_s+T_d}{2})$. Finally, the lubricant vapor density ρ_v and partial pressure P_v are assumed to be related by the ideal gas law:

$$P_v = \frac{\rho_v R T_v}{M_w} \tag{4.4}$$

Our results from Chapter 2 showed that convection has a small impact on the lubricant transfer process, however, the effect of diffusion is significant (see Figure 2.11 from Chapter 2). Hence, we ignore the convective terms in Eq. (4.3). Diffusion coefficient D is obtained using the Hirschfelder approximation [6].

Governing Equation for the Slider Lubricant

We solve for the evolution of the lubricant film on the slider in frame 2. In this frame, the slider is stationary and the disk is moving with speed U. The temperature profile of the slider lubricant is a (stationary) Gaussian curve with FWHM of 20 nm and peak temperature $T_{max,s} = 300^oC$. In this frame, the governing equation for the slider lube thickness $h_s(x, y, t)$ is again given by Eq. (3.11), along with Eqs. (3.12), (3.13) from Chapter 3 (h replaced by h_s). Since the temperature profile on the slider does not change with time, the thermo-capillary stress is also independent of time (Eq. (3.12)), $\frac{\partial \tau_{b,x}}{\partial t} = 0$, $\frac{\partial \tau_{b,y}}{\partial t} = 0$ and thus the lubricant has a predominantly viscous behavior (apart from the initial 2 ns ramp in temperature).

4.3 Results: Disk-to-Head Lubricant Transfer

Evaporation versus Thermo-capillary Stress

Using viscous simulations for Zdol at 350 °C, Dahl & Bogy [32] found that thermo-capillary stress dominates for small spot sizes (< 50 nm), whereas evaporation dominates for large spot sizes ($\sim 1\mu$m). Here we investigate the relative importance of thermo-capillary stress vs evaporation for the viscoelastic lubricants Zdol, Ztetraol at different temperatures and spot sizes.

Figures 4.3a & 4.3b plot the disk lubricant profile for Zdol with and without evaporation for laser FWHM of 20 nm and 1 μm and peak disk temperatures of 350 and 500 °C. For peak temperature of 350 °C, the profiles with and without evaporation are close (Cases c1 and c2) and thus thermo-capillary stress dominates for spot size of 20 nm, as reported in [32]. However, at higher temperature of 500 °C (Cases a1 and a2), evaporation dominates (even for small spot size of 20 nm). For larger spot size of 1 μm (Cases b1 and b2), evaporation becomes even more dominant. Another interesting observation is that as the spot size is increased from 20 nm to 1 μm, the Deborah number decreases ($De = \frac{\lambda U}{L}$) and hence the lubricant behavior changes from viscoelastic (Case a1: elastic trough + viscous trail) to purely viscous (Case b1: only viscous trail). We thus conclude that evaporation is the dominant mechanism for Zdol at high temperatures ($\sim$ 500 °C) for all spot sizes (20 nm to 1 μm).

Figure 4.4 plots the deformation of the disk lubricant for Ztetraol with and without evaporation for laser FWHM of 20 nm (Figure 4.4a) and 1 μm (Figure 4.4b) and a maximum disk temperature of 500 °C. For the smaller spot size of 20 nm, the profiles with and without evaporation are almost indistinguishable (Cases a1 and a2) and thus thermo-capillary stress dominates, even at the high temperature of 500 °C (unlike Zdol). However, for larger spot size of 1 μm (Cases b1 and b2), evaporation dominates. Additionally, as the spot size is increased from 20 nm to 1 μm, the Deborah number decreases ($De = \frac{\lambda U}{L}$) and hence the lubricant behavior changes from viscoelastic (Case a1: elastic trough + viscous trail) to purely viscous (Case b1: only viscous trail).

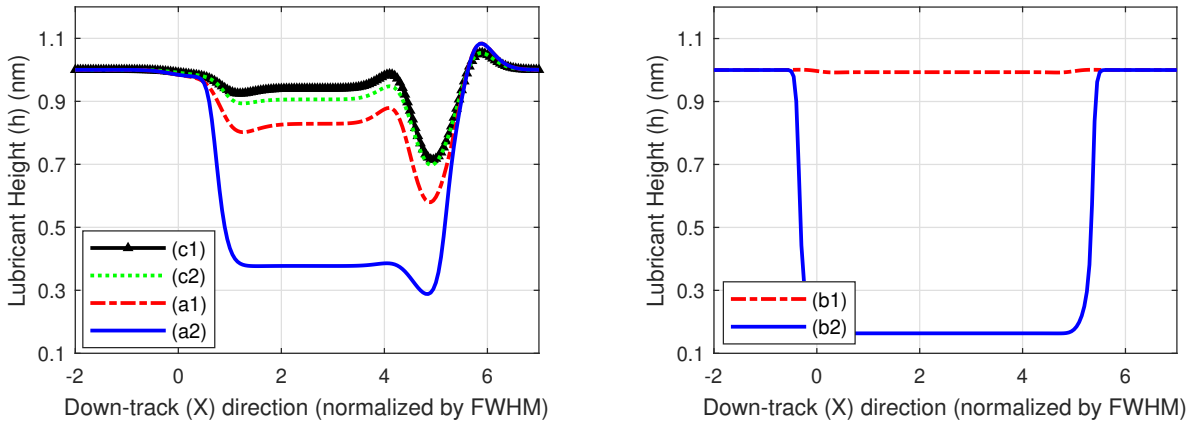

(a) Cases (c1), (c2), (a1), (a2)

(b) Cases (b1) & (b2)

Figure 4.3: Down-track disk lubricant profile with and without evaporation for Zdol 2000 after 10 ns of laser heating with $T_{max,d}$ = 350 °C, 500 °C and Laser FWHM = 20 nm, 1 μm. U = 10 m/s, b = 1 nm. Case description:

(c1) Without Evaporation, 350 °C, 20 nm, 10 ns

(c2) With Evaporation, 350 °C, 20 nm, 10 ns

(a1) Without Evaporation, 500 °C, 20 nm, 10 ns

(a2) With Evaporation, 500 °C, 20 nm, 10 ns

(b1) Without Evaporation, 500 °C, 1 μm, 0.5 μs

(b2) With Evaporation, 500 °C, 1 μm, 0.5 μs

The disparity between the dominant mechanism for Zdol vs Ztetraol at 500 °C and 20 nm (evaporation and thermo-capillary stress respectively) is due to the difference in vaporization properties of both lubricants. The bulk vapor pressure of Zdol at 500 °C is 4.9 MPa, while the same value for Ztetraol is only 2.3 kPa (Figure 4.2). This 3 orders of magnitude difference in the vapor pressure causes the evaporation rate in Zdol to be much larger than that for Ztetraol.

Comparison between Zdol and Ztetraol Transfer

We assume an initially uniform film of Zdol 2000/Ztetraol 2700 of thickness $h_{0,d}$ = 1 nm on the disk. To avoid singularities, we set the initial lube thickness on the slider ($h_{0,s}$) to 0.3 nm. The slip length b is 1 nm. The disk lubricant is subjected to a moving laser spot of

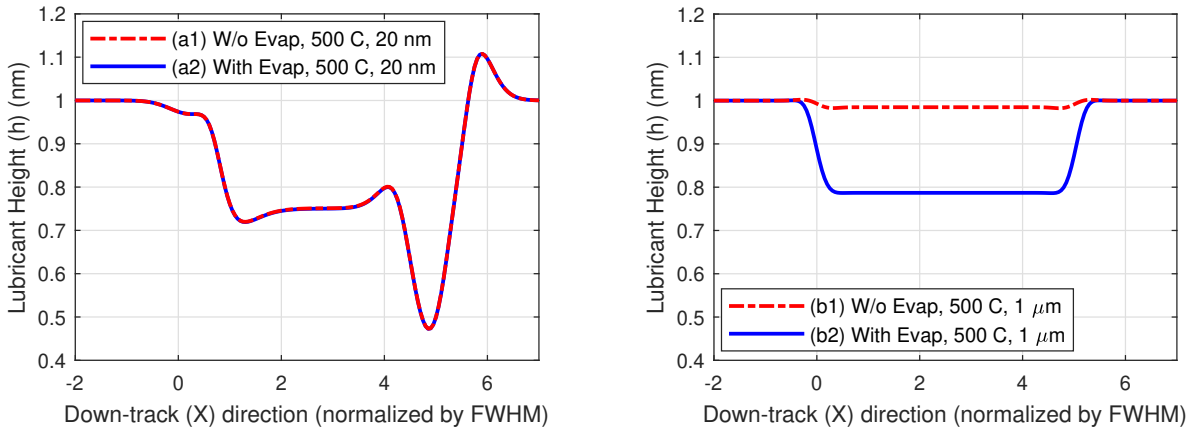

(a) Cases (a1) & (a2)

(b) Cases (b1) & (b2)

Figure 4.4: Down-track disk lubricant profile with and without evaporation for Ztetraol 2700 with $T_{max,d}$ = 500 °C and Laser FWHM = 20 nm and 1 μm respectively. U = 10 m/s, b = 1 nm. Case description:

(a1) Without Evaporation, 500 °C, 20 nm, 10 ns

(a2) With Evaporation, 500 °C, 20 nm, 10 ns

(b1) Without Evaporation, 500 °C, 1 μm, 0.5 μs

(b2) With Evaporation, 500 °C, 1 μm, 0.5 μs

FWHM 20 nm at U = 10 m/s. The NFT center/laser spot center is located at $y = 0$ and $x = Ut$ at time t in frame 1. The resultant temperature profile on the disk and slider is a Gaussian with a peak of 500 °C and 300 °C respectively. To keep the time derivatives finite, we apply the initial rise in temperature on the disk/slider as a ramp of 2 ns. The head-disk clearance fh is 4 nm.

Figures 4.5a & 4.5b show the time evolution of the lubricant profiles on the disk (bottom curves) and the slider (top curves) in the cross-track and down-track directions for Zdol 2000, as viewed from frame 1. The down-track profile is plotted at y = 0, the cross-track profile is plotted at $x = Ut$ (i.e. at instantaneous location of laser spot/NFT). In frame 1, the disk is stationary and the slider is moving, hence the slider lubricant profile moves forward in the down-track direction as time proceeds. On the disk, the length of the depleted region increases as the scanning laser moves forward in the down-track direction. As disk lubricant depletion increases with time, lubricant accumulation on the head grows. The simulation predicts a peak lube height of 1.7 nm on the slider after 8 ns.

Figures 4.6a & 4.6b show the time evolution of lubricant profiles on the disk (bottom

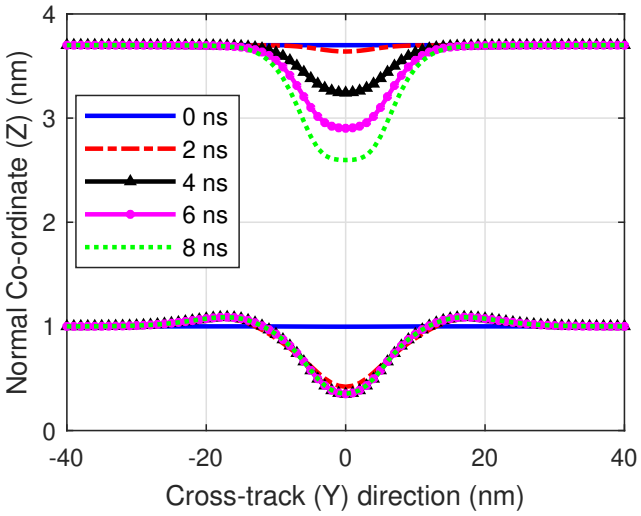

(a) Cross-track lubricant profile

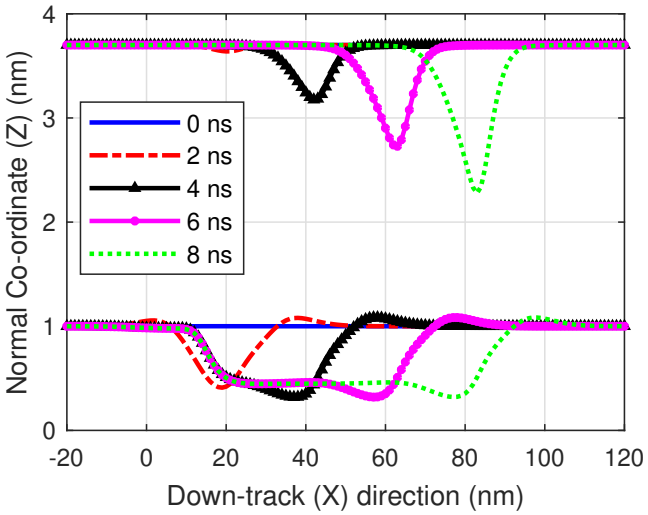

(b) Down-track lubricant profile

Figure 4.5: Disk and slider lubricant profiles at different times of laser irradiation in cross-track and down-track directions for Zdol 2000. $T_{max,d}$ = 500 °C, $T_{max,s}$ = 300 °C, U = 10 m/s, FWHM = 20 nm, b = 1 nm.

curves) and the slider (top curves) in the cross-track and down-track directions for Ztetraol, as viewed from frame 1. We observe a significant difference between the rates of lubricant transfer for Zdol vs Ztetraol. While lubricant transfer occurs on a time scale of ns for Zdol, lubricant pick-up occurs on a time scale of μs for Ztetraol. This can be attributed to the difference in vaporization properties of both lubricants - bulk vapor pressure of Zdol at 500

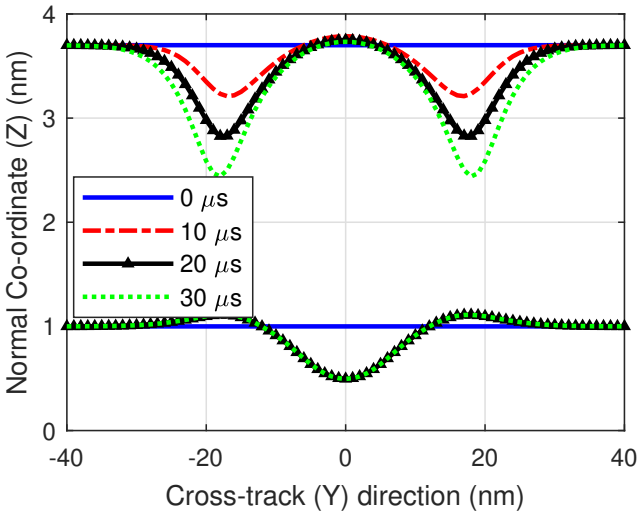

(a) Cross-track lubricant profile at t = 0, 10, 20, 30 μs

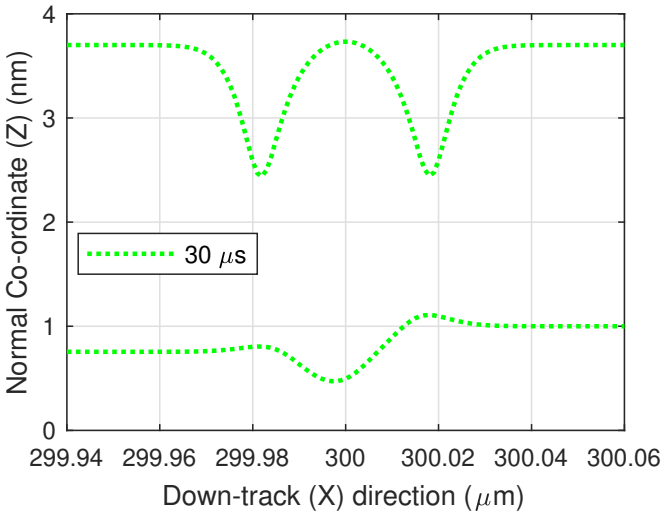

(b) Down-track lubricant profile at t = 30 μs

Figure 4.6: Disk and slider lubricant profiles at different times of laser irradiation in cross-track and down-track directions for Ztetraol 2700. $T_{max,d}$ = 500 °C, $T_{max,s}$ = 300 °C, U = 10 m/s, FWHM = 20 nm, b = 1 nm.

^oC is 4.9 MPa, while that for Ztetraol is only 2.3 kPa (Figure 4.2).

The shape of the slider lubricant profile is also different for the two lubricants. For Zdol, the slider lubricant height is maximum at the NFT center and the lubricant height decreases radially away from the NFT (Figures 4.5a & 4.5b). On the other hand, for Ztetraol, we see a minima in the slider lubricant height at the NFT center (Figures 4.6a & 4.6b). Radially

away from the NFT, the head lubricant thickness initially increases, achieves a maximum at a radial position of $\sim$ 18 nm and thereafter decreases. This difference can be explained by the relative dominance of evaporation/condensation vs thermo-capillary stress. For Zdol, disk lubricant evaporation rate is so high that condensation of lubricant onto the slider dominates over thermo-capillary stress. Since the disk temperature is maximum at the NFT center, the evaporation rate and slider lubricant height are also maximized here. On the other hand, with much slower evaporation rate for Ztetraol, thermo-capillary stress dominates and hence a minima of slider lubricant height is observed at the NFT center (where the slider temperature is maximum). The condensed lubricant is pushed away from the NFT center by the thermo-capillary stress, causing the observed lump of accumulated lubricant at a radial position of $\sim$ 18 nm from the NFT center.

Effect of Lubricant Molecular Weight

In order to investigate the effect of lubricant molecular weight on the transfer dynamics, we performed simulations for Zdol with 3 different molecular weights - 1.5, 2 and 2.5 kg/mol. All other properties of the lubricants (viscosity, shear modulus, disjoining pressure) are assumed to be the same. As the molecular weight is increased, the equilibrium vapor pressure as well as evaporation rate decreases (lighter molecules evaporate faster) [6]. Hence, the amount of lubricant transfer for the low molecular weight lubricant is larger than that for the high molecular weight lubricant (Figure 4.7).

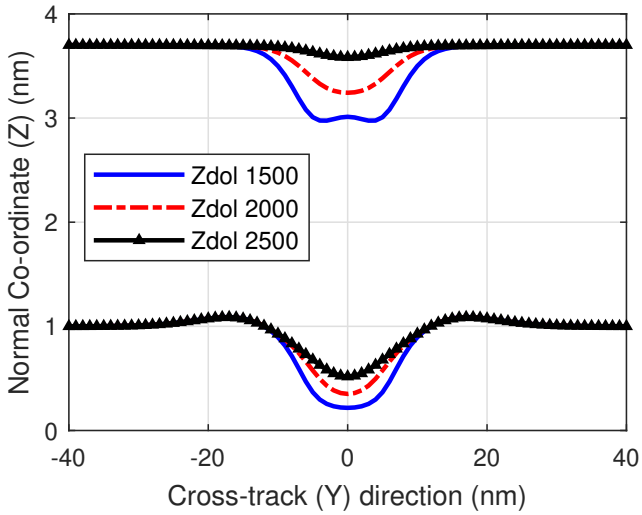

Figure 4.7: Disk and slider lubricant profiles in cross-track direction after 4 ns of laser irradiation for Zdol 1500, 2000 and 2500. $T_{max,d}$ = 500 °C, $T_{max,s}$ = 300 °C, U = 10 m/s, FWHM = 20 nm, b = 1 nm.

Viscous vs Viscoelastic Solution

In this section, we compare the viscoelastic solution with the purely viscous case (elastic terms artificially suppressed: $q_{elastic} = 0$ in Eq. (3.11) from Chapter 3). We plot the cross-track lubricant profile (Ztetraol) on disk and head at the end of 10 μs of laser irradiation for the viscoelastic and purely viscous cases in Figure 4.8. The slip length b is set to 1 nm. All other parameters are same as the Ztetraol simulation from Section "Comparison between Zdol and Ztetraol Transfer". Similar to Figure 3.5b from Chapter 3, the deformed lubricant width on the disk for the viscoelastic solution is much larger (almost twice) the width of the purely viscous solution. The depth of the deformed viscoelastic solution on the disk is also larger than the viscous solution.

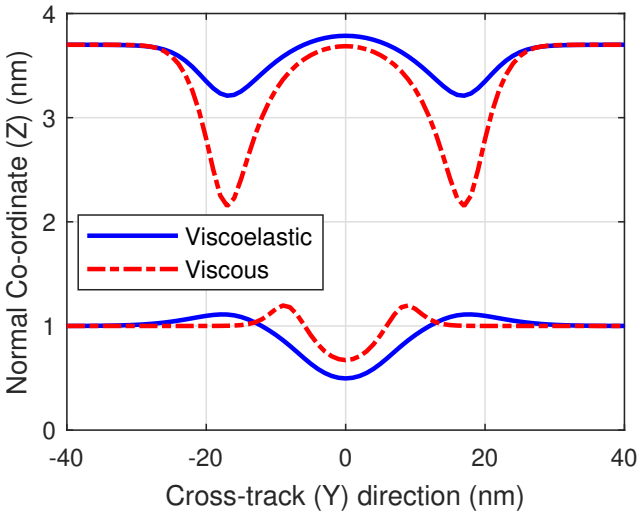

Figure 4.8: Disk and slider lubricant profiles in cross-track direction after 10 μs of laser irradiation for Ztetraol - viscoelastic vs viscous solution. $T_{max,d} = 500$ °C, $T_{max,s} = 300$ °C, $U = 10$ m/s, FWHM = 20 nm, b = 1 nm.

Disjoining pressure suppresses the equilibrium vapor pressure of the thin film lubricant (Eq. (4.2)). If the lubricant thickness h_d is smaller, its disjoining pressure is larger (Eq. (3.13) from Chapter 3) and hence its thin-film equilibrium vapor pressure and evaporation rate are smaller. The disk lubricant thickness of the viscoelastic solution is smaller than the viscous solution (near the laser spot center), causing the evaporation rate from the disk to be smaller, compared to the viscous solution. Hence, the amount of condensed lubricant on the head is also smaller for the viscoelastic solution.

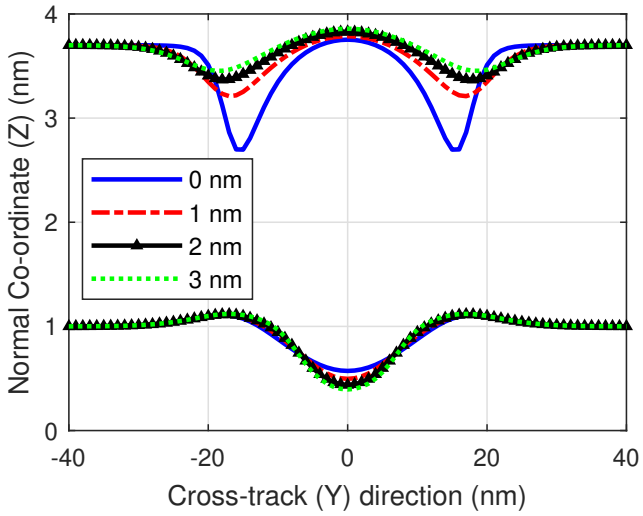

Figure 4.9: Disk and slider lubricant profiles in cross-track direction after 10 μs of laser irradiation for Ztetraol. Slip Length (b) varied from 0 to 3 nm. $T_{max,d}$ = 500 °C, $T_{max,s}$ = 300 °C, U = 10 m/s, FWHM = 20 nm.

Effect of Slip

Next, we investigate the impact of slip on the lubricant transfer process. We plot the cross-track lubricant profile on disk and slider after 10 μs of laser heating for Ztetraol in Figure 4.9. The slip length b is varied: 0, 1, 2 and 3 nm. All other parameters are kept fixed (same as the Ztetraol simulation from Section "Comparison between Zdol and Ztetraol Transfer"). As b is increased, the disk lubricant profile depth increases (i.e. larger viscous deformations, similar to Figure 3.8b from Chapter 3). The resultant smaller disk lubricant thickness near the laser spot center causes the evaporation rate from the disk to be smaller for larger b (due to larger disjoining pressure for thinner film), decreasing the amount of lubricant transfer. Accordingly, the slider lubricant height decreases as the slip length is increased.

Disjoining Pressure Study

Due to the close relation between disjoining pressure and evaporation rate, we study the effect of disjoining pressure on lubricant transfer. We consider three models - DP1: A_{VLS} = 1e-19 J, DP2: A_{VLS} = 3e-20 J, DP3: temperature dependent A_{VLS} from [33]. The same physics of molecular interactions and their changes with temperature applies to surface tension and interfacial energetics. Marchon & Saito [33] have proposed a temperature dependent

Hamaker constant defined as:

$$\begin{aligned} A_{VLS} &= \sqrt{A_{LL}A_{SS}} - A_{LL} \\ A_{LL} &= A^0_{LL}(1 - s\Delta T) \end{aligned} \tag{4.5}$$

Here A_{SS} and A_{LL} are Hamaker constants for solid-solid interactions and liquid-liquid interactions respectively. A_{LL} is assumed to have a linear dependence on temperature, similar to surface tension. We use the same values as those proposed by Marchon: A^0_{LL} = 3.78e-20 J, s = 1.72e-3 $^0C^{-1}$, A_{SS} = 1.16e-19 J. The resulting $A_{VLS}(T)$ varies from $\sim$ 3e-20 J at 0 °C to 0 at $\sim$ 600 °C [33]. The magnitude of disjoining pressure decreases in the order DP1 > DP2 > DP3. Figure 4.10 shows that the amount of lubricant accumulated on the head increases as the disjoining pressure decreases from DP1 to DP3.

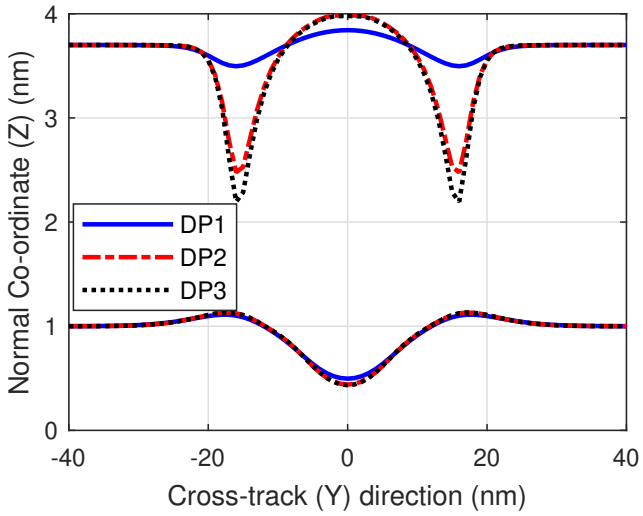

Figure 4.10: Disk and slider lubricant profiles in cross-track direction after 3 μs of laser irradiation for Ztetraol for different disjoining pressure models - DP1: A_{VLS} = 1e-19 J, DP2: A_{VLS} = 3e-20 J, DP3: temperature dependent A_{VLS} from [33]. $T_{max,d}$ = 500 °C, $T_{max,s}$ = 300 °C, U = 10 m/s, FWHM = 20 nm, b = 1 nm.

Effect of Media Temperature

In this section, we investigate how lubricant transfer changes with maximum disk temperature, a consequence of varying the laser power. The maximum head temperature is kept constant at 300 °C and the maximum disk temperature is varied: 500 °C, 550 °C and 600 °C. All other parameters are kept fixed. Figure 4.11 shows the cross-track profiles of the disk and head lubricant thicknesses for the different disk temperatures after 5 μs of laser heating for Ztetraol. As the disk temperature increases, the evaporation rate increases, causing the

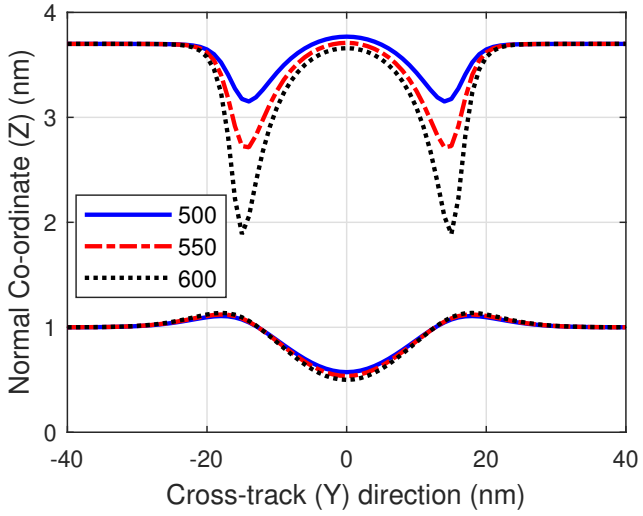

Figure 4.11: Disk and slider lubricant profiles in cross-track direction after 5 μs of laser heating for Ztetraol 2700. $T_{max,d}$ varied: 500°C, 550 °C, 600 °C. $T_{max,s}$ = 300 °C, U = 10 m/s, FWHM = 20 nm, b = 0

lubricant accumulation on the head to rise. To quantify the increase in lubricant transfer, we record the change in total volume of accumulated lubricant on the slider after 5 μs of laser heating. As the disk temperature is increased - 500 °C, 550 °C and 600 °C, the volume of lubricant accumulated on the slider increases significantly - 356 nm^3, 626 nm^3 and 1010 nm^3 respectively. A similar trend (larger lubricant transfer for higher disk temperature) is expected for Zdol as well (see Figure 2.7 from Chapter 2).

Effect of Head Temperature

Next, the maximum disk temperature is kept constant at 500 °C and the maximum slider temperature is varied: 200 °C, 300 °C, 400 °C. All other parameters are kept fixed. The resultant cross-track profiles of the disk and head lubricant thicknesses after 5 μs of laser heating for Ztetraol are plotted in Figure 4.12. We find that change in maximum slider temperature has a relatively small effect on the total amount of lubricant transfer (compared to effect of media temperature). As the head temperature is increased - 200 °C, 300 °C and 400 °C, the volume of lubricant accumulated on the slider decreased only slightly - 369 nm^3, 356 nm^3 and 345 nm^3 respectively. We do however see a difference in distribution of the accumulated lubricant on the slider in Figure 4.12. As the head temperature is increased, the thermo-capillary stress on the accumulated lubricant increases, causing the lubricant to be pushed further away from the NFT center, thereby forming a lump around the NFT. A similar trend (slight decrease in lubricant transfer for higher slider temperature) is expected for Zdol as well (see Figure 2.8 from Chapter 2).

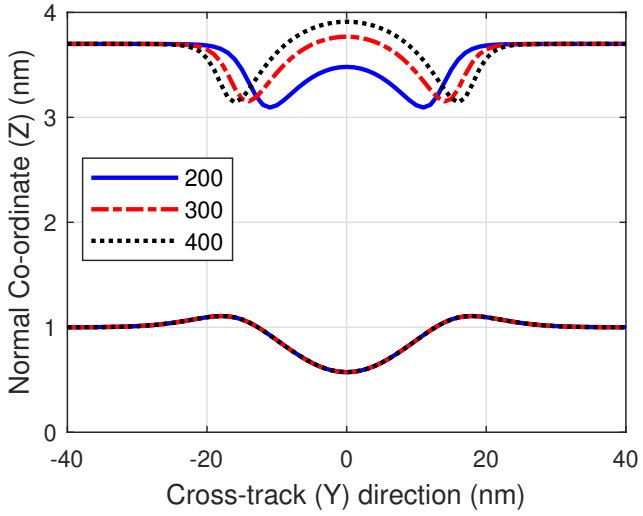

Figure 4.12: Disk and slider lubricant profiles in cross-track direction after 5 μs of laser heating for Ztetraol 2700. $T_{max,s}$ varied: 200°C, 300 °C, 400 °C. $T_{max,d}$ = 500 °C, U = 10 m/s, FWHM = 20 nm, b = 0

Effect of Initial Lubricant Thickness

Here we study how the lubricant transfer process changes with the initial disk lubricant thickness. Figure 4.13 shows the cross-track profiles of the disk and head lubricant thicknesses after 5 μs of laser heating for three different initial disk lube thicknesses: 0.8, 1 and 1.2 nm for Ztetraol. All other parameters are kept fixed. As the disk lubricant thickness is decreased, the lubricant disjoining pressure increases (Eq. (3.13) from Chapter 3). The resultant larger disjoining pressure leads to more suppression of the disk evaporation rate (Eq. (4.2)), causing the amount of lubricant transfer to decrease. Accordingly, as the initial disk lubricant thickness is decreased: 1.2 nm, 1 nm, 0.8 nm, the volume of lubricant accumulated on the slider also decreases - 510 nm^3, 356 nm^3 and 193 nm^3 respectively. A similar trend (larger lubricant transfer for thicker disk lube) is expected for Zdol as well (see Figure 2.9 from Chapter 2).

Effect of Laser Spot Size

In this section, we study the effect of laser FWHM on the lubricant transfer process. We plot the disk and slider lubricant profiles in the cross-track direction (normalized by FWHM) for Ztetraol and Zdol for two laser spot sizes: 20 nm and 1 μm in Figures 4.14 and 4.15 respectively. All other parameters are kept fixed. The relative importance of thermo-capillary stress vs evaporation for lubricant deformation during HAMR depends on its vaporization properties, laser spot size and peak temperature.

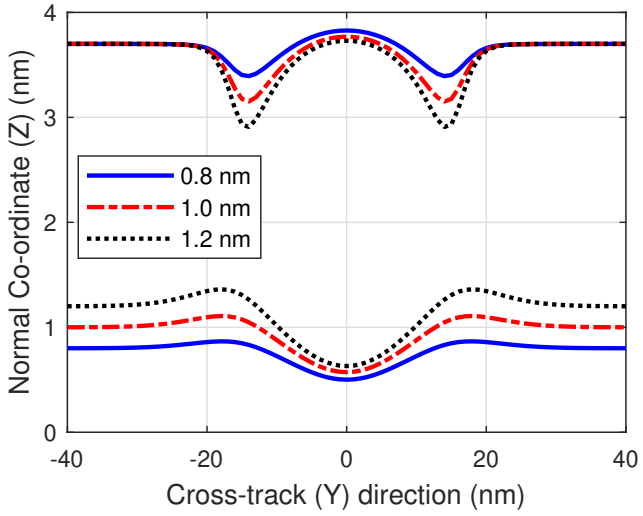

Figure 4.13: Disk and slider lubricant profiles in cross-track direction after 5 μs of laser heating for Ztetraol 2700. $h_{0,d}$ varied: 0.8 nm, 1 nm, 1.2 nm. $T_{max,d} = 500$ °C, $T_{max,s} = 300$ °C, $U = 10$ m/s, FWHM = 20 nm, b = 0 nm

In Figure 4.4 from section "Evaporation versus Thermo-capillary Stress", we saw that thermocapillary stress dominates at low spot sizes ($\sim$ 20 nm) and evaporation dominates at higher spot sizes ($\sim$ 1 μm) for Ztetraol at $\sim$ 500 °C. Hence, as the laser spot size is increased from 20 nm to 1 μm, the amount of lubricant transfer also increases (Figure 4.14). On the other hand, the large vapor pressure of Zdol at $\sim$ 500 °C results in evaporation being the dominant mechanism (over thermocapillary stress) for all spot sizes ($\sim$ 20 nm to 1 μm) (see Figure 4.3 from section "Evaporation versus Thermo-capillary Stress"). The evaporation rate for Zdol at $\sim$ 500 °C and 20 nm is already so high that increase in laser spot size from 20 nm to 1 μm is not very effective in further increasing the evaporation rate (Figure 4.15). This is because the lubricant is so thin that the disjoining pressure is extremely large (Eq. (3.13) from Chapter 3) and is very effective at suppressing evaporation (Eq. (4.2)).

In order to compare the amount of transfer for different spot sizes, we normalize the volume of lubricant accumulated on the slider (ΔV_{slider}) by the laser FWHM squared: $\overline{\Delta V}_{slider} \equiv \frac{\Delta V_{slider}}{FWHM^2}$ [32]. The resulting length scale $\overline{\Delta V}_{slider}$ for Ztetraol is found to increase from 0.09 nm to 0.25 nm as the spot size is increased from 20 nm to 1 μm. On the other hand, $\overline{\Delta V}_{slider}$ for Zdol is found to decrease from 0.4 nm and 0.27 nm as the spot size is increased from 20 nm to 1 μm. This trend of decrease in $\overline{\Delta V}_{slider}$ on increase in FWHM was also observed in our previous viscous simulations for Zdol (see Figure 2.12 from Chapter 2).

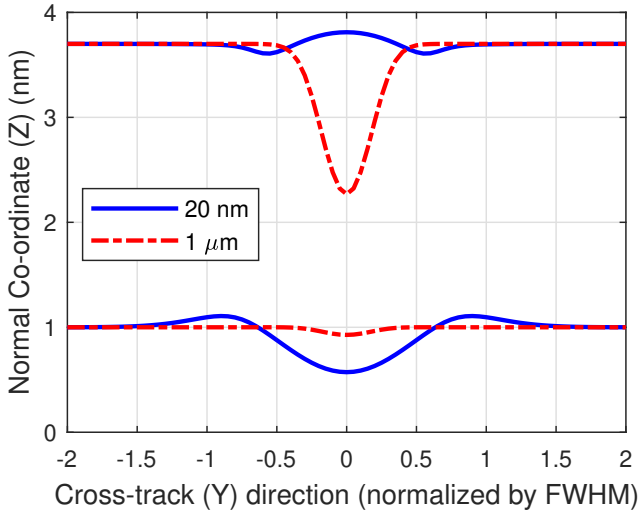

Figure 4.14: Disk and slider lubricant profiles in cross-track direction after 0.5 μs of laser heating for Ztetraol 2700 for laser FWHM of 20 nm and 1 μm. $T_{max,d}$ = 500 °C, $T_{max,s}$ = 300 °C, U = 10 m/s, b = 0

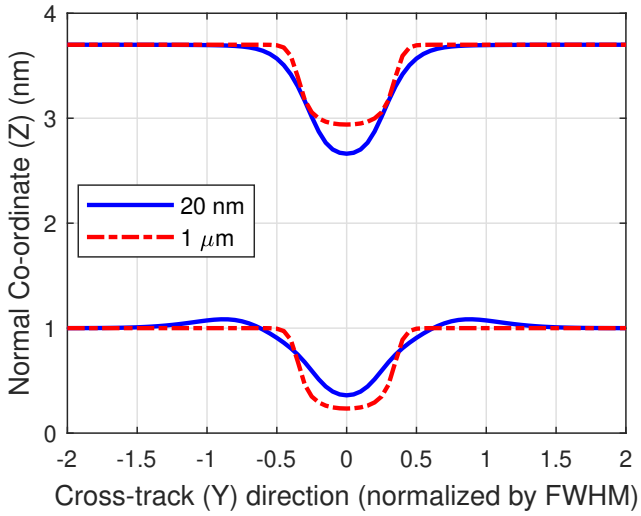

Figure 4.15: Disk and slider lubricant profiles in cross-track direction after 6 ns of laser heating for Zdol 2000 for laser FWHM of 20 nm and 1 μm. $T_{max,d}$ = 500 °C, $T_{max,s}$ = 300 °C, U = 10 m/s, b = 0 nm

Lubricant Transfer vs Write-induced Contamination

Media-to-head lubricant transfer is one of the possible mechanisms for write-induced smear on HAMR heads [29]. This contamination has been observed to occur over a timescale of

seconds [29]. Contaminants are expected to be a small volumetric percentage of the media lubricant. Hence, contaminants would account for a small fraction of the lube accumulated on the head. This explains why write-induced contamination has been observed to occur on a timescale of seconds [29], even though we predict lubricant transfer to occur on a timescale of μs for Ztetraol.

4.4 Results: Lubricant Recovery after Laser Removal

We next study the recovery of the lubricant after the laser is turned off. The lubricant is subjected to a moving laser spot at 10 m/s for 10 ns. The laser is then turned off and the temperature drop is modeled as a 2 ns ramp (T_{max} = 500 °C at t = 10 ns and T_{max} = 25 °C at t = 12 ns). The slip length b is 1 nm. The blue curve in Figure 4.16a is the down-track lubricant profile for Ztetraol after 10 ns of laser heating. We see a viscous trail and an elastic trough. As the disk temperature falls to ambient at t = 12 ns, the elastic trough recovers instantaneously (time scale of ns) leaving behind only the viscous trail (Red curve in Figure 4.16a). Thereafter, the viscous trail recovers slowly under the influence of disjoining pressure over a time scale of μs, as predicted in viscous simulations [34]. A similar trend - instantaneous recovery of elastic trough from 10 ns to 12 ns, followed by slow recovery of viscous/evaporation trail is observed for Zdol in Figure 4.16b.

In order to compare the recovery of Zdol and Ztetraol, we plot the minimum lubricant height versus time for both lubricants in Figure 4.17. The viscosity of Ztetraol at 25 °C is ~7 times that of Zdol [6]. Hence, the recovery rate (slope of Figure 4.17) of Zdol during the second stage (recovery of the viscous/evaporation trail) is larger than that of Ztetraol.

4.5 Discussion

Our simulations indicate that PFPE lubricants exhibit a combination of viscous and elastic behavior at the timescale of HAMR. When subjected to a scanning laser spot of 20 nm FWHM at 10 m/s, the disk lubricant profile consists of an elastic trough centered at the instantaneous laser location, followed by a viscous trail (Figure 3.4 from Chapter 3). The viscous vs elastic behavior of the lubricant is a function of the Deborah number, De = $\frac{\lambda U}{L}$. At a laser spot size (L) of 1 μm (low De), the lubricant exhibits purely viscous behavior (Figure 4.4b). However, as L is reduced to 20 nm, the Deborah number decreases, causing the lubricant to behave part-viscous, part-elastic (Figures 3.5a, 4.4a).

The relative importance of thermo-capillary stress vs evaporation for lubricant deformation during HAMR depends on its vaporization properties, laser spot size and peak temperature. Thermo-capillary stress is proportional to the spatial temperature gradient and increases as the spot size is decreased or the peak temperature is increased. Evaporation rate also increases on increase in peak temperature. At low temperatures (~ 350 °C), thermo-capillary stress dominates at small spot sizes (~ 20 nm) and evaporation dominates at large

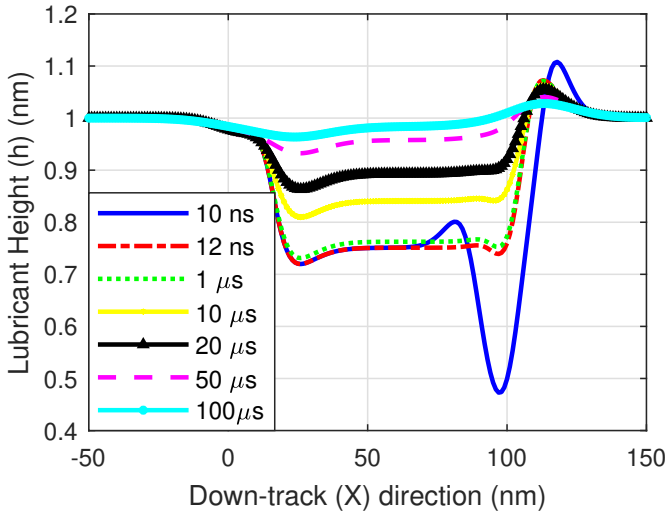

(a) Ztetraol 2700 Recovery

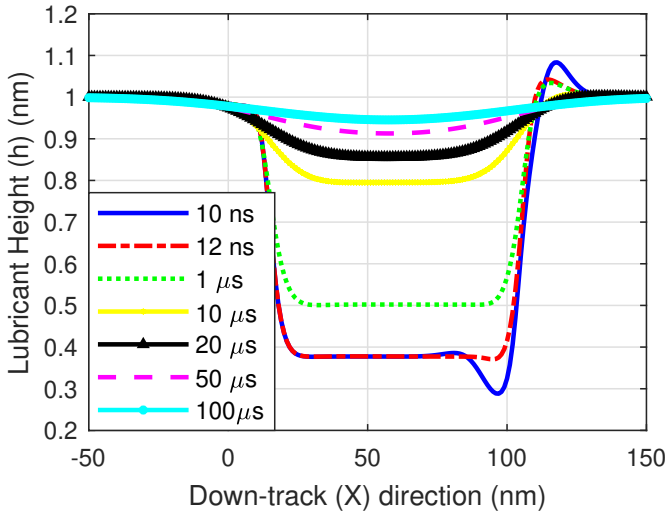

(b) Zdol 2000 Recovery

Figure 4.16: Lubricant recovery after 10 ns of writing. T_{max} = 500 °C, U = 10 m/s, FWHM = 20 nm, b = 1 nm.

spot sizes ($\sim$ 1 μm) for Zdol [32]. However, at high temperatures ($\sim$ 500 °C), evaporation dominates at all spot sizes - 20 nm to 1 μm (Figures 4.3a & 4.3b). On the other hand, for Ztetraol, thermo-capillary shear stress dominates over evaporation for smaller spot sizes ($\sim$ 20 nm), even at high temperatures $\sim$ 500 °C (Figure 4.4a). However, evaporation dominates for larger spot sizes ($\sim$ 1 μm in Figure 4.4b). The disparity between the dominant mechanism for Zdol vs Ztetraol at 500 °C, 20 nm (evaporation and thermo-capillary stress respectively)

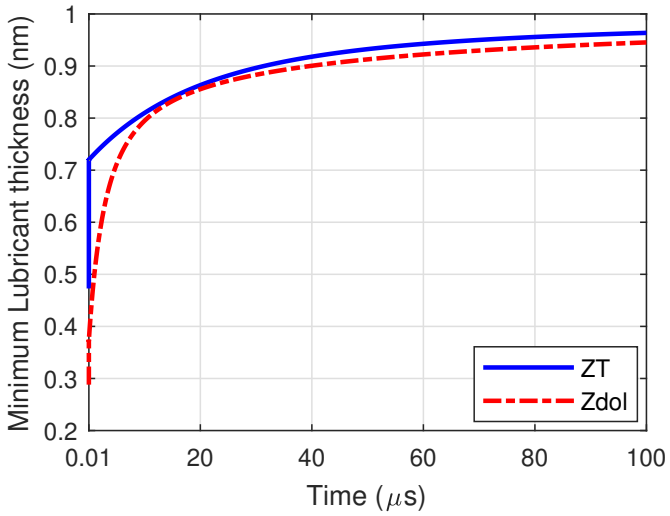

Figure 4.17: Lubricant recovery: Zdol 2000 vs Ztetraol 2700.

is due to the difference in their vaporization properties (Figure 4.2). This also leads to a significant difference in the rates of media-to-head lubricant transfer for Zdol (timescale of ns - Figure 4.5a) vs Ztetraol (timescale of μs - Figure 4.6a).

The media-to-head lubricant transfer causes a deposition of media contaminants at the NFT. A quantitative understanding of this material transfer is necessary to mitigate its effect. The predicted disk lubricant deformation using a purely viscous model is smaller than the deformation due to a viscoelastic constitutive equation (Figure 4.8). This difference causes the viscous model to over-predict the amount of transfer, compared to the viscoelastic model. Including viscoelastic effects is thus essential to accurately estimate the rate of lubricant transfer.

Disjoining pressure suppresses the evaporation rate of the thin-film lubricant (Eqs. (4.1), (4.2)). Hence, the amount of lubricant transfer increases as the Hamaker constant is decreased (Figure 4.10). Slip increases the flow rate of the disk lubricant, causing larger deformations. Accordingly, as the slip length is increased, the disk lubricant thickness near the laser spot center decreases, restricting the amount of transfer (due to larger disjoining pressure for the thinner film, Figure 4.9).

The amount of transfer increases on increase in media temperature (Figure 4.11) and initial lubricant thickness (Figure 4.13). Comparatively, the head temperature has a small impact on the transfer dynamics (Figure 4.12).

The recovery of the viscoelastic lubricant post-writing has two time scales. When the laser is turned off, the elastic trough recovers instantaneously ($\sim$ ns), leaving behind the viscous/evaporation trail (Figures 4.16a & 4.16b). Thereafter, the trail recovers over a time scale of μs. The recovery of the viscous/evaporation trail depends on the lubricant disjoining

pressure, viscosity and the initial deformed profile [34]. The viscous recovery rate for Zdol is faster than that for Ztetraol, primarily due to the higher viscosity of Ztetraol at 25 °C. (Figure 4.17)

In this study, we have not considered the effects of thermal decomposition [80] or polydisperity [81]. The reduction of effective viscosity at high shear stresses is presumed to be due to slip by Mate et al. [86]. However, at high shear strains, viscosity reduction could also occur due to shear thinning [89, 103]. We have assumed that no shear thinning occurs in this study. At low fly heights, environmental conditions such as humidity also influence the interactions in the head-disk interface. Kim et al. found that disk-to-head lubricant transfer is proportional to AH, absolute amount of water in the system, rather than RH, Relative Humidity of the system alone [104]. The effect of humidity is not considered in this study.

4.6 Conclusion

In this study, we have used a modified Reynolds lubrication equation that employs the Linear Maxwell constitutive model to describe the evolution of the viscoelastic lubricant during HAMR. We have used this equation to predict the media-to-head lubricant transfer during HAMR writing. This model simultaneously determines the thermo-capillary stress driven deformation and evaporation of the viscoelastic lubricant film on the disk, the diffusion of the vapor phase lubricant in the air bearing and the evolution of the condensed lubricant film on the slider.

When subjected to a 20 nm FWHM scanning laser spot, the lubricant profile consists of an elastic trough centered at the instantaneous laser location, followed by a viscous trail. When the laser is turned off, the elastic trough recovers instantaneously, leaving behind the viscous trail, which recovers over a time scale of μs.

We have investigated the effects of viscoelasticity, lubricant type (Zdol vs Ztetraol), molecular weight, slip velocity, disjoining pressure, head/media temperature, initial disk lubricant thickness and laser FWHM on the lubricant transfer process. Our results show a significant difference between the rates of transfer for Zdol ($\sim$ ns) vs Ztetraol ($\sim$ μs). As the lubricant molecular weight is decreased, the evaporation rate and amount of transfer increase. The predicted disk lubricant deformation using a purely viscous model is smaller than the deformation due to a viscoelastic model, causing the viscous model to over-predict the amount of transfer. The amount of transfer decreases on increase in slip length and increase in disjoining pressure. The amount of transfer increases on increase in media temperature and increase in initial disk lubricant thickness. Comparatively, the head temperature has a small effect on the transfer dynamics. Ztetraol shows larger disk-to-head lubricant transfer for larger spot sizes (on a relative scale). However, Zdol shows smaller transfer for larger spot sizes (on a relative scale).

This chapter presents work published in Tribology Letters (reprinted by permission from Springer Nature (Tribology Letters) [97], Copyright (2018)) and IEEE Transactions on Magnetics (© 2018 IEEE. Reprinted, with permission, from [98]).

Chapter 5

Investigation of Nanoscale Heat Transfer Between a Head and Non-rotating Disk

5.1 Introduction

Head overheating is a major reliability issue curtailing the commercialization of both HAMR and MAMR. During HAMR writing, a complex laser delivery system integrated into the head is used to create a local hot spot on the disk, generating high temperatures on the disk (∼500 °C) and the head (∼300 °C) [29]. The high current density in the Spin Torque Oscillator in MAMR heads (∼10^8 A/cm^2) also causes high head temperatures (>200 °C) [39].

Moreover, with the minimum fly height of less than 5 nm in contemporary HDDs, classical heat transfer theory can no longer be used to predict temperatures in the head and the disk. Previous experimental studies [20, 21] and wave-based theories of radiation and phonon conduction (or tunneling) [22–25, 105, 106] have shown that heat flux increases significantly at nanoscale gaps. Several other theoretical studies also predict high heat flux between two surfaces separated by a small gap [107–110]. There is a need to develop a methodology that uses theoretical curves for spacing-dependent nanoscale heat transfer coefficients to predict head/media temperatures in actual HDDs.

Ma et al. developed a setup (static touchdown experiment) to study heat flux across a gap between two stationary bodies as the spacing between them closes in a controlled manner from tens of nm to contact [111]. In this experiment, the crown feature (∼ 7 nm) of the head Air Bearing Surface (ABS) is used to control the initial spacing between the head and the media (non-rotating) [111, 112] (Figure 5.1). After loading the head onto the media, the initial spacing between the trailing edge body of the slider and the media can be adjusted via a rocking motion about the center caused by moving the media forward or backward. For instance, moving the media forwards (to the right in Figure 5.1) would cause the slider to rotate counterclockwise, increasing the spacing between the trailing edge body

of the slider and the media. With an initial spacing of 10-50 nm, the Thermal Fly Height Control (TFC) heater in the head is powered to generate a local thermal protrusion near the trailing edge, causing touchdown. A near-surface resistive temperature sensor (Embedded Contact Sensor or ECS) is used to measure the temperature change at the head surface due to the heat flux across the gap. The TFC Power is kept on for a long enough duration in the experiment to ensure that the measured ECS temperature has reached steady state. This entire setup is placed inside a chamber, which can reach high vacuum (< 1e-4 Torr).

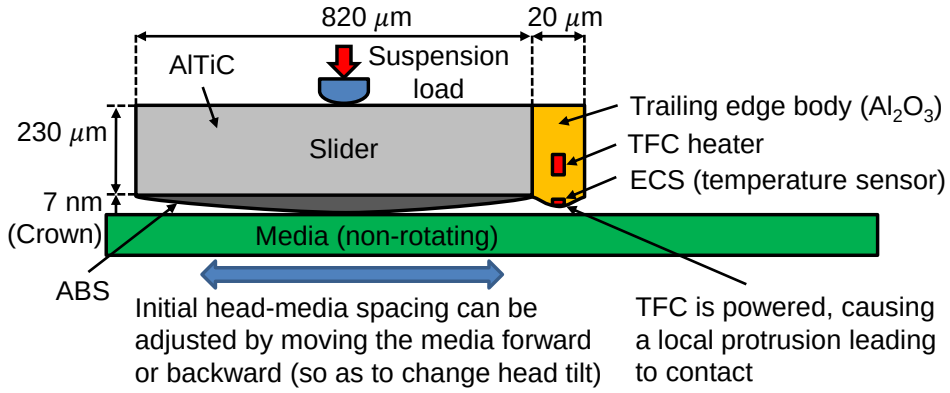

Figure 5.1: Static touchdown experiment schematic (side view)

Several studies have demonstrated that the ECS is an effective tool in understanding heat transfer in the HDI [113–116]. Using the static touchdown experiment, Ma et al. observed that enhanced heat transfer at the HDI causes a drop in the ECS temperature as the ECS approaches the media [111]. They also observed a hysteresis loop during load-unload experiments, suggesting that van der Waals (vdW) forces play an important role on HDI heat transfer [111]. Subsequently, Ma et al. performed phonon conduction-based simulation of ECS cooling during static touchdown, however, their model shows qualitative, but not good quantitative agreement with experiments [112, 117]. Moreover, vdW forces were not considered while determining the thermal protrusion of the head in these numerical studies.

In this study, we present a numerical model to simulate the head temperature profile during static touchdown and compare our results with experiments performed with a head on different media (Si wafer, magnetic disks with AlMg/glass substrate). We first discuss the heat transfer coefficient between two half-spaces based on a wave-based phonon conduction theory as a function of the spacing, the temperatures and material properties of both half-spaces. Next, the numerical model that uses this heat transfer coefficient to simulate head temperature is presented. Simulated ECS temperature during static touchdown with different initial ECS-media spacings, in different environments (air vs vacuum) and on the three different media are compared with corresponding experiments. This is followed by a discussion and conclusion.

This work was completed jointly with Qilong Cheng, Amin Ghafari and Yuan Ma. Qilong and Yuan performed the static touchdown experiments. Amin developed the model to compute the phonon conduction heat transfer coefficient. I developed the numerical model and performed simulations to predict the head temperature, disk temperature and head-disk spacing during static touchdown using the air and phonon conduction heat transfer coefficients.

5.2 Model Description

Heat Transfer Coefficient in the HDI

During static touchdown of the head on the disk, three major heat transfer schemes exist: air conduction (htc_{air}), phonon conduction (htc_{phon}) and radiation (htc_{rad}). The heat transfer coefficient for conduction through air (htc_{air}) is a function of the air bearing height $h = (d-t)$, pressure p_{air} and temperature $T_{air} = \frac{(T_s+T_d)}{2}$ and can be obtained by solving the energy equation using temperature jump theory [18, 19].

$$htc_{air} = \frac{k_{air}}{h + 2\frac{2-\sigma_T}{\sigma_T}\frac{2\gamma}{\gamma+1}\frac{1}{Pr}\lambda_{air}} \tag{5.1}$$

Here $\lambda_{air}(h, p_{air}, T_{air})$ is the effective mean free path of air molecules at pressure p_{air} and temperature T_{air} accounting for boundary scattering[19]. k_{air} is the effective thermal conductivity of air accounting for boundary scattering. σ_T is the thermal accommodation coefficient, Pr is the Prandtl number of air and γ is the ratio of specific heats for air.

Intermolecular vdW forces between two half-spaces ($\nu = A, B$) with temperatures T_A, T_B and spacing h cause phonons to transfer energy from one half-space to the other (phonon conduction)[23, 25, 105]. When the system of the two half-spaces is in equilibrium (no heat flux), phonon waves in both half-spaces are described by the Bose-Einstein distribution (or the Planck function), which is a function of the equilibrium temperature ($T_A = T_B = T$) and frequency ω[106].

$$p^2(\omega, T)|_{equil} = \left(\exp\left(\frac{\hbar\omega}{k_B T}\right) - 1\right)^{-1} \tag{5.2}$$

Here $\hbar$ and k_B are the reduced Planck constant and the Boltzmann constant respectively.

When the system of the two half-spaces is in a non-equilibrium condition (non-zero steady state heat flux Q), the distribution function of phonons in each half-space ν is a modified version of Bose-Einstein distribution (modified Planck function)[106] and is given by

$$(p_\nu^{\pm})^2(\omega, T_\nu, \mu_\nu) = \left(\exp\left(\frac{\hbar\omega[1 \mp \mu_\nu]}{k_B T_\nu}\right) - 1\right)^{-1} \tag{5.3}$$

Here μ_ν is an unknown factor in $(0,1)$ indicating how much the system has deviated from equilibrium, with $\mu_\nu = 0$ as being at the equilibrium condition. In our notation, p_ν^+ applies to waves travelling away from the half-space and p_ν^- applies to waves travelling into the half-space. $(p_\nu^\pm)^2$ is displaced from the equilibrium distribution, $p^2(\omega,T)|_{equil}$, by a term $\hbar\mu_\nu\omega$, which can be interpreted physically as the chemical potential[118]. The displacement term, $\hbar\mu_\nu\omega$ is proportional to the phonon momentum and goes to zero as $\omega \to 0$. We note that since $0 < \mu_\nu < 1$, $(p_\nu^\pm)^2$ is always positive.

As demonstrated in Refs. [25, 105], the resultant heat flux $Q(T_A, T_B, h)$ between the two half-spaces is given by two different representations [25, 105]

$$\begin{aligned} Q &= N \int_\Omega \left\{ (p_\nu^+)^2 - (p_\nu^-)^2 \right\} \frac{\hbar\omega^3}{8\pi^2 c_\nu^2} \sin(2\theta_\nu) d\theta_\nu d\omega, \\ \nu &= A, B, \end{aligned} \tag{5.4}$$

where $N = 3$ is the number of polarizations, ω, θ_ν are the wave frequency and angle of propagation, ρ_ν, c_ν are the material density and wave speed. The domain of integration $\Omega = \Omega(\omega, \theta_\nu)$ determines the wave vectors that contribute to Q and is determined using the compatibility conditions in Ref. [25] which are summarized below.

$$\Omega(\omega,\theta_\nu) = \begin{cases} F_-(\mu_A, T_A, \omega, \theta_A) \le f(\mu_B, T_B, \omega, \theta_B) \\ \le F_+(\mu_A, T_A, \omega, \theta_A), \\ F_-(-\mu_B, T_B, \omega, \theta_B) \le f(-\mu_A, T_A, \omega, \theta_A) \\ \le F_+(-\mu_B, T_B, \omega, \theta_B), \\ 0 \le \omega \le \omega_D, \quad 0 \le \theta_\nu \le \Theta_\nu. \end{cases} \tag{5.5}$$

Here $F_\pm$ and f are

$$\begin{aligned} F_\pm(\mu_\nu, T_\nu, \omega, \theta_\nu) &= |p_\nu^-(\omega, T_\nu, \mu_\nu) \pm R p_\nu^+(\omega, T_\nu, \mu_\nu)|, \\ f(\mu_\nu, T_\nu, \omega, \theta_\nu) &= \sqrt{1-R^2}\, p_\nu^-(\omega, T_\nu, \mu_\nu) \\ R &\equiv R(\omega, \theta_\nu, h) \end{aligned} \tag{5.6}$$

where R is the reflection coefficient, ω_D is the Debye frequency of half-space ν and Θ_ν is the critical angle for half-space ν (depends on c_ν) [23, 25].

The effect of vdW forces on Q is considered through the reflection coefficient, R. When phonons are considered as propagating waves inside a medium, the energy transfer between layers is quantified according to the reflection coefficient of waves on the interface. For the energy transfer between two layers separated by vacuum, R depends on the vdW forces between the two layers. R affects the domain of integration, Ω, in Eq. (5.4) through Eqs. (5.5), (5.6) and thus determines how much energy can be transferred between the two half-spaces due to vdW forces[25]. A detailed derivation for the expression of $R(\omega, \theta_\nu, h)$ (depends on material properties ρ_ν, c_ν) using vdW forces can be found in Ref. [23].

Table 5.1: Phonon conduction parameters for three different media

Material	c_1	c_2	c_3	b
Si	-1.93	-0.83	1.4	12.33
Al-Mg	-1.97	-0.86	1.65	11.34
Glass	-2.11	-0.89	0.5	10.10

We have two equations from (5.4) and 3 unknowns (μ_A, μ_B, Q), resulting in a range of possible solutions for Q. By using the Maximum Entropy Production Principle (MEPP) [119], we choose the maximum Q as the solution in order to maximize the entropy of the system [25].

Using this methodology, the phonon conduction heat transfer coefficient ($htc_{phon} = \frac{Q(T_s,T_d,h)}{T_s-T_d}$) is determined as a function of the disk temperature T_d, the slider-disk temperature difference $\Delta T = T_s - T_d$ and the spacing h. We plot htc_{phon} as a function of h, ΔT and T_d for the Al_2O_3 - Si wafer interface in Figure 5.2. We observe that htc_{phon} varies almost linearly with h, ΔT and T_d on a log-log scale. Further, we plot htc_{phon} vs h for three media materials: Si, AlMg, glass in Figure 5.3. The slider material is assumed to be Al_2O_3 for all three cases. Our results suggest that htc_{phon} can be approximated using the following equation (0.1 nm $\leq h \leq$ 100 nm, 4 K $\leq \Delta T \leq$ 400 K, 298 K $\leq T_d \leq$ 398 K)

$$ln(htc_{phon}) = c_1 ln(h) + c_2 ln\left(\frac{\Delta T}{400}\right) + c_3 ln\left(\frac{T_d}{298}\right) + b \tag{5.7}$$

Parameters c_1, c_2, c_3, b depend on the density (ρ_ν), wave speed (c_ν) and Debye frequency of both half-spaces (Table 5.1).

At nanoscale spacings, the heat transfer coefficient due to radiation ($\sim 10^3$ W/m^2·K) [24] is much smaller than that due to phonon conduction ($\sim 10^6$ W/m^2·K), hence radiation is ignored in this study. Thus, the net heat transfer coefficient in the HDI is approximated as:

$$htc_{total} \approx htc_{air} + htc_{phon} \tag{5.8}$$

As $h \to 0$, the net heat transfer coefficient due to phonon and air conduction, htc_{total} increases (Eq. (5.7)). In reality, htc_{total} would be limited by the interface thermal conductance when the head and the media come into contact [120]. Hence, we limit htc_{total} to a constant interface thermal conductance: 5e7 W/m^2·K for head-Si interface and 3e7 W/m^2·K for head-AlMg disk, head-glass disk interfaces.

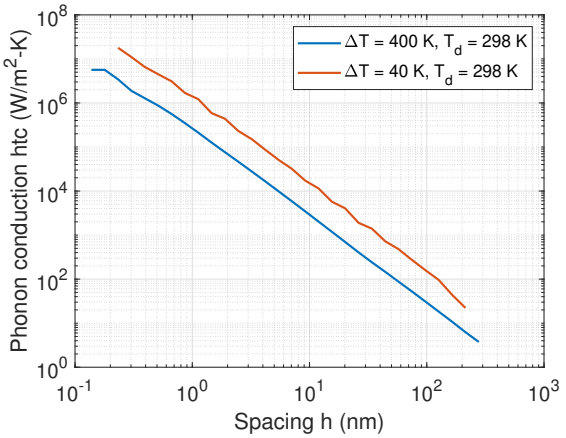

(a) htc_{phon} vs h

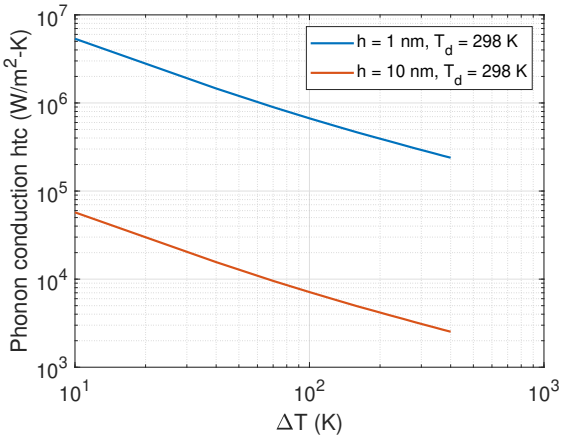

(b) htc_{phon} vs ΔT

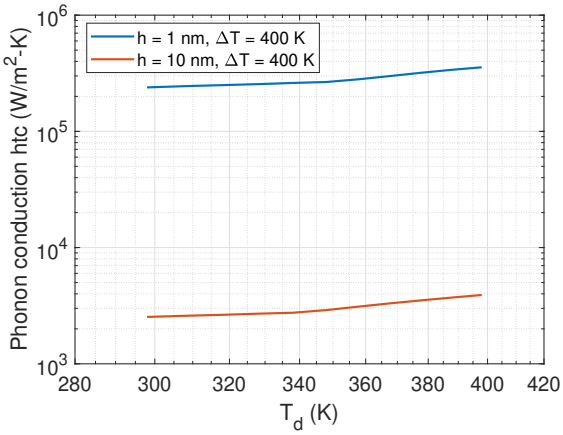

(c) htc_{phon} vs T_d

Figure 5.2: Phonon conduction heat transfer coefficient, htc_{phon} vs h, ΔT, T_d for Al_2O_3 - Si wafer interface

Thermo-mechanical Slider and Disk model

The net heat transfer coefficient due to phonon and air conduction, $htc_{total}(T_s, T_d, h)$ is integrated into a finite element ANSYS model of the slider and the disk. The bulk of the slider block (820 μm x 700 μm x 230 μm) is made of AlTiC (k = 20 W/m·K)[10], while the trailing edge (TE) portion (20 μm x 700 μm x 230 μm) is made of Al_2O_3 (k = 1.8 W/m·K)[10] (Figure 5.1). Additionally, the TE body has several metal components (such as the reader, writer and shields), which are much better thermal conductors than Al_2O_3 and affect the heat diffusion inside the head. The focus of this study is to understand the heat transfer in the HDI and model its effect on the ECS temperature. To avoid an overly complex geometric model, we define an effective thermal conductivity (k_{eff}) and effective

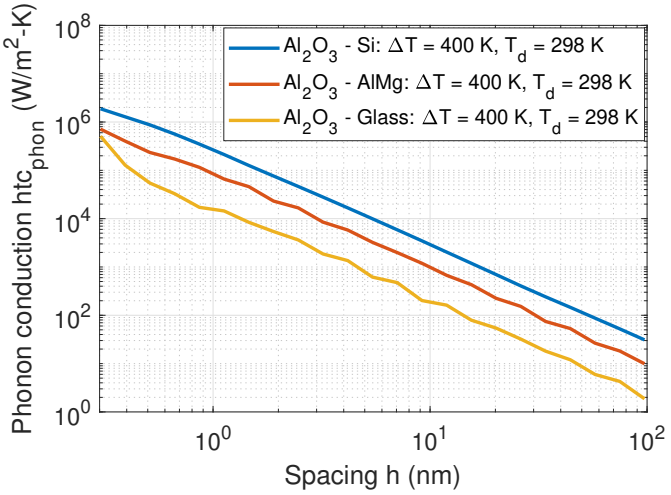

Figure 5.3: Phonon conduction heat transfer coefficient, htc_{phon} vs spacing, h at T_d = 298 K and ΔT = 400 K for three different media

thermal expansion coefficient (α_{eff}) for the part of the TE body near the ABS that contains these metal elements (20 μm x 40 μm x 30 μm). Using the values k_{eff} = 50 W/m·K and α_{eff} = 7e-6 K^{-1}, the initial slope of the ECS temperature vs TFC Power curve during the static touchdown simulation on Si wafer in air (0.85 °C/mW) agrees with the measured slope during the experiment (Figure 5.4). We note that the value of k_{eff} is dependent on the head design and lies within the range of thermal conductivity (W/m·K) of all the components in the head: 35 for NiFe (reader/shield), 403 for Cu (writer), 1.8 for Al_2O_3[10]. We create a local disk model (1150 μm x 800 μm x 330 μm) and enforce all boundary faces (except the face opposite to ABS) at room temperature (25 °C).

The slider temperature profile (T_s) during the static touchdown simulation is determined using a steady state thermal conduction simulation with a heat source (TFC), metal suspension cooling (2000 W/m^2·K)[74] on the back surface and $htc_{total}(T_s, T_d, h)$ on the ABS. The disk temperature profile (T_d) is determined using a steady state thermal conduction simulation with the same $htc_{total}(T_s, T_d, h)$ on the surface opposite to the ABS. The head-disk spacing (h) is determined using a linear elasto-static simulation with specified temperature profile (T_s) and vdW force on the ABS to evaluate the head's TFC heating-induced protrusion. The net vdW force between each ABS element (Δ) and the disk is given by [121]

$$F_{vdW} = \frac{A}{6\pi} \iint_{\Delta} \frac{dxdy}{h^3} - \frac{B}{45\pi} \iint_{\Delta} \frac{dxdy}{h^9} \tag{5.9}$$

We assume that A = 0.4e-19 J, B = 1e-76 Jm^6. The resultant non-linear problem for T_s, T_d and h (or equivalently htc_{total}) is solved using Broyden's (Quasi-Newton) method [122].

We note that our model considers the effect of vdW forces in two different ways. Firstly, the effect of vdW forces is considered on the phonon conduction heat flux Q in Eq. (5.4) through the reflection coefficient (using Eqs. (5.5), (5.6)). Secondly, we also consider the effect of vdW forces while determining the thermal protrusion of the slider through Eq. (5.9).

5.3 Results and Discussion

Free Heating

Figure 5.4 shows the ECS temperature vs TFC power during free heating of the slider in air (with no media present). During free heating, there is negligible cooling on the ABS and the metal suspension back cooling is poor compared to static touchdown, since the suspension is not loaded. With a low back cooling coefficient for free heating (1200 W/m^2·K vs 2000 W/m^2·K for static touchdown [74]), the simulated free heating ECS temperature curve agrees with the experiment.

Effect of van der Waals forces

Figure 5.4 also plots the simulated ECS temperature vs TFC power for static touchdown of the head on Si in air with an initial ECS-media spacing of 21.3 nm. We consider two cases: (a) vdW forces are not considered while determining the thermal protrusion of the slider (solid green curve in Figure 5.4), (b) vdW forces are considered while determining the slider's thermal protrusion using Eq. (5.9) (solid red curve). Both simulation cases consider the effect of vdW forces on Q through the reflection coefficient in Eq. (5.4). We plot the minimum spacing h and the maximum heat transfer coefficient htc_{total} vs TFC power for the simulation case (b) (including vdW forces) in Figure 5.5.

As the TFC power is increased, the thermal protrusion of the TE portion of the slider also increases, causing the minimum spacing h to decrease (Figure 5.5). As the spacing h decreases with increasing TFC power, the maximum htc_{total} increases. In particular, when the h becomes smaller than about 2 nm, we see a rapid increment in htc_{total} in Figure 5.5 due to exponential growth in phonon conduction (Eq. (5.7)).

Figure 5.4 shows that as the TFC power is increased, initially, the ECS temperature increases due to larger joule heating at the higher TFC power for both cases (a) and (b). However, when the ECS-media spacing becomes smaller than about 2 nm, enhanced phonon conduction heat transfer causes a drop in the ECS temperature.

The simulation without vdW forces (solid green curve in Figure 5.4) shows a much more gradual drop in the ECS temperature than that in the experiment (dashed red curve). As the ECS approaches touchdown, enhanced phonon conduction causes cooling and impedes touchdown. On the other hand, attractive vdW forces between the slider and the media accelerate the touchdown process. Hence, the simulation with vdW forces (solid red curve)

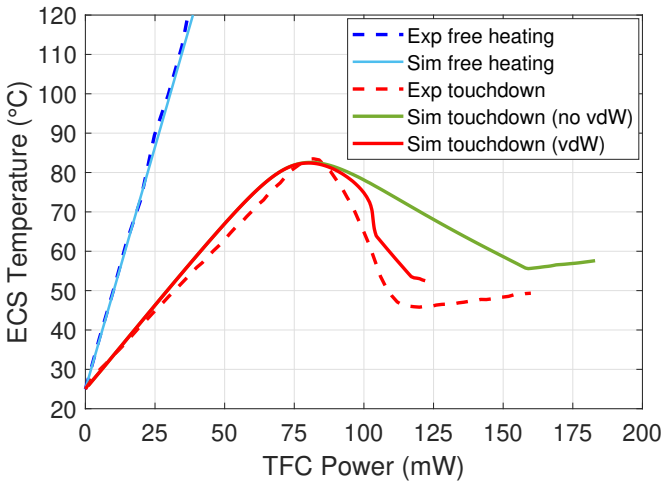

Figure 5.4: ECS temperature vs TFC power for static touchdown experiment and simulation on Si in air with initial spacing of 21.3 nm. Solid green curve excludes vdW forces while computing slider's thermal protrusion, while solid red curve considers vdW forces while computing slider's thermal protrusion.

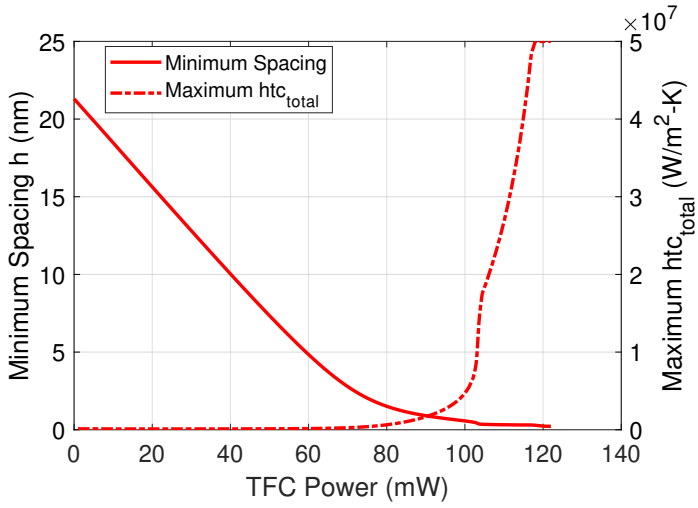

Figure 5.5: Static touchdown simulation on Si in air with initial spacing of 21.3 nm, including the effect of vdW forces. Solid red curve curve shows the minimum spacing h (left axis) and dashed red curve shows the maximum htc_{total} (right axis).

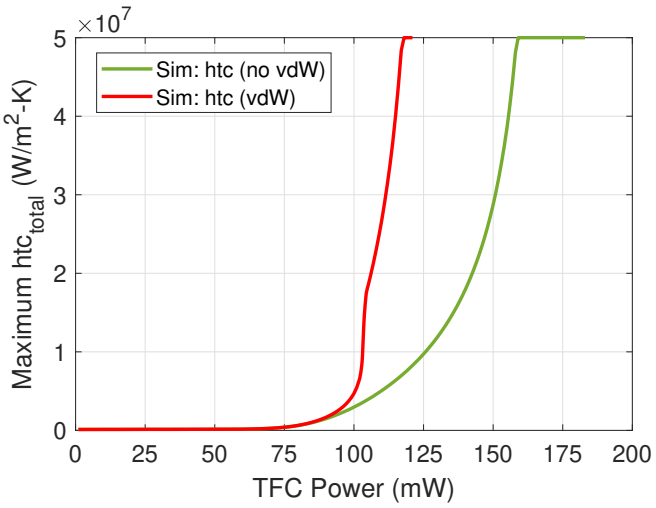

Figure 5.6: Maximum htc_{total} vs TFC power for static touchdown simulation on Si in air with initial spacing of 21.3 nm. Solid green curve excludes vdW forces while computing slider's thermal protrusion, while solid red curve considers vdW forces while computing slider's thermal protrusion.

shows a steeper drop in the ECS temperature curve than the simulation without vdW forces and agrees much better with the experiment.

We plot the maximum htc_{total} vs TFC Power for the simulations with and without vdW forces in Figure 5.6. Since vdW forces accelerate the touchdown process, the simulation with vdW forces (solid red curve) shows a steeper rise in the htc_{total} curve than the simulation without vdW forces (solid green curve). This steeper rise in htc_{total} for the simulation with vdW forces explains the corresponding sharper drop in the ECS temperature curve in Figure 5.4, compared to the simulation without vdW forces.

We plot the ECS temperature and the maximum disk (i.e. Si wafer) temperature as a function of the TFC power for the simulations with and without vdW forces in Figure 5.7. As the spacing h decreases, the net heat transfer coefficient htc_{total} increases (Figure 5.5). Hence, as the TFC power is increased (causing h to decrease), the head and the disk (i.e. Si wafer) temperatures near the ECS location approach each other, as shown in Figure 5.7. Since we limit htc_{total} to an interface thermal conductance of 5e7 W/m^2·K for head-Si interface, the head and disk temperatures are never exactly equal even at and beyond touchdown. Rather we see a temperature jump of $\sim 6 - 9$ ° C between the head and the disk at the ECS location beyond touchdown. The value of this temperature jump depends on the assumed interface thermal conductance.

We plot the surface temperature profile of the slider ABS and the top surface of the Si wafer (i.e. the surface directly underneath the slider ABS) in Figures 5.8 and 5.9. These temperature plots correspond to a TFC power of 80 mW for the simulation with vdW forces.

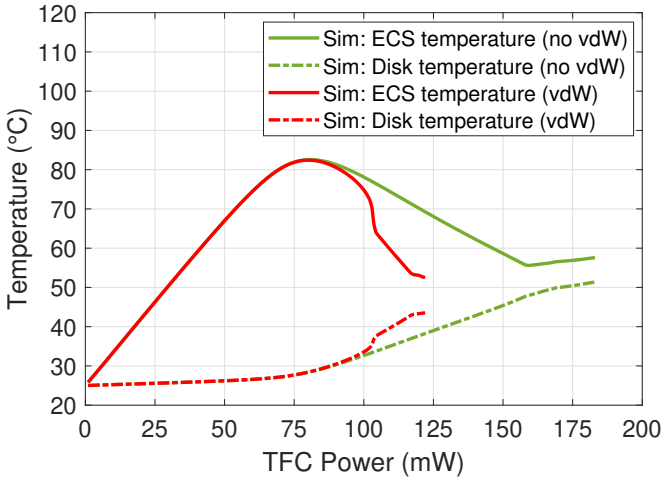

Figure 5.7: Static touchdown simulation on Si in air with initial spacing of 21.3 nm. Solid green curve and dashed green curve are the ECS temperature and maximum disk (i.e. Si wafer) temperature for the simulation that excludes vdW forces while computing slider's thermal protrusion. Solid red curve and dashed red curve are the ECS temperature and maximum disk (i.e. Si wafer) temperature for the simulation that includes vdW forces while computing slider's thermal protrusion

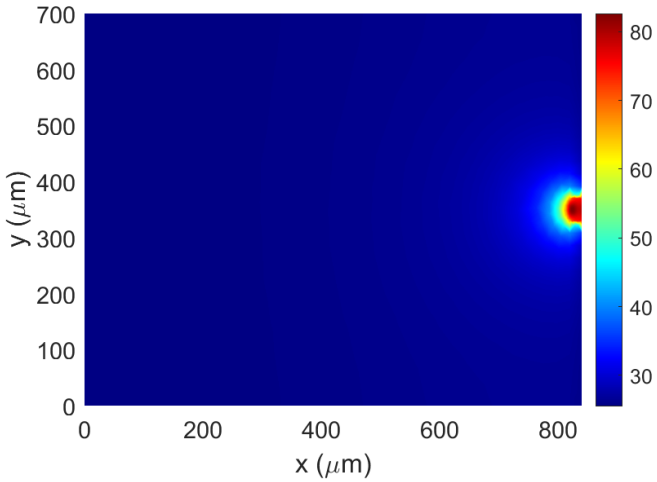

Figure 5.8: Slider temperature profile on ABS at TFC power of 80 mW for static touchdown simulation on Si in air with initial spacing of 21.3 nm, including the effect of vdW forces

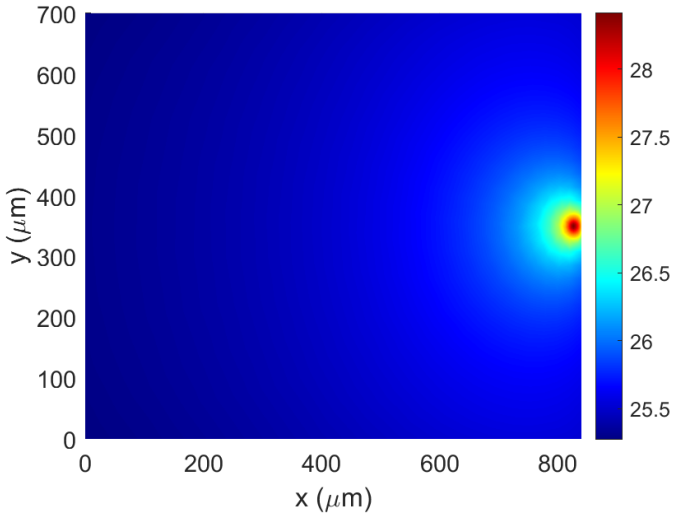

Figure 5.9: Disk (i.e. Si wafer) surface temperature profile at TFC power of 80 mW for static touchdown simulation on Si in air with initial spacing of 21.3 nm, including the effect of vdW forces

The slider temperature profile shows a localized hotspot near the trailing edge of the slider ($x = 840\mu$m), close to its centerline ($y = 350\mu$m) due to TFC heating. A corresponding localized hotspot is observed in the Si wafer surface temperature profile due to heat transfer from the head.

Air Conduction vs Phonon Conduction

To isolate the effect of air conduction on ECS cooling, we performed touchdown experiments in vacuum and compared the simulation with and without air conduction (including vdW forces) with the experiment in air and in vacuum (Figure 5.10). When we include air conduction in the model, htc_{total} increases during the initial TFC heating zone (0-66 mW). This causes the ECS temperature to drop, which explains why the red curve is below the black curve from 0 to 66 mW. A lower ECS temperature causes a smaller TFC protrusion, leading to a larger spacing and hence a smaller htc_{phon} for the simulation with air as compared to that without air. Hence the ECS temperature is lower for simulation without air (black curve) than that with air (red curve) for TFC power $>$ 66 mW (when phonon conduction dominates). The shift in the ECS curve with/without air conduction agrees well with the shift in the experiment in air vs vacuum. Since the media is stationary in this experiment, air conduction has a small effect on the ECS temperature (as opposed to the flying case over a rotating disk, where air cooling would have a more significant impact).

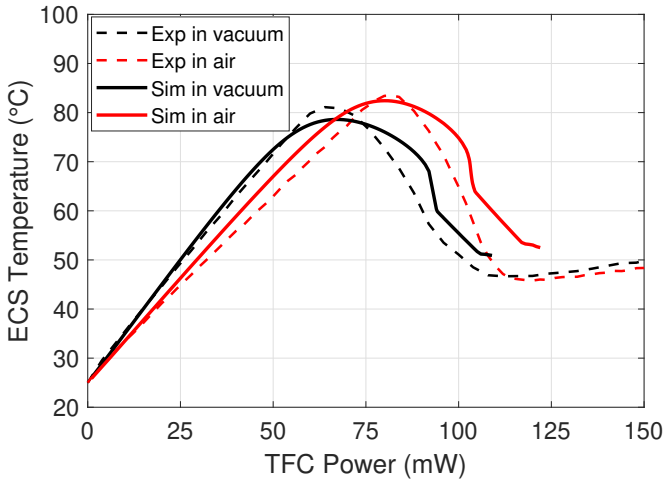

Figure 5.10: Static touchdown simulation on Si in air (htc_{air} included) and in vacuum (htc_{air} excluded) and comparison with experiment in air and in vacuum. Initial spacing is 21.3 nm; vdW forces are included.

Effect of Spacing

As the initial ECS-media spacing is increased in the experiment, the peak ECS temperature increases and the peak is attained at a higher TFC power (Figure 5.11). The same trend is observed in the simulated ECS temperature curve, as the initial spacing is increased from 21.3 nm to 31.7 nm. Moreover, for both initial spacings, we use the same value of A, B in Eq. (5.9). A good quantitative match between the experiment and simulation for both spacings strongly suggests that vdW force is responsible for the steep drop in the ECS cooling curve.

Effect of Media

To study the effect of media on ECS cooling, we performed touchdown experiments on Perpendicular Magnetic Recording (PMR) disks with AlMg and glass substrates (Figure 5.12) and compared the results with the touchdown curve on Si. Figure 5.13 plots the simulated ECS temperature vs TFC power for static touchdown on AlMg disk and glass disk and comparison with corresponding experiments. We also plot the ECS temperature vs TFC power curve for static touchdown experiment on Si wafer as a reference in Figure 5.13. Figure 5.14 plots the ECS temperature and maximum disk temperature as a function of the TFC power during the static touchdown simulation on these three media materials (Si wafer, AlMg disk, glass disk).

PMR disks have a multi-layered structure (Figure 5.12) comprising of lube, DLC (diamond-

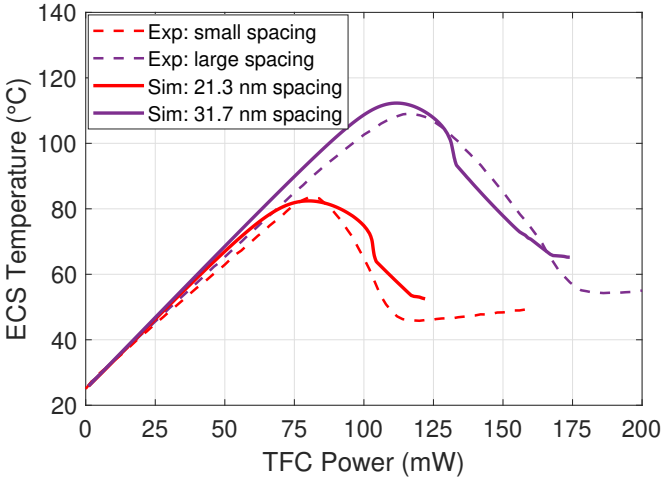

Figure 5.11: Static touchdown simulation on Si in air with initial spacing of 21.3 nm, 31.7 nm (with vdW) and comparison with two experiments performed at different initial spacings in air. Since we do not know the initial spacing in the experiment, we choose the initial spacing in the simulation to ensure a good fit with the experiment.

like-carbon), magnetic layers (CoCrPt, Ru, CoFe) and the substrate (AlMg or glass). Since the characteristic dimension along the surface ($\sim \mu$m) is much larger than the height of the disk layers ($\sim$nm), we model the effect of the layers by computing an "effective thermal conductance" (tc) of the layered structure, which is defined as

$$\frac{1}{tc} = \Sigma_i \left(\frac{L_i}{k_i} + \frac{1}{h_i} \right) \quad ; \quad k_i(L_i) = \frac{k_{i,bulk}}{1 + \frac{4\Lambda_{bulk}}{3L_i}} \tag{5.10}$$

$$Q_{total} = htc_{total}(T_s - T_d) = tc(T_d - T_d') \tag{5.11}$$

Here L_i is the thickness of the i^{th} layer, k_i is the thin-film thermal conductivity of the layer material, h_i is the interface thermal conductance between layers i, $i+1$. This approximation assumes that the temperature varies linearly along each layer thickness (i.e. heat flux along the z direction remains a constant through the layers). Accordingly, the temperature difference between the top surfaces of the disk (T_d) and the AlMg substrate (T_d') is determined using Eq. (5.11).

We assume h_i = 4e9 W/m^2·K for metal-metal interfaces [123] and h_i = 1e8 W/m^2·K for metal-dielectric interfaces [120]. The reduced thermal conductivity of each magnetic layer $k_i(L_i)$ due to boundary scattering is determined using Matthiessen's rule [124] in Eq. (5.10) (we assume bulk mean free path of electrons, Λ_{bulk} in the magnetic layer is 40 nm). The bulk thermal conductivity of the magnetic layer materials, $k_{i,bulk}$ can be found in Ref. [125]. k_i

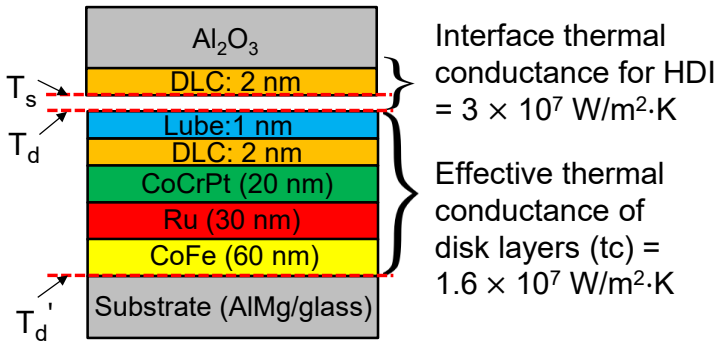

Figure 5.12: PMR disk multi-layered structure.

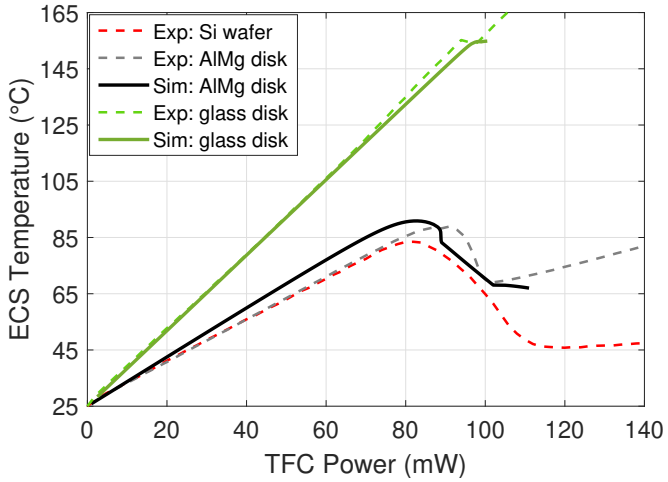

Figure 5.13: ECS temperature vs TFC power for static touchdown of head on different media materials (Si wafer vs AlMg disk vs glass disk) in air: comparison between simulations and experiments

of DLC is 1 W/m·K and that of the lube is 0.07 W/m·K. [29, 126] With these assumptions, *tc* for the AlMg disk layers is computed as 1.6e7 W/m^2·K.

The interface thermal conductance for the HDI is expected to be sensitive to the disk roughness and is assumed to be 3e7 W/m^2·K. This value is chosen such that the touchdown simulation on the AlMg disk in air with vdW and initial spacing of 24 nm (solid black curve in Figure 5.13) agrees with the experiment (dashed grey curve in Figure 5.13). Using the same layered structure, we simulate the touchdown curve for the glass disk in air with vdW and initial spacing of 41 nm (solid green curve in Figure 5.13), which also agrees well with

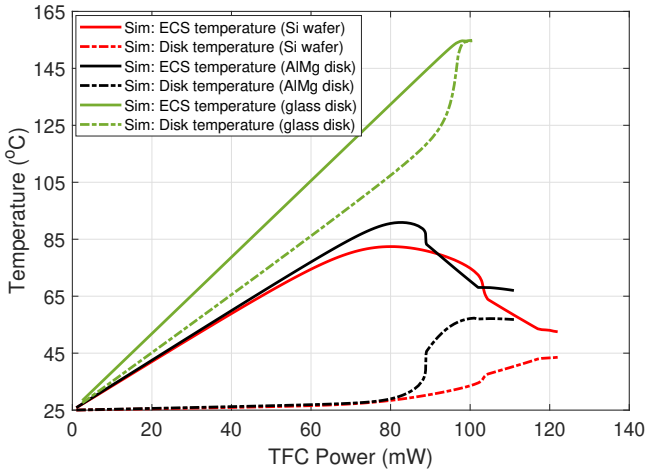

Figure 5.14: Effect of media material (Si wafer vs AlMg disk vs glass disk) on head cooling during static touchdown experiment in air. Solid curves plot the simulated ECS temperature and dashed curves plot the simulated maximum disk temperature vs TFC power.

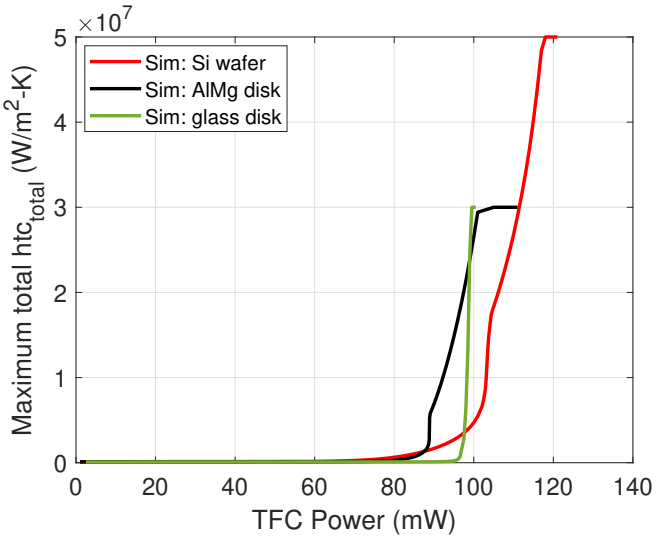

Figure 5.15: htc_{total} vs TFC power for static touchdown simulation on Si wafer, AlMg disk and glass disk.

the experiment (dashed green curve in Figure 5.13).

If the media is a good thermal conductor, it is able to effectively diffuse the heat transferred from the head, leading to stronger cooling of the ECS. Glass has a much lower thermal conductivity (0.9 W/m·K) than Si (148 W/m·K). Hence the glass disk heats up a lot during static touchdown (Figure 5.14), leading to a very small drop in the ECS cooling curve, compared to Si wafer.

AlMg has a comparable thermal conductivity (117 W/m·K) [127] to Si (148 W/m·K), yet shows a smaller drop in the touchdown curve than Si. The layers on top of the AlMg substrate (tc = 1.6e7 W/m^2·K) make the AlMg disk an overall poor conductor (compared to Si), causing the AlMg disk to heat up more than Si wafer during static touchdown (Figure 5.14). The presence of the disk layers, along with lower thermal conductance for the HDI (3e7 W/m^2·K for head-AlMg disk vs 5e7 W/m^2·K for head-Si, which is possibly caused by larger RMS surface roughness of the AlMg disk: S_q = 0.2 nm than that of Si: S_q = 0.1 nm), account for the smaller drop in the simulated touchdown curve on AlMg disk compared to Si. We plot a comparison of htc_{total} vs TFC Power for Si, Al-Mg disk and glass disk in Figure 5.15.

5.4 Conclusion

We have developed a numerical model to simulate the head temperature due to heat transfer across a closing nanoscale gap between the head and the media (non-rotating) and compared our results with static touchdown experiments performed with a head resting on three different media (Si, magnetic disks with AlMg and glass substrates). The TFC heater in the head is powered to create a local protrusion, leading to contact of the ECS that is used to measure the temperature change.

As the ECS approaches the media with increasing TFC power, enhanced phonon conduction heat transfer causes a drop in the ECS temperature vs TFC power curve. Our model shows that the introduction of van der Waals forces between the head and the media during computation of the head's thermal protrusion causes a steeper drop in the simulated ECS temperature curve, ensuring a good quantitative match with experiments for all of the media materials tested and different initial ECS-media spacings. We isolate the effect of air conduction and phonon conduction on ECS cooling by comparing our simulations with experiments performed in air vs vacuum. We also find that the media material significantly impacts the amount of ECS cooling: a good conductor (like Si) shows a large cooling drop, whereas a poor conductor (such as glass disk) shows a small cooling drop.

This chapter presents results published in Applied Physics Letters in 2019 (reproduced from [128], with the permission of AIP Publishing) and 2020 (reproduced from [129] with the permission of AIP Publishing) and presented at ISPS 2019 [130].

Chapter 6

Investigation of Nanoscale Heat Transfer Between a Flying Head and Rotating Disk

6.1 Introduction

Understanding head cooling via heat transfer in the HDI is imperative to develop reliable head and media designs for contemporary PMR drives and particularly for emerging technologies such as HAMR and MAMR. Furthermore, with the minimum fly height of less than 5 nm in contemporary HDDs, it is imperative to consider heat transfer due to near field radiation and phonon conduction [22–25, 105, 106] in addition to traditional air conduction [18, 19] to accurately predict head/media temperatures in HDDs.

In Chapter 5, we performed static touchdown experiments and simulations to study phonon conduction driven heat transfer between the head and the non-rotating media. We found that inclusion of phonon conduction, intermolecular forces (vdW forces) and disk temperature rise is essential to accurately predict the ECS temperature during static touchdown of the head on the media. In this study, we aim to answer the next logical question: how much do phonon conduction, disk temperature rise and intermolecular forces impact the ECS temperature of a flying slider over a rotating disk?

While the effect of intermolecular forces in the HDI was considered in our previous static touchdown study (Chapter 5), the roughness of the head and the disk was ignored. To consider the combined effect of intermolecular forces, head/disk roughness and partial/complete head-disk contact, asperity based intermolecular adhesion force and contact force models are needed. Zheng & Bogy used the sub-boundary lubrication model which was proposed by Stanley et al. [131] to study the behaviour of a TFC slider flying at near-contact [132]. They found the fly height is significantly affected by interfacial forces in the HDI (such as adhesion force, contact force, friction force etc.). Moreover, these interfacial forces also compromise the stability of the slider while flying at near-contact [132–134]. Since nanoscale heat transfer

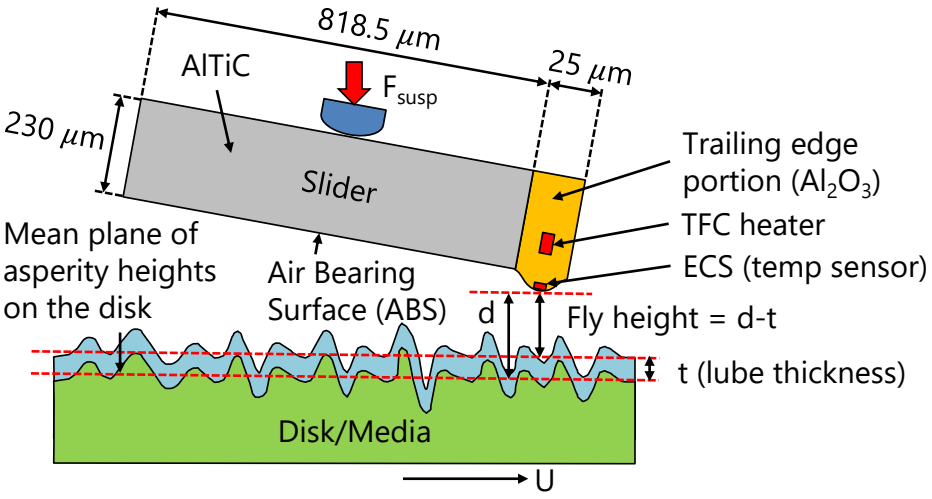

Figure 6.1: Schematic of the Head-disk interface (HDI)

is spacing dependent, it is expected that intermolecular adhesion and contact forces would impact the temperature profile of a flying slider.

Recently Zheng et al. numerically and experimentally studied the effect of the disk temperature rise on the ECS temperature for a flying slider over a rotating disk [114]. They found that excluding the effect of disk temperature rise (i.e. treating the disk as an ideal heat sink) overestimates the cooling of the slider in the simulation. However, they did not study the ECS temperature change due to heat transfer in the HDI at and beyond contact conditions. Beyond contact, heat generation due to friction between the head and the sliding disk is expected to increase the ECS temperature [135, 136].

In this chapter, we introduce a numerical model to predict the slider temperature profile and the fly height for a flying TFC slider over a rotating disk. Subsequently, we compare our simulation results with touchdown experiments performed with a magnetic recording head flying over a rotating Al-Mg disk. The TFC heater is energized, causing a localized protrusion near the flying slider's trailing edge and the ECS is utilized to record the temperature change during this process (Figure 6.1). The simulations and experiments are performed over a range of TFC powers starting from a fly height of $\sim$ 9-12 nm all the way down to contact and beyond. To accurately predict the fly height and heat transfer in the HDI, we incorporate the effects of disk temperature rise, asperity based adhesion & contact force models, air & phonon conduction heat transfer and friction heating in our model. We study the effect of each of these features on the ECS temperature and the fly height during the flying touchdown process.

We first discuss the methodology used to compute the adhesion and contact forces and the net heat flux in the HDI. Next, the overall simulation schematic, including the slider thermo-mechanical model, the rotating disk thermal model and the air bearing model is

presented. This is followed by a discussion of results and the conclusion.

This work was completed jointly with Qilong Cheng and Amin Ghafari. Qilong performed the flying touchdown experiments. Amin developed the model to compute the phonon conduction heat transfer coefficient. I developed the numerical model and performed simulations to predict the head temperature, disk temperature and fly height during touchdown of a flying slider using air and phonon conduction heat transfer coefficients. I also performed simulations using Amin's model to compute the phonon conduction heat transfer coefficient for the HDI.

6.2 Model Description

Adhesion and Contact Forces

To accurately predict the fly height at near-contact, it is necessary to account for the interactions between the rough slider and the lubricant/rough disk using asperity-based intermolecular adhesion force and contact force models. In this study, we use the sub-boundary lubrication model which was proposed by Stanley et al. [131]. A rough surface (slider/disk) is described using three topological roughness parameters: standard deviation of asperity heights, mean radius of curvature of asperities and areal density of asperities. This model converts the problem of two contacting rough surfaces (slider and disk) to the equivalent simpler problem of contact between a rigid infinitely smooth surface (slider) and a nominally flat surface (disk) having combined roughness parameters of the individual surfaces. Accordingly, σ_s is the standard deviation of asperity heights for the combined slider/disk surfaces, R is the mean radius of curvature of asperities for the combined slider/disk surfaces and η is the areal density of asperities for the combined slider/disk surfaces. We note that σ_s is related to σ (the standard deviation of surface heights for the combined slider/disk surfaces) as described in Ref. [131].

Next, the total intermolecular adhesion force F_a between the slider and the lubricated disk is obtained as [131, 132]

$$F_a = \eta A_n \left(\int_{-\infty}^{d-t} \frac{8}{3}\pi R\delta\gamma \left[\left(\frac{\epsilon}{d-u-t+\epsilon}\right)^2 - \frac{1}{4}\left(\frac{\epsilon}{d-u-t+\epsilon}\right)^8 \right] \phi(u)\mathrm{d}u + 2\pi R\delta\gamma \int_{d-t}^{d} \phi(u)\mathrm{d}u \right. \\ \left. + \int_{d}^{\infty}\int_{r_t}^{\infty} \frac{8}{3}\frac{\delta\gamma}{\epsilon} \left[\left(\frac{\epsilon}{z-t+\epsilon}\right)^3 - \left(\frac{\epsilon}{z-t+\epsilon}\right)^9 \right] 2\pi r\mathrm{d}r\phi(u)\mathrm{d}u \right) \tag{6.1}$$

where A_n is the nominal contact area, d is the distance between the mean plane of asperity heights on the disk and the slider ABS (Figure 6.2), t is the lubricant thickness, $\delta\gamma$ is the adhesion energy per unit area for the HDI, ϵ is the equilibrium inter-molecular separation, u is the asperity height and $\phi(u)$ is the probability density function of asperity heights. We assume that $\phi(u)$ is a Gaussian distribution with a mean of zero and a standard deviation of

σ_s. In the third integral in Eq. (6.1), z is the separation of solid surfaces outside the contact region at a radius r, and r_t is the radius at the intersection of the lubricant and solid (see Figure 6.2). The expression for z and r_t can be found in Refs. [131, 132]. We note that since d is the distance between the mean plane of asperity heights on the disk and the slider ABS, the fly-height (i.e. actual air bearing height) is defined as $h = (d - t)$ (as shown in Figure 6.1). Eq. (6.1) considers three types of asperities on the disk (as shown in Figure 6.2) - (1) non-contacting asperities (described by the first integral), (2) lubricant-contacting asperities (described by the second integral) and (3) solid-contacting asperities (described by the third integral).

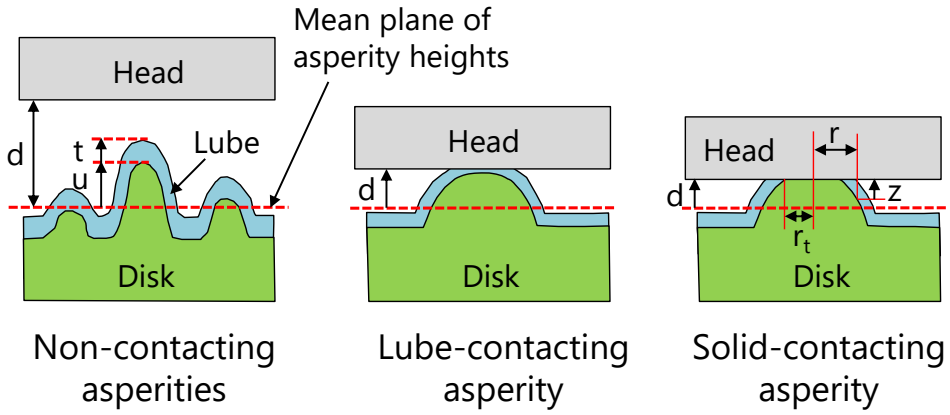

Figure 6.2: Schematic of non-contacting, lubricant-contacting and solid-contacting asperities

The contact force F_c between the slider and the disk is obtained using the well-known Greenwood-Williamson model and is given by

$$F_c = \frac{4}{3}\eta A_n E R^{1/2} \int_d^\infty (u - d)^{3/2} \phi(u) \mathrm{d}u \tag{6.2}$$

where E is the combined Hertz elastic modulus of the two surfaces. The adhesion and contact force parameters used in Eqs. (6.1), (6.2) are summarized in Table 6.1.

HDI Heat Transfer Coefficient

During flying touchdown of the slider on the disk, four major heat transfer schemes exist: air conduction (htc_{air}), viscous dissipation (htc_{visc}), phonon conduction (htc_{phon}) and radiation (htc_{rad}).

$$htc_{HDI} = htc_{air} + htc_{visc} + htc_{phon} + htc_{rad} \tag{6.3}$$

The heat transfer coefficient for conduction through air (htc_{air}) is a function of the air bearing height $h = (d - t)$, pressure p_{air} and temperature $T_{air} = \frac{(T_s + T_d)}{2}$ and can be obtained

Table 6.1: Adhesion/contact force parameters [132, 134, 137–141]

Combined standard deviation of surface heights σ (nm)	0.5
Combined mean radius of asperities R (nm)	20
Combined asperity density η ($1/\mu\text{m}^2$)	5000
Equilibrium intermolecular distance ϵ (nm)	0.3
Adhesion energy per unit area $\delta\gamma$ (N/m)	0.1
Lubricant thickness t (nm)	1
Hertz elastic modulus E (GPa)	148.56

by solving the energy equation using temperature jump theory [18, 19].

$$htc_{air} = \frac{k_{air}}{h + 2\frac{2-\sigma_T}{\sigma_T}\frac{2\gamma}{\gamma+1}\frac{1}{Pr}\lambda_{air}} \tag{6.4}$$

Here $\lambda_{air}(h, p_{air}, T_{air})$ is the effective mean free path of air molecules at pressure p_{air} and temperature T_{air} accounting for boundary scattering [19] (with a nominal value of 67.1 nm for no boundary scattering and at ambient pressure and temperature). k_{air} is the effective thermal conductivity of air accounting for boundary scattering (with a nominal value of 0.0261 W/(m-K) for no boundary scattering). σ_T is the thermal accommodation coefficient, $Pr = 0.71$ is the Prandtl number of air and $\gamma = 1.4$ is the ratio of specific heats for air. We assume that $\sigma_T = 0.6$ in our calculations [142, 143]. This value ensures that the slope of the simulated ECS temperature change vs TFC power curve in the initial linear regime agrees well with the corresponding experiment (see Figure 6.14 in subsequent section "Comparison with Experiments"). We note that since $\lambda_{air} \propto p^{-1}$, htc_{air} increases as the air bearing pressure p_{air} increases.

The heat transfer coefficient due to viscous dissipation (htc_{visc}) can be neglected compared to air conduction (htc_{air}) for small gap sizes [18] and hence is ignored in this study.

We use a wave-based phonon conduction theory to model the enhanced nanoscale heat transfer due to van der Waals force driven migration of phonons from one half-space to the other [23, 25, 105]. Using the methodology outlined in Section 5.2 in Chapter 5, we compute the phonon conduction heat transfer coefficient for the HDI (htc_{phon}) as a function of h, $\hat{T}_d$ and $\Delta\hat{T} = \hat{T}_s - \hat{T}_d$. Here $\hat{T}_d$ and $\hat{T}_s$ are the disk and slider surface temperatures respectively.

We ignore radiative heat transport in this study, since htc_{rad} ($\sim 10^3$ W/m^2·K) [24] is typically much smaller than htc_{phon} ($\sim 10^6$ W/m^2·K) at nanoscale spacings. Thus, the net heat transfer coefficient in the HDI is approximated as:

$$htc_{HDI} \approx htc_{air} + htc_{phon} \tag{6.5}$$

Friction Heating Flux

The net heat generation per unit contact area due to friction heating is given by [135]

$$q_{fric} = \mu p U \tag{6.6}$$

Here μ is the coefficient of friction, p is the net normal pressure in the HDI due to the contact force and the adhesion force [144] and U is the linear disk speed. We assume a heat partition factor of 0.5 in our model [135] so that the heat flux due to friction heating into the slider ($q_{fric,s}$) and the disk ($q_{fric,d}$) is given by $q_{fric,s} = q_{fric,d} = 0.5 q_{fric}$.

Slider Thermo-mechanical Model

We determine the slider temperature profile $T_s(x, y, z)$ and thermal protrusion due to TFC heating using a thermo-mechanical finite element model (ANSYS). The net heat flux into the slider ABS due to heat transfer in the HDI and heat generation due to friction is given by

$$q_s = -htc_{HDI}(\hat{T}_s - \hat{T}_d) + q_{fric,s} \tag{6.7}$$

We note that $T_s(x, y, z)$ and $T_d(x, y, z)$ are the temperature profiles in the slider and the disk respectively. On the other hand, $\hat{T}_s(x, y) = T_s(x, y, z = 0)$ is the slider ABS surface temperature and $\hat{T}_d(x, y) = T_d(x, y, z = 0)$ is the disk top surface temperature profile (as shown in Figure 6.3).

As shown in Figure 6.1, the slider is composed of two parts - a block of 818.5 μm x 700 μm x 230 μm that is made of AlTiC (thermal conducitivity of 20 W/m·K) [10] and a block of 25 μm x 700 μm x 230 μm (called the trailing edge or TE portion) that is made of Al_2O_3 (thermal conductivity of 1.8 W/m·K) [10]. We use a similar model as Chapter 5 to account for the presence of the metallic components in the TE body (such as the NiFe reader, Cu writer and NiFe shields), which have a much higher thermal conductivity (35 W/m·K for NiFe, 403 W/m·K for Cu) [10] than Al_2O_3. These metallic components are present near the ABS in a volume of 25 μm x 30 μm x 35 μm and are described in our model using an effective thermal conductivity of 50 W/m·K and an effective thermal expansion coefficient of 8e-6 K^{-1} as described in Section 5.2 in Chapter 5. Using a similar slider model, we obtained a good agreement between simulations and experiments for static touchdown of the head on different media materials (AlMg disk, glass disk and Si wafer), in different environments (air, vacuum) and at different head-media spacings in our previous study (Chapter 5).

We perform a static thermal finite element analysis to compute the slider temperature profile (T_s) due to TFC joule heating. We consider a convection coefficient of 100 W/m^2·K on the side surfaces and a larger convection coefficient of 2000 W/m^2·K) on the back surface of the slider to account for metal fixture cooling [74]. The heat flux q_s from Eq. (6.7) is applied on the ABS. This temperature profile (T_s) is subsequently used to determine the thermal protrusion of the slider using a static structural finite element analysis. We also account for the air bearing pressure, adhesion force and contact force on the ABS in this simulation.

Disk Thermal Model

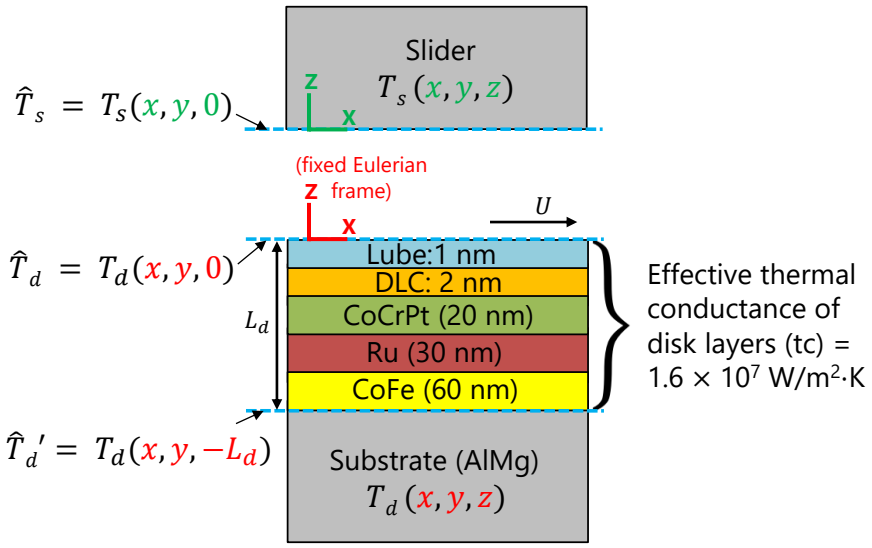

Figure 6.3: PMR head and multi-layered disk schematic

As the disk rotates underneath the flying hot slider, heat transfers from the slider to the part of the disk which is underneath the slider at any given time. Hence, the temperature of each material point on the disk varies periodically and does not reach a steady state. However, if we consider a frame of reference that is fixed with the slider and use Eulerian co-ordinates, the temperature field in the disk ($T_d(x,y,z)$) reaches a steady state in this frame [114]. Ignoring the skew of the slider, the temperature profile of the disk in this frame is given by

$$\rho C_p U \frac{\partial T_d}{\partial x} = \nabla.(k \nabla T_d) \tag{6.8}$$

Here ρ is the density, C_p is the specific heat capacity, U is the linear disk speed and k is the thermal conductivity. The net heat flux into the disk due to heat transfer from the slider and heat generation due to friction heating is obtained as

$$q_d = htc_{HDI}(\hat{T}_s - \hat{T}_d) + q_{fric,d} \tag{6.9}$$

Eq. (6.8) subject to boundary condition Eq. (6.9) determines the disk temperature profile.

We describe the thin layers (lubricant, Diamond-like-Carbon, magnetic layers) on the top of the AlMg substrate of the PMR disk (Figure 6.3) using an "effective thermal conductance" ($tc = 1.6 \times 10^7$ W/m^2·K) in our model (same as Chapter 5). This approximation assumes that the temperature varies linearly along each layer thickness (i.e. heat flux along the z direction remains a constant through the layers). Accordingly, we compute the temperature jump between the top surface of the PMR disk ($\hat{T}_d$) and the top surface of the AlMg substrate

($\hat{T}'_d = T_d(x, y, z = -L_d)$) as (see Figure 6.3)

$$q_d = tc(\hat{T}_d - \hat{T}'_d) \tag{6.10}$$

Assuming that the AlMg disk substrate can be approximated as a semi-infinite medium, the temperature profile of the top surface of the AlMg substrate ($\hat{T}'_d$) is determined using the analytical solution of Eq. (6.8) as [145].

$$\begin{aligned} \hat{T}'_d(x, y) &= T_0 + \int\int \frac{q_d(x', y')}{2\pi k R} e^{-\frac{U\rho C_p}{2k}(R-(x-x'))} \mathrm{d}x' \mathrm{d}y' \\ R &= \sqrt{(x-x')^2 + (y-y')^2} \end{aligned} \tag{6.11}$$

Here $T_0 = 298$ K is the ambient temperature. ρ, C_p, k for AlMg can be found in Ref. [125]. Eqs. (6.9), (6.10) and (6.11) together describe the temperature profile of the top surface of the disk $\hat{T}_d$.

Air Bearing Pressure Solver

The governing equation for the air bearing pressure profile in the HDI is the steady state generalized Reynolds equation. The non-dimensional form of this equation is: [146, 147]

$$\frac{\partial}{\partial X}\left(\hat{Q}PH^3\frac{\partial P}{\partial X} - \Lambda_x PH\right) + \frac{\partial}{\partial Y}\left(\hat{Q}PH^3\frac{\partial P}{\partial Y} - \Lambda_y PH\right) = 0 \tag{6.12}$$

where $X = x/L$, $Y = y/L$, $P = p/p_a$, $H = h/h_m$ are the non-dimensionalized x coordinate (along the slider's length direction), y coordinate (along the slider's width direction), air bearing pressure and spacing respectively. Here L is the slider's length, p_a is the ambient pressure and h_m is the reference spacing at the slider's trailing edge center. $\Lambda_x = 6\mu UL/p_a h_m^2$ and $\Lambda_y = 6\mu VL/p_a h_m^2$ are the bearing numbers in the x and y directions, where μ is the air viscosity and U and V are the x and y disk velocity components. Since the minimum spacing h can be lower than 5 nm, which is small compared to the mean free path of air ($\lambda = 63.5$ nm at ambient temperature and pressure), the no-slip boundary condition does not hold and hence a flow factor $\hat{Q}$ is introduced to account for rarefaction effects. CML Air uses the Fukui–Kaneko slip correction factor: $\hat{Q} = f(K_n/PH)$, where $K_n = \lambda/h_m$ is the Knudsen number and f is given by Fukui and Kaneko [146, 148].

We use a modified version of the CML Air static simulation program [147] to solve the generalized Reynolds equation. CML Air uses Patankar's control volume method [76] with a multigrid solver to discretize and solve Eq. (6.12) for a given flying attitude (nominal fly height, pitch and roll) [147]. In order to obtain the slider's equilibrium flying attitude at a given suspension load, CML Air starts by solving Eq. (6.12) and computing the air bearing pressure distribution using an initial guess for the flying attitude. Next, a Quasi-Newton iteration method is applied to search for a new guess for the flying attitude. Iterations are performed, until the new updated flying attitude ensures the balance between the suspension load and the air bearing pressure.

The sub-boundary lubrication model [131] is implemented in the modified CML Air

program by regarding the slider ABS as an infinitely smooth surface with combined roughness parameters being applied on the disk surface (see Table 6.1) [132, 149]. The asperity heights on the disk are described by a Gaussian distribution function $\phi(u)$ with a mean of zero and a standard deviation σ_s. This asperity-based model enables us to solve the generalized Reynolds equation at near-contact and contact conditions when the fly height $(d-t)$ becomes 0 or even negative [133, 149]. This approach also considers the effect of air pressure loss at asperities which are in contact during determination of the air bearing force and the air conduction heat flux [133, 149]. The ABS profile is modified with the simulated TFC protrusion [149] using the slider thermo-mechanical finite element model to account for the fly height change due to TFC actuation. The equilibrium flying state of the slider is then determined by balancing the forces and torques on the slider due to adhesion and contact forces (Eqs. (6.1), (6.2)), the suspension load and the air bearing pressure [132, 149].

Overall Simulation Methodology

The simulated TFC protrusion profile determined by the slider thermo-mechanical model is used to compute the steady state fly-height and air bearing pressure using the modified CML Air program (accounting for adhesion and contact forces in the HDI using Eqs. (6.1), (6.2)). The fly height, air pressure p_{air}, slider surface temperature $\hat{T}_s$ and disk surface temperature $\hat{T}_d$ are used to compute the heat flux into the slider and disk q_s, q_d using Eqs. (6.5), (6.6), (6.7), (6.9). q_s and q_d are further used as boundary conditions to determine the slider temperature profile $T_s(x, y, z)$ and the disk temperature profile $T_d(x, y, z)$. T_s, p_{air} and the computed adhesion and contact forces on the ABS in the modified CML Air are used to determine the slider TFC heating-induced protrusion profile. The resultant non-linear problem involving the modified CML Air, the slider thermo-mechanical model and the disk thermal model is solved using Broyden's Quasi-Newton method [122]. The overall simulation schematic is summarized in Figure 6.4.

We note that our model considers the effect of intermolecular forces in two different ways. Firstly, the effect of intermolecular forces is considered on the phonon conduction heat transfer coefficient htc_{phon} through the reflection coefficient (see Eqs. (5.4), (5.5), (5.6) from Chapter 5). Secondly, we also consider the effect of intermolecular forces while determining the steady state fly height of the slider in modified CML Air and while computing thermal protrusion of the slider using the slider thermo-mechanical model through the adhesion force (Eq. (6.1)).

6.3 Results and Discussion

Phonon Conduction Heat Transfer Coefficient

In Chapter 5, we determined htc_{phon} as a function of h, $\hat{T}_d$ and $\Delta\hat{T} = \hat{T}_s - \hat{T}_d$ for the HDI, assuming that the slider material is Al_2O_3 and the disk material is AlMg/glass. We found

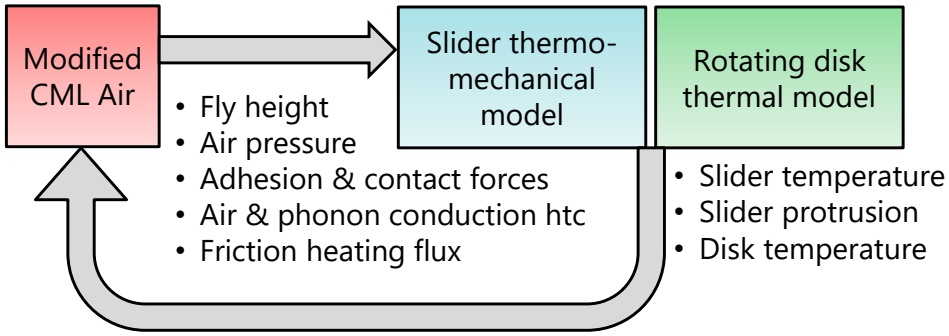

Figure 6.4: Overall simulation model schematic

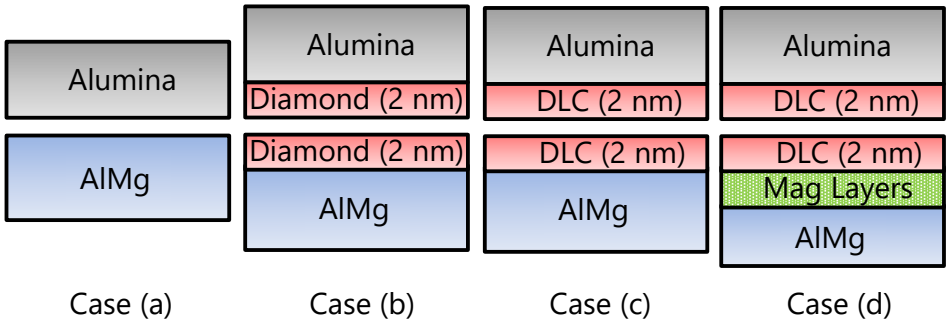

Figure 6.5: Phonon conduction calculation cases

that htc_{phon} can be well approximated with the following equation (0.1 nm $\leq h \leq$ 100 nm, 4 K $\leq \Delta\hat{T} \leq$ 400 K, 298 K $\leq \hat{T}_d \leq$ 398 K)

$$ln(htc_{phon}) = c_1 ln(h) + c_2 ln\left(\frac{\Delta\hat{T}}{400}\right) + c_3 ln\left(\frac{\hat{T}_d}{298}\right) + b \tag{6.13}$$

Parameters c_1, c_2, c_3, b depend on the material properties of both half-spaces (ρ_ν, c_ν and ω_D). However, we did not consider the effect of the diamond-like-carbon (DLC) films on the slider/disk and the magnetic layers on the disk (Figure 6.3) in Chapter 5. Other studies have shown that addition of a diamond film to the disk can significantly reduce the phonon conduction heat transfer coefficient [23]. To understand the effect of slider/disk DLC films and disk magnetic layers on phonon conduction, we consider 4 cases as shown in Figure 6.5:

(a) Al_2O_3 - gap - AlMg

(b) Al_2O_3 - 2 nm Diamond layer - gap - 2 nm Diamond layer - AlMg

Table 6.2: Density, acoustic wave speed and Debye frequency of different materials for computation of htc_{phon} [125, 126, 150]

Material	ρ_ν (kg/m^3)	c_ν (m/s)	ω_D ($\times 10^{15}$ rad/s)
Alumina	3980	7133	0.1179
AlMg	2660	3420	0.056
Diamond	3500	13850	0.2919
DLC	2800	4167	0.1593
CoCrPt	8900	2844	0.06
Ru	12300	2295	0.0726
CoFe	8514	2601	0.06

(c) Al_2O_3 - 2 nm DLC layer - gap - 2 nm DLC layer - AlMg

(d) Al_2O_3 - 2 nm DLC layer - gap - 2 nm DLC layer - mag layers - AlMg

The material properties (ρ_ν, c_ν, ω_D) of all the layers are summarized in Table 6.2. We use bulk Diamond properties for the Diamond layer (case b) and thin film DLC properties for the DLC layer (cases c and d). The thin film DLC acoustic wave speed is estimated from the elastic properties and density of a 2.2 nm DLC film from Ref. [150]. The acoustic wave speed of the magnetic layer materials is estimated from the elastic properties and density from Ref. [125].

The resultant htc_{phon} as a function of h for cases (a), (b), (c), (d) are plotted in Figure 6.6. Our results show that the addition of a 2 nm Diamond layer (with bulk Diamond properties) reduces the phonon conduction heat transfer coefficinet by 1 to 2 orders of magnitude (which is consistent with previously published results in Ref. [23]). However, addition of a 2 nm DLC layer (with thin film DLC properties) has a relatively small effect on htc_{phon}. Similarly, addition of a 2 nm DLC layer and magnetic layers also has a relatively small effect on htc_{phon}. Nevertheless, we use the simulation curve for case (d) for all the simulations in this study. For case (d), the parameters in Eq. (6.13) are obtained as: $c_1 = -1.99$, $c_2 = -0.83$, $c_3 = 0.99$, $b = 11.4$.

Effect of Disk Temperature Rise

In this section, we study the effect of the disk temperature rise on the ECS temperature. Figure 6.7 plots the ECS temperature change vs the TFC power for the simulations with and without the disk temperature model. In the simulation with the disk temperature model, the disk temperature rise is determined using the methodology described in the Section "Disk Thermal Model". In the simulation without the disk temperature model, the disk

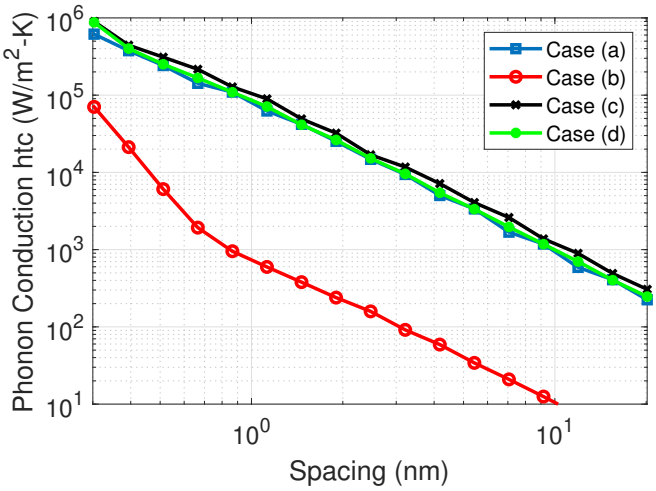

Figure 6.6: Phonon conduction heat transfer coefficient as a function of spacing h for cases (a), (b), (c), (d). $\Delta\hat{T} = 400$ K, $\hat{T}_d = 298$ K

is assumed to be an ideal heat sink and hence the disk temperature is always equal to the ambient temperature everywhere (i.e. $T_d(x, y, z) = T_0 = 298$K). Both simulations include heat transfer due to both air and phonon conduction. For now, adhesion and contact forces and friction heating are excluded in both simulations.

In both simulations, initially, the ECS temperature increases with increasing TFC power due to larger joule heating generated at the higher TFC power. However, as the flying head approaches the rotating disk with a further increase in TFC power, enhanced nanoscale heat transfer in the HDI due to air conduction and phonon conduction causes the ECS temperature to decrease. Our results indicate that the simulation without the disk temperature model overestimates the ECS cooling drop compared to the simulation with the disk temperature model. We note that a similar trend was observed in Ref. [114]. The heat flux from the slider to the disk is directly proportional to the temperature difference between the slider and the disk surfaces (Eq. (6.7)). Treating the disk as an ideal heat sink overestimates the heat flux in the HDI and hence overestimates the ECS cooling drop.

Effect of Adhesion and Contact Forces

The adhesion and contact forces in the HDI are computed as a function of the fly height using eqs. (6.1), (6.2) and are plotted in Figure 6.8. We note that adhesion force being attractive is negative and the contact force being repulsive is positive. We also note that d is the distance between the mean plane of asperity heights on the disk and the slider ABS and the fly height is defined as $(d - t)$, hence the fly height becomes negative when the head protrusion penetrates into the lubricant. We see that as the fly height becomes smaller

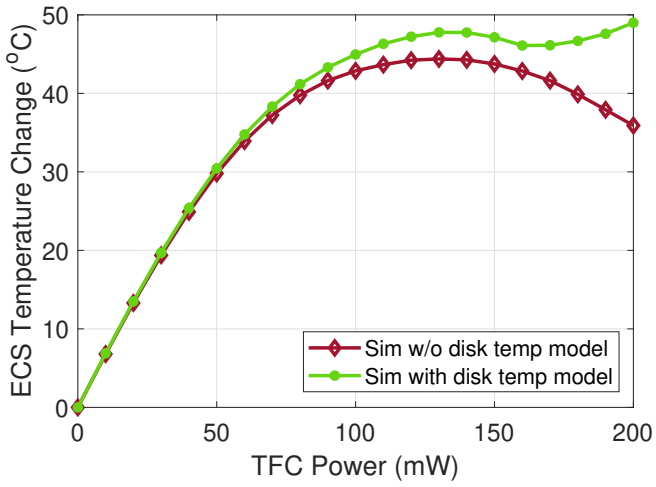

Figure 6.7: Effect of disk temperature rise on the ECS temperature change

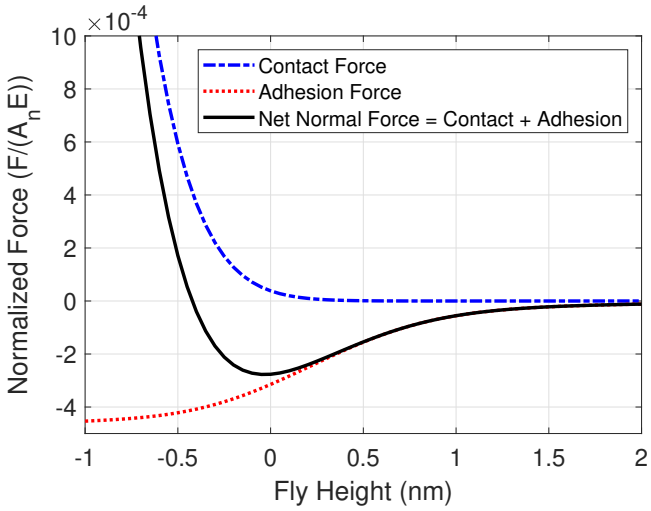

Figure 6.8: Adhesion and contact forces in the HDI as a function of the fly-height $(d - t)$

than $\sim$ 1 nm, the magnitude of the adhesion force starts increasing due to enhanced head-lubricant-disk interactions, causing the net normal force to decrease. As the fly height is further decreased causing the head to penetrate through the lubricant and come into contact with the disk asperities, the contact force increases rapidly, causing the net normal force to increase.

In order to study the effect of adhesion/contact forces on fly height and nanoscale heat transfer, we perform simulations with and without adhesion/contact forces. We plot the minimum fly height vs the TFC power for the simulations with and without adhesion/contact forces in Figure 6.9. Both simulations include the disk temperature rise model and heat transfer due to both air and phonon conduction. Friction heating is excluded in both simulations.

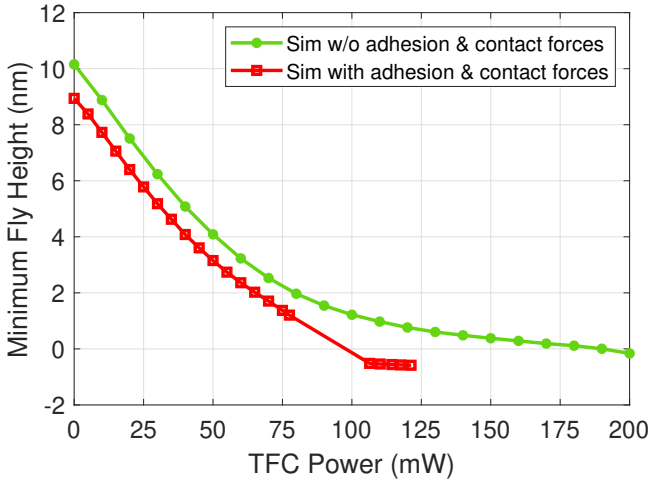

Figure 6.9: Comparison between simulations with and without adhesion & contact forces: minimum fly height $(d - t)$

The simulation with adhesion/contact forces has a lower fly hieght (8.94 nm) than the simulation without adhesion/contact forces (10.16 nm) at TFC power = 0 mW. This is because attractive adhesion forces between the head and the disk cause the head to fly at a lower spacing. As the TFC power is increased and the minimum fly height decreases below $\sim$ 1.2 nm (TFC power $>$ 77.5 mW), the magnitude of the adhesion force starts increasing (Figure 6.8), causing the simulation with adhesion/contact forces to reach touchdown at a lower TFC power than the simulation without adhesion/contact forces (Figure 6.9). Moreover, since the adhesion force acts in a direction opposite to the air bearing force, the slider looses stability when the increase in the air bearing force can no longer balance the rapid increment in adhesion force [132]. Hence, we do not find stable equilibrium fly heights between 77.5 mW and 106.4 mW. The slider regains stability when it comes into contact with

the disk at TFC power of 106.4 mW (minimum fly height = - 0.52 nm). The rapidly growing contact force adds on to the air bearing force (Figure 6.8) thereby restoring the stability of the HDI [132]. We use the approach discussed in Refs. [132, 151] to determine the stability of an equilibrium state.

The instability in the fly height of TFC sliders at near-contact has been observed in several previous simulation studies [132–134, 139]. This instability has also been observed experimentally in literature using an LDV to measure slider vertical vibration and AE signal to monitor contact at the HDI [152–154]. To model the slider behavior during this unstable region, simulations need to be performed with a dynamic air bearing program (such as the CML Air dynamic simulation program) so as to capture the bouncing vibrations of the slider [133, 134].

The loss of slider stability with rapidly increasing adhesion forces beyond 77.5 mW makes the convergence of the simulation scheme (Figure 6.4) challenging. Hence, to simplify the highly non-linear calculations at near-contact, we use the methodology from Ref. [132] - we set the slider protrusion profile at TFC power of 70 mW as a baseline and proportionally alter this profile for TFC power beyond 77.5 mW for the simulation with adhesion/contact forces.

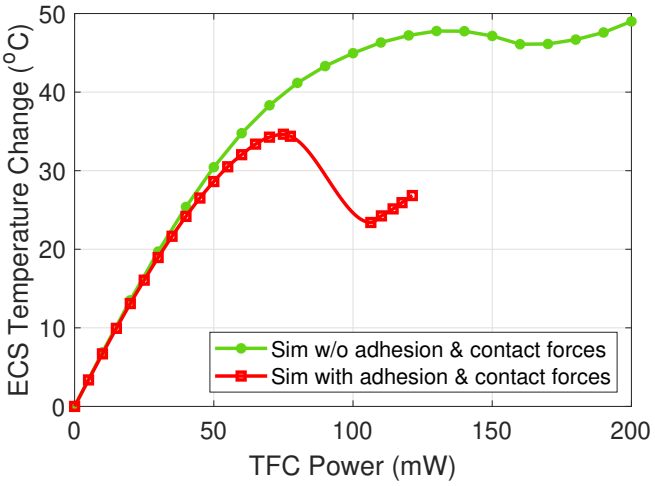

Figure 6.10: Comparison between simulations with and without adhesion & contact forces: ECS temperature change

We plot the ECS temperature change vs the TFC power for the simulations with and without adhesion/contact forces in Figure 6.10. As the head-disk spacing decreases, the heat transfer coefficient due to air conduction as well as phonon conduction increases (Eq. (6.4), Fig. 6.6). Hence, as the head approaches the disk with increasing TFC power, enhanced heat transfer in the HDI due to both air conduction and phonon conduction leads to a drop

in the ECS temperature change vs TFC power curve. The simulation with adhesion/contact forces has a smaller spacing and hence a larger heat transfer coefficient than the simulation without adhesion/contact forces (Figure 6.9). Hence, the simulation with adhesion/contact forces shows a smaller ECS temperature and a steeper ECS cooling drop than the simulation without these forces in Figure 6.10.

We note that we observed a similar trend (compared to Figure 6.10) in our previous static touchdown simulation study (Figure 5.4 in Chapter 5), where the simulation with intermolecular forces showed a steeper ECS cooling drop and predicted a smaller static touchdown power than the simulation without intermolecular forces.

Effect of Phonon Conduction

The net heat transfer coefficient in the HDI has two dominant contributions: air conduction and phonon conduction (Eq. (6.5)). To isolate the effects of air conduction and phonon conduction, we performed simulations with and without phonon conduction heat transfer htc_{phon} and plot the ECS temperature change vs TFC power curve for both cases in Figure 6.11. Both simulations consider air conduction heat transfer htc_{air}, the disk temperature rise model and adhesion/contact forces. Friction heating is excluded in both simulations.

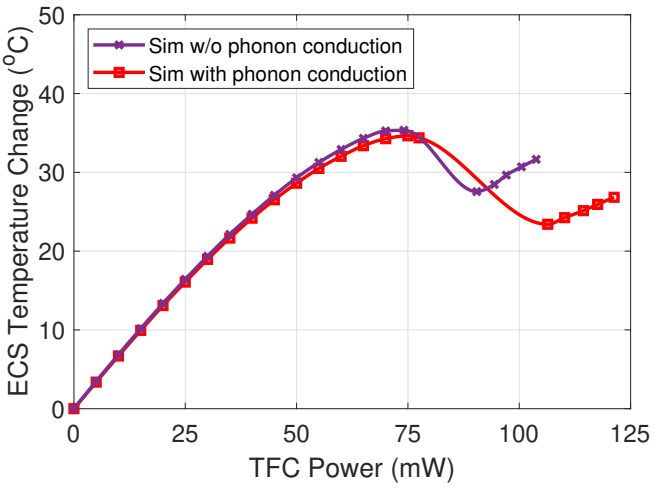

Figure 6.11: Comparison between simulations with and without phonon conduction: ECS temperature change. Both simulations consider air conduction.

For TFC power $<$ 77.5 mW (i.e. fly height $>$ 1.2 nm), simulations with and without phonon conduction give very similar results, indicating that air conduction is the dominant heat transfer mechanism for large fly heights. However, when the fly height becomes smaller than 1.2 nm (TFC Power $>$ 77.5 mW), the simulation with phonon conduction shows a larger

ECS cooling drop than the simulation without phonon conduction. Our results indicate that it is imperative to include phonon conduction heat transfer to accurately predict the ECS temperature at near-contact.

Effect of Friction Heating

In this section, we study the effect of friction heating on the ECS temperature change vs TFC power curve. We plot the results for simulations with friction heating (Eq. (6.6) with $\mu = 0.7$) and without friction heating in Figure 6.12. Both simulations consider the disk temperature rise model, heat transfer due to both air and phonon conduction and adhesion/contact forces.

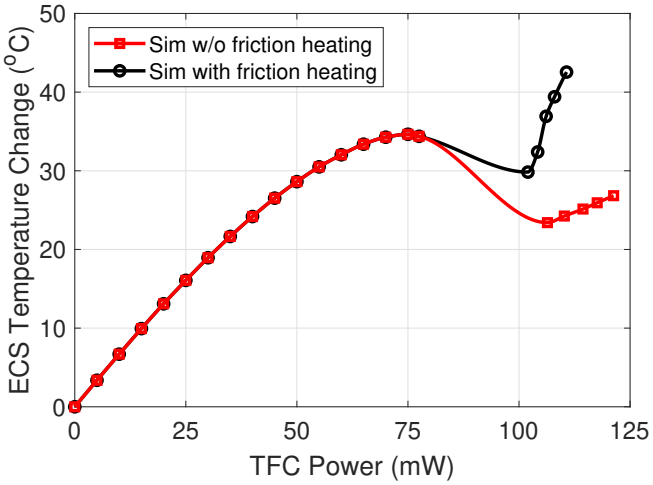

Figure 6.12: Comparison between simulations with and without friction heating: ECS temperature change

As expected, both simulations yield exactly identical results at large fly heights (TFC power $\leq$ 77.5 mW). Further, as noted in the Section "Effect of Adhesion and Contact Forces", we do not find stable equilibrium fly heights and ECS temperatures between 77.5 mW and 106.4 mW for the simulation without friction heating and between 77.5 mW and 102 mW for the simulation with friction heating due to the inclusion of adhesion and contact forces. Beyond contact, the simulation with friction heating shows a larger ECS temperature change and a larger slope of ECS temperature change vs TFC power due to additional heat generated by friction.

Interface Thermal Conductance

We plot the temperature change at the ECS (which is located near the head ABS, see Figure 6.1) and the temperature change at the location on the surface of the disk exactly below

the ECS at different TFC powers in Figure 6.13. We note that this simulation considers the effects of disk temperature rise model, heat transfer due to both air and phonon conduction, adhesion/contact forces and friction heating.

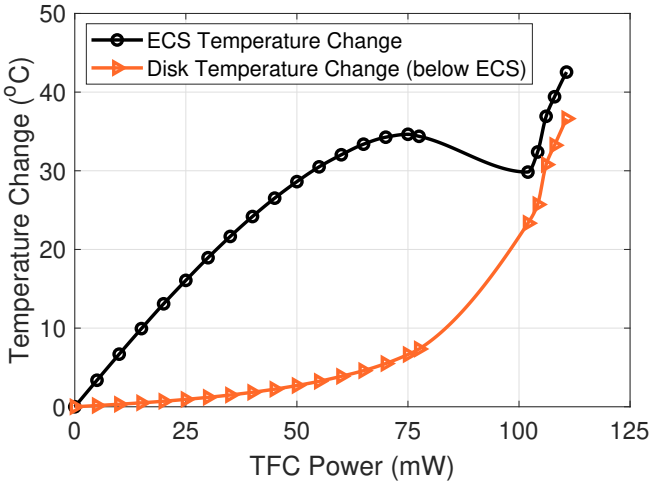

Figure 6.13: Comparison between the temperature change at the ECS (on the head surface) and the temperature change at the location on the disk exactly below the ECS for different TFC powers

As the spacing h decreases, the net heat transfer coefficient in the HDI due to phonon and air conduction, htc_{HDI} increases (Eq. (6.4), Figure 6.6). Hence, as the TFC power is increased (causing h to decrease), the head and the disk temperatures at the ECS location approach each other, as shown in Figure 6.13. In reality, at head-disk contact, htc_{HDI} would be restricted by the interface thermal conductance (or Kapitza conductance) of the HDI. Hence, we enforce an interface thermal conductance of 1.5×10^7 W/m^2·K as an upper bound to htc_{HDI} in our model. Due to the presence of this interface thermal conductance, the head and disk temperatures are not exactly equal even at and beyond touchdown (i.e. TFC power $\geq$ 102 mW). Rather we see a temperature jump of ~ 6 ° C between the head and the disk at the ECS location at contact. The value of this temperature jump depends on the assumed interface thermal conductance.

Comparison with Experiments

Figure 6.14 shows the simulated ECS temperature change vs TFC power curve at 5400 RPM and 7200 RPM and comparison with corresponding experimental curves. The minimum fly height vs TFC power for the simulations at 5400 RPM and 7200 RPM are plotted in Figure 6.15. Both the simulation and the experiment are performed at a radial position of 27 mm.

Both simulations consider the disk temperature rise model, heat transfer due to both air and phonon conduction, adhesion/contact forces and friction heating. The simulation at 5400 RPM is performed with $\mu = 0.7$ and the simulation at 7200 RPM assumes $\mu = 0.5$. The smaller μ at 7200 RPM can be justified by the larger sliding velocity and the larger normal force at 7200 RPM compared to 5400 RPM. All other parameters are kept the same for both simulations (5400 RPM and 7200 RPM).

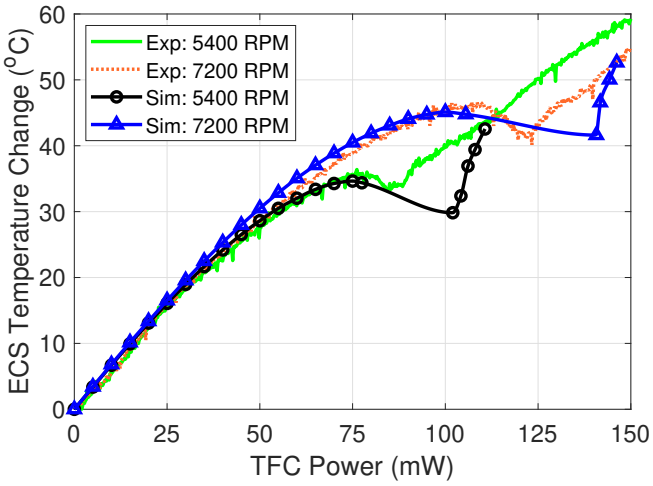

Figure 6.14: Comparison between simulation and experiment at 5400 RPM & 7200 RPM: ECS temperature change

As expected, the simulation at 7200 RPM has a larger fly height (at a given TFC power) and a larger touchdown power than the simulation at 5400 RPM. As explained in the Section "Effect of Adhesion and Contact Forces", we do not find stable equilibrium fly heights and ECS temperatures between 77.5 mW and 102 mW for the simulation at 5400 RPM due to the inclusion of adhesion and contact forces. The simulation at 7200 RPM also shows a similar behavior with no stable equilibrium fly heights and ECS temperatures between 105.5 mW and 140.7 mW.

The value of the thermal accommodation coefficient $\sigma_T = 0.6$ in Eq. (6.4) is chosen such that the slope of the ECS temperature vs. TFC power curve in the initial linear regime in the simulation ($\sim$0.63 °C/mW from 0 to 30 mW) agrees well with the corresponding initial slope in the experiment at 5400 RPM. With $\sigma_T = 0.6$, we see that overall the simulated ECS temperature change vs TFC power curves at both 5400 RPM and 7200 RPM agree reasonably well with corresponding experimental curves even beyond the initial linear regime of 0 to 30 mW.

However, we note that the rate of frictional heating in the simulation is higher than the experimental observation (i.e. slope of ECS temperature change vs TFC power beyond

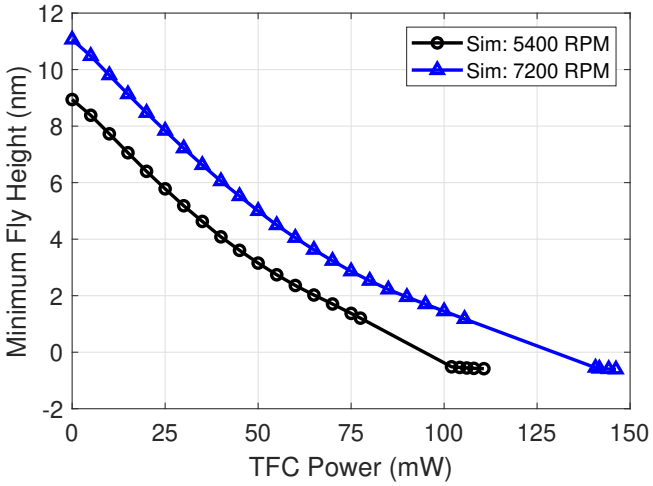

Figure 6.15: Comparison between simulations at 5400 RPM and 7200 RPM: minimum fly-height $(d - t)$

contact is higher in the simulation than the experiment). This may be caused by several factors such as:

- We assume a constant friction coefficient μ at a given sliding velocity in our simulations. In reality, μ is a function of the normal pressure (typically μ decreases with increasing normal pressure). Hence as the TFC power is increased beyond the touchdown power and the contact pressure increases, assuming a constant μ at the higher contact pressure may cause the simulation to overestimate the amount of friction heating.
- The contact force estimated by the simulation (Eq. (6.2)) may be higher than reality, causing the simulation to overestimate friction heating
- The TFC protrusion shape predicted by the simulation at contact and hence the simulation contact area may be different than reality

The simulation model presented in this study can be improved by modeling the detailed head geometry including the reader, writer and shields. While intermolecular van der Waals forces are the driving mechanism for phonon conduction heat transfer between two half-spaces, the high air bearing pressure in the HDI may also enhance the htc_{phon}. Humidity in the HDI can also affect the air pressure, fly height and air conduction/phonon conduction heat transfer coefficients, which is not considered in our study [155]. The accuracy of the simulated ECS temperature and fly height at near-contact can be improved by considering the thermal protrusion of the disk due to the temperature rise. The fly height prediction can be improved by incorporating electrostatic forces in the HDI [133].

6.4 Conclusion

We have introduced a numerical model to predict the slider temperature profile and the fly height for a flying TFC slider over a rotating disk. Next, we compared our simulation results with touchdown experiments performed with a magnetic recording head flying over a rotating Al-Mg disk. Our model considers the effects of disk temperature rise, asperity-based adhesion and contact forces, combined heat transfer due to air conduction & phonon conduction and friction heating to accurately predict the fly height and heat transfer at near-contact. The heat transfer coefficient due to wave-based phonon conduction theory is determined as function of the spacing, the disk surface temperature and the slider-disk surface temperature difference, accounting for the effect of DLC layers on the slider/disk and magnetic layers on the disk.

Initially, the ECS temperature increases with increasing TFC power due to larger joule heating generated at the higher TFC power. However, as the flying head approaches the rotating disk with a further increase in TFC power, enhanced nanoscale heat transfer due to air conduction and phonon conduction leads to a drop in the ECS temperature change vs the TFC power curve until touchdown. Beyond touchdown, the ECS temperature increases again with increasing TFC power. Our results show that the simulation without the disk temperature model overestimates the ECS cooling drop compared to the simulation with the disk temperature model. The incorporation of adhesion force between the head and the disk causes a reduction in the fly height, leading to a smaller touchdown power and a steeper ECS cooling drop than the simulation without adhesion force. The simulation with phonon conduction shows a larger ECS cooling drop compared to the simulation without phonon conduction. The simulation with friction heating predicts a larger ECS temperature and a larger slope of ECS temperature vs TFC power beyond contact. The simulation with disk temperature model, air & phonon conduction, adhesion & contact forces and friction heating agrees well with experiment at different rotational speeds (5400 RPM, 7200 RPM).

The results of this chapter have been submitted for publication in the Journal of Applied Physics [156] and were presented at ISPS 2020 [157].

Chapter 7

Disk Temperature Profile and Thermal Protrusion During HAMR

7.1 Introduction

During HAMR writing, the media is locally heated to $\sim 500\ ^oC$ using a laser, so as to temporarily reduce its coercivity during writing. Successful data writing in HAMR is strongly dependent on attainment of a desirable disk temperature profile. Moreover, laser heating of the media may also cause a thermal protrusion, which can affect the slider's flying performance. While direct measurement of the media temperature profile and thermal protrusion can be challenging, numerical modeling provides a practical way to characterize the thermo-mechanical response of the media and provide guidelines for experiments [50, 158–161]. In this chapter, we present a numerical model to predict the temperature profile of the media and its resultant thermal protrusion during HAMR laser heating. We study the effect of the laser FWHM on the protrusion of the media.

7.2 Model Description

As the disk rotates underneath a stationary laser beam, the laser heats up the part of the disk which is below it at any given time. Hence, the temperature of each material point on the disk varies periodically and does not reach a steady state. However, if we consider a frame of reference that is fixed with the laser and use Eulerian co-ordinates, the temperature field in the disk ($T_d(x, y, z)$) reaches a steady state in this frame [114]. The co-ordinate system is defined such that the X axis is along the direction of the disk velocity and the Z axis is along the thickness of the disk. The origin is located on the top surface of the disk at the center of the laser spot. Ignoring the skew of the slider, the steady state temperature profile of the disk is given by

$$\rho C_p U \frac{\partial T_d}{\partial x} = \nabla.(k \nabla T_d) + q_{gen} \tag{7.1}$$

Here ρ is the density, C_p is the specific heat capacity, U is the linear disk speed and k is the thermal conductivity. q_{gen} is the heat generation rate per unit volume in the media due to laser absorption. We consider a multi-layered HAMR disk geometry (see Figure 7.1) consisting of 10 nm thick FePt storage layer, 15 nm thick MgO interlayer, 80 nm thick heat sink, 100 nm thick NiTa layer and a glass substrate [160, 162]. The effect of the lubricant (1 nm) and the DLC (2 nm) layers is ignored. We assume that heat generation rate per unit volume in the storage layer drops exponentially with the thickness [161]. Further we ignore the heat generation in the other layers of the disk such as the interlayer and the heat sink [163]. Accordingly, q_{gen} in the storage layer is given by

$$\begin{aligned} q_{gen} &= I\beta e^{-\beta z} \\ I &= C\exp\left(-\frac{x^2+y^2}{2\delta^2}\right) \end{aligned} \tag{7.2}$$

Here I is the next flux entering the film from the top surface, which is assumed to be a Gaussian profile centered at the origin with standard deviation δ. β is the storage layer attenuation constant which is assumed to be 0.033 nm^{-1} [161]. C is a constant (with units of heat flux) whose value depends on the laser power, the laser FWHM and the storage layer's optical properties [164].

The thermal conductivity and thermal expansion coefficient of the HAMR disk layers are tabulated in Table 7.1. Material anisotropy is taken into account, assuming out-of-plane and in-plane thermal conductivity ratio is 5 for FePt [158, 162]. We also consider an interface thermal conductance (Kapitza conductance) of 3e8 $\text{W/m}^2\text{K}$ between FePt/MgO and MgO/heat sink interfaces in our model [165].

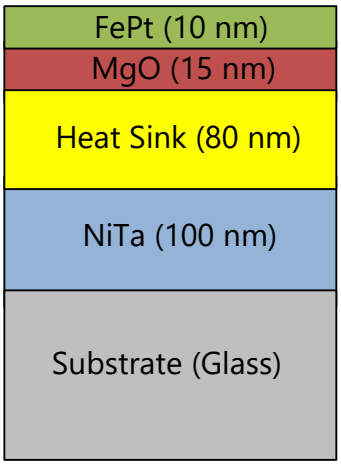

Figure 7.1: HAMR multi-layered disk schematic

Table 7.1: Thermal conductivity (k) and thermal expansion coefficient (α) of disk layers [125, 158, 160, 162, 164]

Material	k (W/m-K)	α (K^{-1})
FePt	2 (in-plane), 10 (out-of-plane)	12e-6
MgO	2	11e-6
Heat Sink	50	17e-6
NiTa	5	13e-6
Glass	1	7.1e-6

We discrete and solve Eq. (7.1) using Patankar's Control Volume method (Hybrid scheme) [76]. We use a 3D spatially non-uniform structured grid to model the layered disk geometry. The resultant disk temperature profile $T_d(x, y, z)$ is inputted into a finite element model (ANSYS) of the media, which is used to determine the thermal protrusion of the media using a quasi-static structural simulation.

7.3 Results and Discussion

Baseline Simulation

We plot the temperature rise of the disk along the cross-track direction (y) and along the thickness (z) direction for laser FWHM = 20 nm in Figures 7.2 and 7.3 respectively. The disk velocity U is set at 20 m/s. The value of the constant C in Eq. (7.2) is adjusted such that the peak temperature rise of the disk is 475 ^{o}C. Due to the inclusion of the Kapitza resistance, we see a temperature jump of 144.8 ^{o}C at the FePt/MgO interface and a temperature jump of 40.6 ^{o}C at the MgO/heat sink interface. Almost all of the temperature drop occurs in the first 25 nm of thickness (i.e. in the storage layer, the interlayer and at the FePt/MgO, MgO/heat sink interfaces) and the temperature rise is negligible in the heat sink. We observe a peak disk protrusion of only 0.11 nm at a laser spot size of 20 nm, as shown in Figure 7.3.

Effect of Spot Size

In this section, we study the effect of the laser FWHM on the temperature profile and thermal protrusion of the media. We plot the temperature rise of the disk along the thickness (z) direction for laser FWHM = 20 nm, 75 nm and 200 nm in Figure 7.5. The resultant disk protrusion profile is plotted in Figure 7.6 along the cross-track direction (y). The disk

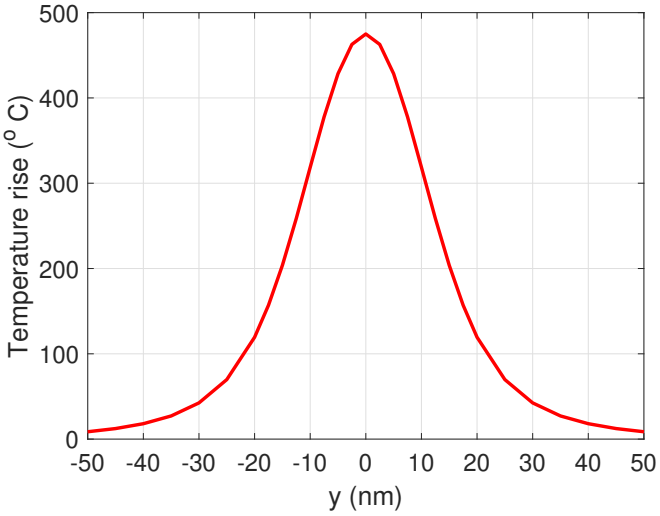

Figure 7.2: Disk temperature profile at $z = 0$ (i.e. top surface of the disk), $x = 0$ along cross-track (y) direction. Laser FWHM = 20 nm, $U = 20$ m/s.

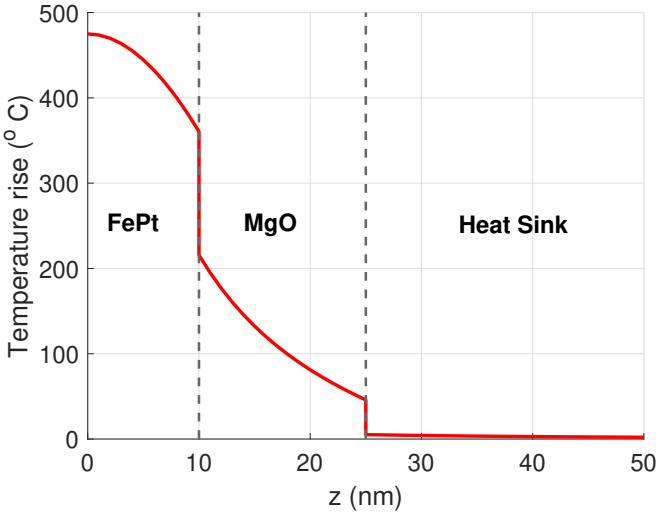

Figure 7.3: Disk temperature profile at the center of the laser beam ($x = 0$, $y = 0$) along thickness (z) direction. Laser FWHM = 20 nm, $U = 20$ m/s.

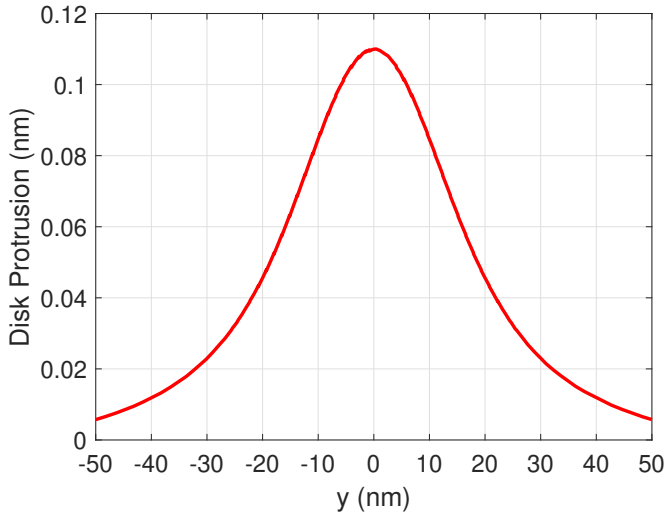

Figure 7.4: Disk Protrusion profile at $z = 0$ (i.e. top surface of the disk) along cross-track (y) direction. Laser FWHM = 20 nm, $U = 20$ m/s.

velocity U is set at 20 m/s. The value of the constant C in Eq. (7.2) is adjusted for all three cases such that the peak temperature rise of the disk is 475 ^{o}C.

As the spot size increases, the peak disk protrusion also increases. The peak protrusion of the media is found to be 0.11 nm, 0.22 nm and 0.57 nm for FWHM of 20 nm, 75 nm and 200 nm respectively. At the small spot size of 20 nm, almost all of the temperature increase due to the laser occurs in the first 25 nm of thickness, with negligible temperature rise in the heat sink (Figure 7.5). Hence, we see a relatively small peak protrusion of 0.11 nm in Figure 7.6. However, as the spot size is increased to 200 nm, we observe a non-negligible temperature rise in the heat sink layer, NiTa layer and even the glass substrate (Figure 7.5). This larger heat penetration through the thickness causes a correspondingly larger peak disk protrusion of 0.57 nm (Figure 7.6).

7.4 Conclusion

In this chapter, we have developed a numerical model to predict the temperature profile of the media and its resultant thermal protrusion during HAMR laser heating. We find that close to the HAMR target spot size (20 nm), the disk protrusion is quite small (0.11 nm). However, for larger spot sizes, like those generated by the HAMR waveguide (200 nm), the disk protrusion can be relatively large (0.57 nm).

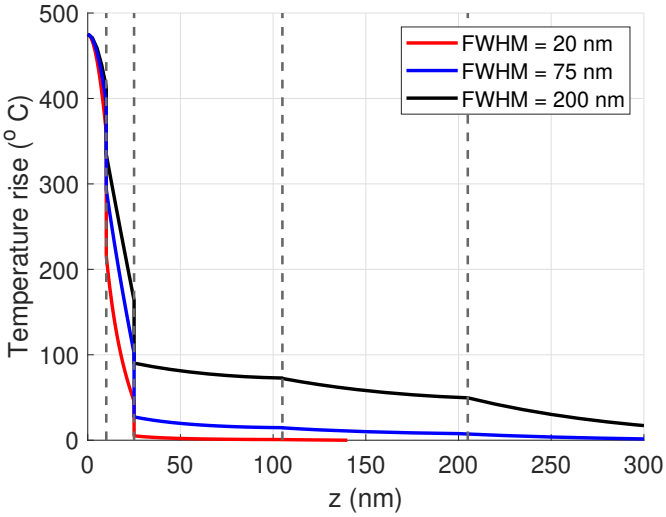

Figure 7.5: Disk temperature profile at the center of the laser beam ($x = 0$, $y = 0$) along thickness (z) direction for FWHM = 20 nm, 75 nm and 200 nm

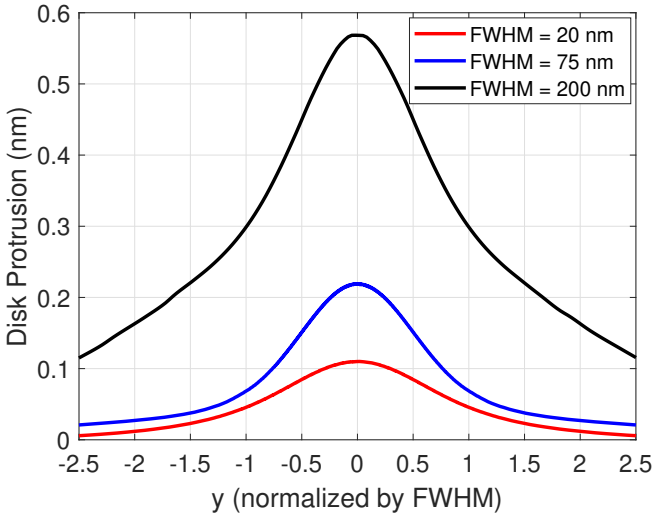

Figure 7.6: Disk Protrusion profile at $z = 0$ (i.e. top surface of the disk) along cross-track (y) direction for FWHM = 20 nm, 75 nm and 200 nm

Chapter 8

Conclusion and Future Work

8.1 Conclusion

Technologies such as Heat-Assisted Magnetic Recording and Microwave-Assisted Magnetic Recording are under rapid development to decrease magnetic media bit sizes below the superparamagnetic limit so as to achieve the HDD storage density targets of 1–10 Tb/in^2. However, addition of new components required for the energy-assist in HAMR/MAMR leads to high temperatures in the head, making head failure due to overheating an increasing concern for both these technologies. Moreover, the high thermal gradient on the disk during HAMR writing causes the lubricant to deform and transfer to the slider, leading to additional reliability issues such as write-induced head contamination. This dissertation investigates the deformation, media-to-head transfer and recovery of the media lubricant during HAMR laser heating through numerical simulations. Further, we perform simulations to investigate nanoscale heat transfer in the HDI during static as well as flying conditions and compare our computations with experiments.

Chapter 2 presents a viscous model for lubricant transfer from the disk to the head during HAMR writing. This model simultaneously determines the thermocapillary stress-driven deformation and evaporation of the lubricant film on the disk, the convection and diffusion of the vapor phase lubricant in the air bearing and the evolution of the condensed lubricant film on the slider. The model also considers molecular interactions between disk–lubricant, slider–lubricant and lubricant–lubricant in terms of disjoining pressure. We investigate the effect of media temperature, head temperature and initial lubricant thickness on the lubricant transfer process for the PFPE lubricant, Zdol. We find that the transfer mechanism is initially largely thermally driven. However, as the amount of lubricant accumulation increases with time, a change in the transfer mechanism occurs from thermally driven to molecular interactions driven (dewetting instability). A similar change in transfer mechanism is predicted as the head–disk spacing is reduced.

While lubricant behavior is traditionally modeled using viscous lubrication theory in the HDD industry, PFPE lubricants are viscoelastic fluids and are expected to exhibit a

combination of viscous and elastic behavior at the timescale of HAMR writing. Hence, we introduce a modification to the traditional (viscous) Reynolds lubrication equation using the linear Maxwell (viscoelastic) constitutive equation and a slip boundary condition in Chapter 3. We study the deformation of the viscoelastic lubricant due to laser heating under the influence of thermocapillary stress and disjoining pressure. Our results show that the deformed lubricant profile (under a 20-nm scanning laser spot) consists of an elastic trough centered at the laser location, followed by a viscous trail. Slippage increases the flow rate of the lubricant, causing larger viscous deformations.

Subsequently, in Chapter 4, we use this modified lubrication equation for the viscoelastic lubricant to develop a model that predicts the media-to-head lubricant transfer during HAMR writing for two PFPE lubricants - Zdol and Ztetraol. Our results show a significant difference between the rates of transfer for Zdol ($\sim$ ns) vs Ztetraol ($\sim$ μs). The amount of transfer increases with the lubricant molecular weight. The purely viscous model underpredicts the deformation of the disk lubricant and also grossly over-predicts the amount of transfer. The amount of transfer decreases on increase in slip length and increase in disjoining pressure. We find a larger amount of transfer at higher media temperatures and larger initial disk lubricant thicknesses. Finally, we study the recovery of the viscoelastic lubricant when the laser is turned off. We find that the elastic trough recovers instantaneously ($\sim$ns), leaving behind the viscous trail, which recovers over a time scale of μs.

In Chapter 5, we present a numerical model to simulate the head and media temperature profiles due to nanoscale heat transfer between the head and the non-rotating media. We compare our simulations with static touchdown experiments performed with a slider resting on three different media (Si, AlMg disk and glass disk). The TFC heater in the head is powered to create a local protrusion, leading to head-media contact and the ECS is used to detect the temperature change. The net heat transfer coefficient due to phonon conduction and air conduction is integrated into a finite element model to simulate the head/media temperature profiles and the head-media spacing using a non-linear thermo-mechanical simulation. As the head approaches the media with increasing TFC power, enhanced phonon conduction causes a drop in the ECS temperature vs TFC power curve. Our model shows that the introduction of van der Waals forces between the head and the media during computation of the head's thermal protrusion causes a steeper drop in the simulated ECS temperature curve, ensuring a good quantitative match with experiments for all of the media materials tested, different initial head-media spacings and in different environments (air vs vacuum). We find that the media material significantly impacts the amount of ECS cooling: a good conductor (like Si) shows a large cooling drop, whereas a poor conductor (such as glass disk) shows a small cooling drop.

In Chapter 6, we develop a numerical model to predict the temperature profile and the fly height for a flying slider over a rotating disk. We compare our simulations with touchdown experiments performed with a flying TFC slider embedded with the ECS, which helps us detect the temperature change. To accurately predict the heat transfer and fly height at near-contact, we incorporate the effects of disk temperature rise, intermolecular adhesion & contact forces, air & phonon conduction heat transfer and friction heating in our

model. As the head approaches the disk with increasing TFC power, enhanced nanoscale heat transfer leads to a drop in the ECS temperature change vs TFC power curve. We find that the exclusion of the disk temperature rise causes the simulation to overestimate the ECS cooling drop. The incorporation of adhesion force results in a smaller touchdown power. The addition of phonon conduction in the model causes a larger ECS cooling drop. The simulation with friction heating predicts a larger ECS temperature slope beyond contact. The simulation with these features agrees with the experiment.

In Chapter 7, we develop a numerical model to predict the temperature profile of the media and its resultant thermal protrusion during HAMR writing. We find that the protrusion of the media is quite small (0.11 nm) at the HAMR target spot size of 20 nm. However, for larger spot sizes, like those generated by the HAMR waveguide (200 nm), the disk protrusion can be relatively large (0.57 nm).

Our hope is that our findings would provide a better understanding of the mechanism of heat and mass transfer in the HDI and would contribute towards managing head overheating and contamination in HAMR and MAMR drives. While our investigation is of direct relevance to the HDD industry, our methodology for modeling the behavior of nanoscale viscoelastic lubricant films and insight into understanding the impact of enhanced nanoscale heat transfer would appeal to a broader scientific community.

8.2 Future Work

In this dissertation, we use the Linear Maxwell model to describe the behavior of the lubricant during HAMR laser heating (Chapters 3 and 4). In order to estimate the magnitude of non-linear viscoelastic effects, we compared the lubricant deformation using the non-linear elastic neo-hookean model with our Linear Maxwell model, in the limit $De \to \infty$. While our preliminary results suggest that the non-linear effects are relatively small in the elastic limit, nevertheless, the model presented here can be improved by using a non-linear viscoelastic constitutive equation (for example, differential model like the upper-convected Maxwell model [95] or integral model like the K-BKZ model). Moreover, at high shear strains, viscosity reduction could occur due to shear thinning [103], an effect that we have not considered in this dissertation. Itoh et al. have reported occurrence of shear thinning in PFPE lubricants using Fiber Wobbling Experiments [89]. As a first order approximation, we can assume that shear thinning decreases the viscosity and maxwell relaxation time ($\eta(\dot{\gamma})$, $\lambda(\dot{\gamma})$), while the shear modulus is unaffected (G = constant). With this assumption, if shear thinning does occur, we would expect to see larger, viscous deformations in the lubricant response.

In Chapter 5, we present static touchdown simulations for different media materials and in air/vacuum environments. However, the effect of humidity on heat transfer was not considered. Static touchdown experiments performed at different humidity levels suggest that nanoscale heat transfer in the HDI is significantly impacted by relative humidity (RH) level for RH $>$ 75 % [129]. Simulations need to be performed to understand how humidity

in the HDI and the formation of a water layer on the head/disk at very high humidity levels affects the air and phonon conduction heat transfer in the HDI.

In Chapter 5, we performed static thermal and structural simulations to predict the steady state temperature distribution and thermal protrusion of the slider during static touchdown. Transient thermal and structural simulations need to be performed and compared with the transient data from the static touchdown experiment to understand the timescales of heat diffusion in the slider and thermal protrusion of the slider when subjected to a step TFC power input.

The simulation models presented in Chapter 5 and 6 can be extended to HAMR and MAMR drives. The thermo-mechanical finite element head model needs to be modified by adding additional components such as the laser diode, the waveguide and the NFT for HAMR and the STO for MAMR. At the time of this writing, fully functional HAMR and MAMR heads are still not available to us for study. Once they are available, experiments and simulations can be performed using these heads to study nanoscale heat transfer during static and flying touchdown. It would be interesting to see how the ECS cooling drop observed during both static and flying touchdown in Chapters 5 and 6 is impacted by laser heating of the media during HAMR and the high current density in the STO in MAMR heads. In Chapter 5 and 6, we have investigated how heat transfers from the hot head (due to TFC Joule heating) to the cool media. In the case of HAMR, two types of heat flow occurs - firstly, far away from the NFT, where the head is hotter than the media, we would still have heat flux from the head to the media (similar to the results in Chapters 5 and 6). Secondly, close to the NFT, the media is hotter ($\sim$500 ^{o}C) than the head ($\sim$300 ^{o}C). Hence, here we would expect a back-heating flux from the media to the head. Simulations and experiments need to be performed by applying the methodology developed in Chapters 5 and 6 to actual HAMR heads to understand these two types of heat flow.

Furthermore, the disk-to-head lubricant transfer and resultant head contamination could in turn affect the heat transfer in the HDI [29] and also alter the slider's fly height. Simulations can performed using the methodology developed in Chapter 6 to investigate how the contamination buildup on the slider ABS could affect the ECS temperature and fly height.

Finally, the author wants to express his sincere hope that the technical challenges of HAMR and MAMR can be conquered and either or both of these products can be released to the public soon.

Bibliography

[1] *IDC Data Age 2025 Report.* URL: https://www.seagate.com/files/www-content/our-story/trends/files/idc-seagate-dataage-whitepaper.pdf. (accessed: 07.13.2020).

[2] R. Fontana and G. Decad (IBM Systems). "The 2018 Storage Landscape – An 11 Year Perspective (2008-2019) LTO Tape Media, HDD, NAND". In: *Designing Storage Architectures for Digital Collections,* Library of Congress, Washington DC, September 9-10 (2019). URL: http://www.digitalpreservation.gov/meetings/DSA2019/Day_1/03_fontana_2018-Storage-Landscape-09092019.pdf. (accessed: 07.13.2020).

[3] J. Handy. *Are SSDs Approaching Price Parity with HDDs?* URL: https://thessdguy.com/are-ssds-approaching-price-parity-with-hdds/. (accessed: 07.13.2020).

[4] *IBM 350 disk storage unit.* URL: https://www.ibm.com/ibm/history/exhibits/storage/storage_350.html. (accessed: 07.13.2020).

[5] *Seagate Exos X16 16TB ST16000NM001G Datasheet.* URL: https://www.seagate.com/www-content/datasheets/pdfs/exos-x16-DS2011-2-1910US-en_US.pdf. (accessed: 07.13.2020).

[6] T. E. Karis. "Lubricants for the Disk Drive Industry". In: *Lubricant Additives: Chemistry and Applications.* Ed. by L. R. Rudnick. CRC Press, 2009. Chap. 22, pp. 523–584.

[7] R. L. Wallace. "The reproduction of magnetically recorded signals". In: *Bell System Technical Journal* 30.4 (1951), pp. 1145–1173.

[8] B. Marchon and T. Olson. "Magnetic spacing trends: from LMR to PMR and beyond". In: *IEEE Transactions on Magnetics* 45.10 (2009), pp. 3608–3611.

[9] P. E. K. Dallas, W. Meyer, and J. C. Liu. "Slider with temperature responsive transducer positioning". US Patent 5991113A (23 November 1999).

[10] M. Kurita et al. "Flying-height reduction of magnetic-head slider due to thermal protrusion". In: *IEEE Transactions on Magnetics* 41.10 (2005), pp. 3007–3009.

[11] J.-Y. Juang, D. Chen, and David B. Bogy. "Alternate air bearing slider designs for areal density of 1 Tb/in^2". In: *IEEE Transactions on Magnetics* 42.2 (2006), pp. 241–246.

[12] J.-Y. Juang et al. “Numerical and Experimental Analyses of Nanometer-Scale Flying Height Control of Magnetic Head With Heating Element”. In: *IEEE Transactions on Magnetics* 44.11 (2008), pp. 3679–3682.

[13] K. Aoki and T. Watanabe. “Nonlinearity of Thermal Spacing Control in Hard Disk Drives”. In: *IEEE Transactions on Magnetics* 45.2 (2009), pp. 816–821.

[14] H. Zheng, H. Li, and F. E. Talke. “Numerical simulation of a thermal flying height control slider with dual heater and insulator elements”. In: *IEEE Transactions on Magnetics* 45 (2009), pp. 3628–3631.

[15] N. Liu, J. Zheng, and D. B. Bogy. “Predicting the flying performance of thermal flying-height control sliders in hard disk drives”. In: *Journal of Applied Physics* 108.1 (2010), p. 016102.

[16] L. Li, H. Zheng, and F. E. Talke. “Investigation of Nanoscale Heat Transfer and Flying Characteristics in Thermal Flying Height Control Sliders Considering Near-Field Radiation”. In: *Tribology Letters* 59.1 (2015), p. 12.

[17] J. Xu et al. “Contact/Clearance Sensor for HDI Subnanometer Regime”. In: *IEEE Transactions on Magnetics* 50.3 (2014), pp. 114–118.

[18] S. Zhang and D.B. Bogy. “A heat transfer model for thermal fluctuations in a thin slider/disk air bearing”. In: *International Journal of Heat and Mass Transfer* 42.10 (1999), pp. 1791–1800.

[19] D. Chen, N. Liu, and D.B Bogy. “A phenomenological heat transfer model for the molecular gas lubrication system in hard disk drives”. In: *Journal of Applied Physics* 105.8 (2009), p. 084303.

[20] S. Shen, A. Narayanaswamy, and G. Chen. “Surface Phonon Polaritons Mediated Energy Transfer between Nanoscale Gaps”. In: *Nano Letters* 9.8 (2009), pp. 2909–2913.

[21] K. Kim et al. “Radiative heat transfer in the extreme near field”. In: *Nature* 528.7582 (2015), pp. 387–391.

[22] B. V. Budaev and D. B. Bogy. “Computation of radiative heat transport across a nanoscale vacuum gap”. In: *Applied Physics Letters* 104.6 (2014), p. 061109.

[23] B. V. Budaev and D. B. Bogy. “Heat transport by phonon tunneling across layered structures used in heat assisted magnetic recording”. In: *Journal of Applied Physics* 117.10 (2015), p. 104512.

[24] B. V. Budaev, A. Ghafari, and D. B. Bogy. “Intense radiative heat transport across a nano-scale gap”. In: *Journal of Applied Physics* 119.14 (2016), p. 144501.

[25] B. V. Budaev and D. B. Bogy. “A wave theory of heat transport with applications to Kapitsa resistance and thermal rectification”. In: *Proceedings of the Royal Society A* 473.2198 (2017), p. 20160584.

[26] M. H. Kryder et al. "Heat assisted magnetic recording". In: *IEEE Transactions on Magnetics* 96.11 (2008), pp. 1810–1835.

[27] D. Weller et al. "High K_u materials approach to 100 Gbits/in^2". In: *IEEE Transactions on Magnetics* 36.1 (2000), pp. 10–15.

[28] B. Marchon et al. "Head–Disk Interface Materials Issues in Heat-Assisted Magnetic Recording". In: *IEEE Transactions on Magnetics* 50.3 (2014), p. 3300607.

[29] J. D. Kiely et al. "Write-Induced Head Contamination in Heat-Assisted Magnetic Recording". In: *IEEE Transactions on Magnetics* 53.2 (2017), p. 3300307.

[30] S. Xiong et al. "Material Transfer Inside Head Disk Interface for Heat Assisted Magnetic Recording". In: *Tribology Letters* 65.2 (2017), p. 74.

[31] L. Wu. "Modelling and simulation of the lubricant depletion process induced by laser heating in heat-assisted magnetic recording system". In: *Nanotechnology* 18.21 (2007), p. 215702.

[32] J. B. Dahl and David B Bogy. "Lubricant flow and evaporation model for heat-assisted magnetic recording including functional end-group effects and thin film viscosity". In: *Tribology Letters* 52.1 (2013), pp. 27–45.

[33] B. Marchon and Y. Saito. "Lubricant Thermodiffusion in Heat Assisted Magnetic Recording". In: *IEEE Transactions on Magnetics* 48.11 (2012), pp. 4471–4474.

[34] J. B. Dahl and D.B. Bogy. "Simulation of lubricant recovery after heat-assisted magnetic recording writing". In: *Tribology Letters* 52.1 (2013), pp. 163–174.

[35] M. S. G. Sarabi and D. B. Bogy. "Simulation of the Performance of Various PFPE Lubricants Under Heat Assisted Magnetic Recording Conditions". In: *Tribology Letters* 56.2 (2014), pp. 293–304.

[36] R. I. Tanner. *Engineering Rheology*. Clarendon Press, Oxford, 2000.

[37] S. Sarabi and D.B. Bogy. "Effect of Viscoelasticity on Lubricant Behavior Under Heat-Assisted Magnetic Recording". In: *Tribology Letters* 66.1 (2018), p. 33.

[38] J.-G. Zhu, X. Zhu, and Y. Tang. "Microwave assisted magnetic recording". In: *IEEE Transactions on Magnetics* 44.1 (2008), pp. 125–131.

[39] C. Boone et al. "Heat sink for a spin torque oscillator (STO) in microwave assisted magnetic recording (MAMR)". US Patent 8995088B1 (31 March 2015).

[40] B. Marchon et al. "A model for Lubricant flow from disk to slider". In: *IEEE Transactions on Magnetics* 39.5 (2003), pp. 2447–2449.

[41] Y. Ma and B. Liu. "Dominant Factors in Lubricant Transfer and Accumulation in Slider-Disk Interface". In: *Tribology letters* 29.2 (2008), pp. 119–127.

[42] Y. Ma and B. Liu. "Lube Depletion Caused by Thermal-Desorption in Heat Assisted Magnetic Recording". In: *IEEE transactions in magnetics* 44.11 (2008), pp. 3691–3694.

[43] Y. Yang et al. “Head–Disk Lubricant Transfer and Deposition During Heat-Assisted Magnetic Recording Write Operations”. In: *IEEE Transactions on Magnetics* 51.11 (2015), p. 3300604.

[44] L. Wu. “A model for liquid transfer between two approaching gas bearing surfaces through coupled evaporation-condensation and migration dynamics”. In: *Journal of Applied Physics* 104.1 (2008), p. 014503.

[45] R. P. Ambekar et al. “Critical clearance and lubricant instability at the head-disk interface of a disk drive”. In: *Applied Physics Letters* 92.3 (2008), p. 033104.

[46] C. M. Mate. “Taking a Fresh Look at Disjoining Pressure of Lubricants at Slider-Disk Interfaces”. In: *IEEE Transactions on Magnetics* 47.1 (2011), pp. 124–130.

[47] R. J. Waltman et al. “The Effect of PFPE Film Thickness and Molecular Polarity on the Pick-Up of Disk Lubricant by a Low-Flying Slider”. In: *Tribology Letters* 39.2 (2010), pp. 211–219.

[48] Y. Zhang and A. A. Polycarpou. “Lubricant Transfer Model at the Head-Disk Interface in Magnetic Storage Considering Lubricant–Lubricant Interaction”. In: *Tribology Letters* 62.3 (2016), p. 38.

[49] N. Li, Y. Meng, and D. B. Bogy. “Effects of PFPE Lubricant Properties on the Critical Clearance and Rate of the Lubricant Transfer from Disk Surface to Slider”. In: *Physical Review E* 43.3 (2011), pp. 275–286.

[50] L. Wu and F. E. Talke. “Modeling laser induced lubricant depletion in heat-assisted-magnetic recording systems using a multiple-layered disk structure”. In: *Microsystem Technologies* 17.5-7 (2011), pp. 1109–1114.

[51] A. R. Mendez and David B Bogy. “Lubricant flow and accumulation on the slider’s air-bearing surface in a hard disk drive”. In: *Tribology Letters* 53.2 (2014), pp. 469–476.

[52] C. M. Mate and B. Marchon. “Shear Response of Molecularly Thin Liquid Films to an Applied Air Stress”. In: *Physical Review Letters* 85.18 (2000), pp. 1333–1339.

[53] T. E. Karis et al. “Lubricant spin-off from magnetic recording disks”. In: *Tribology Letters* 11.3-4 (2001), pp. 151–159.

[54] M. Scarpulla, C. M. Mate, and M. Carter. “Air shear driven flow of thin perfluoropolyether polymer films”. In: *The Journal of Chemical Physics* 118.7 (2003), p. 3368.

[55] X. Dai et al. “Study of Perfluoropolyether Lubricant Consumption and Recovery in Heat Assisted Magnetic Recording Using Molecular Dynamics Simulation Method”. In: *IEEE Transactions on Magnetics* 53.3 (2017), p. 3301606.

[56] X. Dai et al. “Study of Formation and Development of Lubricant Bridge in Head - Disk Interface Using Molecular Dynamic Method”. In: *IEEE Transactions on Magnetics* 53.3 (2017), p. 3301204.

[57] Y. Seo et al. “Molecular Dynamics Simulation of Lubricant Transfer at the Head-Disk Interface”. In: *IEEE Transactions on Magnetics* 50.11 (2014), p. 3302904.

[58] Y. Seo, A. Ovcharenko, and F. Talke. “Simulation of Hydrocarbon Oil Contamination at the Head-Disk Interface Using Molecular Dynamics”. In: *Tribology Letters* 61.3 (2016), p. 28.

[59] J. B. Dahl. “Heat Assisted Magnetic Recording Head-Disk Interface: Numerical Simulation of Air Bearing and Lubricant Mechanics”. Ph.D. thesis. University of California, Berkeley, 2013.

[60] A. Oron, Stephen H Davis, and S George Bankoff. “Long-scale evolution of thin liquid films”. In: *Reviews of Modern Physics* 69.3 (1997), pp. 931–980.

[61] G. Batchelor. *An Introduction to Fluid Dynamics*. Cambridge University Press, Cambridge, 1976.

[62] B. V. Derjaguin, N. V. Churaev, and V. Muller. *Surface Forces*. Plenum Publishing Corporation, New York, 1987.

[63] L. Wu. “Lubricant dynamics under sliding condition in disk drives”. In: *Journal of Applied Physics* 100.2 (2006), p. 024505.

[64] T. E. Karis and G. W. Tyndall. “Calculation of spreading profiles for molecularly-thin films from surface energy gradients”. In: *Journal of Non-Newtonian Fluid Mechanics* 82.2 (1999), pp. 287–302.

[65] G. W. Tyndall et al. “Interfacial interactions of perfluoropolyether lubricants with magnetic recording media”. In: *Tribology Letters* 4.2 (1998), pp. 103–108.

[66] R. Pit et al. “Formation of lubricant “moguls” at the head/disk interface”. In: *Tribology Letters* 10.3 (2001), pp. 133–142.

[67] B. V. Derjaguin and N. V. Churaev. “Polymolecular adsorption and capillary condensation in narrow slit pores”. In: *Journal of Colloid and Interface Science* 54.2 (1976), pp. 157–175.

[68] M. Forcada. “Instability in a system of two interacting liquid films: Formation of liquid bridges between solid surfaces”. In: *The Journal of Chemical Physics* 98.1 (1993), pp. 638–643.

[69] H. K. Christenson. “Capillary Condensation due to vander Waals Attraction in Wet Slits”. In: *Physical Review Letters* 73.13 (1994), pp. 1821–1824.

[70] J. N. Israelachvili. *Intermolecular and surface forces: revised third edition*. Academic press, 2011.

[71] V. P. Carey. *Liquid-Vapor Phase-Change Phenomena*. Taylor and Francis Group, LLC, New York, 2008.

[72] G. M. Rosenblatt. “Evaporation from Solids”. In: *Treatise on Solid State Chemistry*. Ed. by N. Hannay. Plenum Press, New York, 1976. Chap. 3, pp. 165–240.

[73] J. B. Dahl and David B Bogy. "Heat-assisted magnetic recording air bearing simulations that account for lateral air temperature variation". In: *IEEE Transactions on Magnetics* 47.10 (2011), pp. 2379–2382.

[74] J. B. Dahl and D. B. Bogy. "Static and Dynamic Slider Air-Bearing Behavior in Heat-Assisted Magnetic Recording Under Thermal Flying Height Control and Laser System-Induced Protrusion". In: *Tribology Letters* 54.1 (2014), pp. 35–50.

[75] J. O. Hirschfelder, R. B. Bird, and E. L. Spotz. "The Transport Properties of Gases and Gaseous Mixtures. II." In: *Chem. Rev.* 44.1 (1949), pp. 205–231.

[76] S. Patankar. *Numerical Heat Transfer and Fluid Flow*. Hemisphere Publishing Corporation, New York, 1980.

[77] T. Yabe et al. "The compact CIP (Cubic-Interpolated Pseudo-particle) method as a general hyperbolic solver". In: *Computers & Fluids* 19.3-4 (1991), pp. 421–431.

[78] T. Aoki. "Multi-dimensional advection of CIP (cubicinterpolated propagation) scheme". In: *International Journal of Computational Fluid Dynamics* 4.3 (1995), pp. 279–291.

[79] P. M. Jones et al. "Laser-Induced Thermo-Desorption of Perfluoropolyether Lubricant from the Surface of a Heat-Assisted Magnetic Recording Disk: Lubricant Evaporation and Diffusion". In: *Tribology Letters* 59.2 (2015), pp. 1–6.

[80] R. Z. Lei, A. J. Gellman, and P. Jones. "Thermal Stability of Fomblin Z and Fomblin Zdol Thin Films on Amorphous Hydrogenated Carbon". In: *Tribology Letters* 11.1 (2001), pp. 1–5.

[81] W. Zhou et al. "Evaporation of Polydisperse Perfluoropolyether Lubricants in Heat-Assisted Magnetic Recording". In: *Applied Physics Express* 4.9 (2011), p. 095201.

[82] B. Dai, L.G. Leal, and A. Redondo. "Disjoining pressure for nonuniform thin films". In: *Physical Review E* 78.6 (2008), p. 061602.

[83] S. V. Sakhalkar and D. B. Bogy. "A Model for Lubricant Transfer from Media to Head During Heat-Assisted Magnetic Recording (HAMR) Writing". In: *Tribology Letters* 65.4 (2017), p. 166.

[84] R.-N. Kono et al. "Rheology of perfluoropolyether lubricants". In: *IEEE Transactions on Magnetics* 37.4 (2001), pp. 1827–1829.

[85] H. J. Choi et al. "Viscoelasticity and solution viscosity of perfluoropolyether lubricants". In: *Tribology International* 38.6-7 (2005), pp. 682–686.

[86] C. M. Mate et al. "Lubricant-Induced Spacing Increases at Slider-Disk Interfaces in Disk Drives". In: *Tribology Letters* 37.3 (2010), pp. 581–590.

[87] M. Ruths and S. Granick. "Tribology of confined Fomblin-Z perfluoropolyalkylethers: molecular weight dependence and comparison between unfunctionalized and telechelic chains". In: *Tribology Letters* 7.4 (1999), pp. 161–172.

[88] S. Itoh et al. “Fiber Wobbling Method for Dynamic Viscoelastic Measurement of Liquid Lubricant Confined in Molecularly Narrow Gaps”. In: *Tribology Letters* 30.3 (2008), pp. 177–189.

[89] S. Itoh et al. “Opposing effects of confinement and confinement-induced shear-thinning on viscoelastic properties of liquid lubricant in nanometer-scale gaps”. In: *Tribology International* 44.11 (2011), pp. 1333–1339.

[90] B. Marchon et al. “Lubricant dynamics on a slider: “The waterfall effect””. In: *Journal of Applied Physics* 105.7 (2009), p. 074313.

[91] K. R. Rajagopal. “On some unresolved issues in non-linear fluid dynamics”. In: *Russian Mathematical Surveys* 58.2 (2003), pp. 319–330.

[92] M. Rauscher et al. “A thin-film equation for viscoelastic liquids of Jeffreys type”. In: *The European Physical Journal E* 17.3 (2005), pp. 373–379.

[93] R. Blossey. “Thin film rupture and polymer flow”. In: *Physical Chemistry Chemical Physics* 10.34 (2008), pp. 5177–5183.

[94] R. LeVeque. *Finite Difference Methods for Ordinary and Partial Differential Equations*. SIAM, Philadelphia, PA, 2007.

[95] J. Tichy. “Non-Newtonian Lubrication With the Convected Maxwell Model”. In: *Journal of Tribology* 118.2 (1996), pp. 344–348.

[96] W. Schowalter. “The behaviour of complex fluids at solid boundaries”. In: *Journal of Non-Newtonian Fluid Mechanics* 29 (1988), pp. 25–36.

[97] S. V. Sakhalkar and D. B. Bogy. “Effect of rheology and slip on lubricant deformation and disk-to-head transfer during heat-assisted magnetic recording (HAMR)”. In: *Tribology Letters* 66.4 (2018), p. 145.

[98] © 2018 IEEE. Reprinted, with permission, from S. V. Sakhalkar and D. B. Bogy. “Viscoelastic Lubricant Deformation and Disk-to-Head Transfer During Heat-Assisted Magnetic Recording”. In: *IEEE Transactions on Magnetics* 55.7 (July 2019), p. 3300506.

[99] J. Aoyama et al. “A Head Cleaning Procedure for Heat-Assisted Magnetic Recording”. In: *IEEE Transactions on Magnetics* 53.11 (2017), p. 3102004.

[100] J. Kiely, P. Jones, and J. Hoehn. “Materials challenges for the heat-assisted magnetic recording head-disk interface”. In: *MRS Bulletin* 43.2 (2018), pp. 119–124.

[101] H. Tani et al. “Smear growth on head slider surface from siloxane outgas on heat assisted magnetic recording”. In: *Microsystem Technologies* 24.1 (2018), pp. 4641–4648.

[102] Solvay-Solexis: Fomblin Z Derivatives: Product Data Sheet. Solvay Solexis, Inc., North America (2002).

[103] Y. Zhang and A. Polycarpou. "A single asperity sliding contact model for molecularly thin lubricant". In: *Microsystem Technologies* 23.6 (2017), pp. 1733–1741.

[104] S. H. Kim et al. "Humidity effects on lubricant transfer in the head-disk interface of a hard disk drive". In: *Journal of Applied Physics* 105.7 (2009), 07B704.

[105] B. V. Budaev and D. B. Bogy. "Thermal rectification in inhomogeneous nanotubes". In: *Applied Physics Letters* 109.23 (2016), p. 231905.

[106] B. V. Budaev and D. B. Bogy. "Systems with a constant heat flux with applications to radiative heat transport across nanoscale gaps and layers". In: *Zeitschrift für angewandte Mathematik und Physik* 69 (2018), p. 71.

[107] R. Prasher. "Acoustic mismatch model for thermal contact resistance of van der Waals contacts". In: *Applied Physics Letters* 94.4 (2009), p. 041905.

[108] M. Prunnila and J. Meltaus. "Acoustic Phonon Tunneling and Heat Transport due to Evanescent Electric Fields". In: *Physical Review Letters* 105.12 (2010), p. 125501.

[109] Y. Ezzahri and K. Joulain. "Vacuum-induced phonon transfer between two solid dielectric materials: Illustrating the case of Casimir force coupling". In: *Physical Review B* 90.11 (2014), p. 115433.

[110] C. Henkel and P. P. Schmidt. "On anomalously large nano-scale heat transfer between metals". In: *Journal of the Optical Society of America B* 36.4 (2019), pp. C10–C14.

[111] Y. Ma et al. "Controlled heat flux measurement across a closing nanoscale gap and its comparison to theory". In: *Applied Physics Letters* 108.21 (2016), p. 213105.

[112] Y. Ma et al. "Measurement and Simulation of Nanoscale Gap Heat Transfer Using a Read/Write Head With a Contact Sensor". In: *IEEE Transactions on Magnetics* 53.2 (2017), p. 3300105.

[113] H. Wu and D.B. Bogy. "Use of an embedded contact sensor to study nanoscale heat transfer in heat assisted magnetic recording". In: *Applied Physics Letters* 110.3 (2017), p. 033104.

[114] J. Zheng, Y.-K. Chen, and Q. Zhou. "Heat transfer across a nanoscale pressurized air gap and its application in magnetic recording". In: *Scientific Reports* 8.1 (2018), p. 3343.

[115] N. Zuckerman et al. "Sensing and Modeling Heat Transfer Between a Recording Head and Medium for Clearance Setting in HAMR". In: *IEEE Transactions on Magnetics* 55.3 (2019), p. 3300205.

[116] Y. Ma et al. "Study of Head-Disk Interface Characterization Using Touchdown Sensor and Electromagnetic Signal in Hard Disk Drives". In: *IEEE Transactions on Magnetics* 51.11 (2015), p. 3300504.

[117] Y. Ma et al. "A study of the nanoscale heat transfer in the hdd head-disk interface based on a static touchdown experiment". In: *IEEE Transactions on Magnetics* 56.3 (2020), p. 3300107.

[118] P. Wurfel. "The chemical potential of radiation". In: *Journal of Physics C: Solid State Physics* 15.18 (1982), pp. 3967–3985.

[119] L. M. Martyushev and V. D. Seleznev. "Maximum entropy production principle in physics, chemistry and biology". In: *Physics Reports* 426.1 (2006), pp. 1–45.

[120] D. G. Cahill, K. Goodson, and A. Majumdar. "Thermometry and Thermal Transport in Micro/Nanoscale Solid-State Devices and Structures". In: *Journal of Heat Transfer* 124.2 (2001), pp. 223–241.

[121] L. Wu and D. B. Bogy. "Effect of the Intermolecular Forces on the Flying Attitude of Sub-5 NM Flying Height Air Bearing Sliders in Hard Disk Drives". In: *Journal of Tribology* 124.3 (2002), pp. 562–567.

[122] C. G. Broyden. "A class of methods for solving nonlinear simultaneous equations". In: *Mathematics of Computation* 19 (1965), pp. 577–593.

[123] B. C. Gundrum, D. G. Cahill, and R. S. Averback. "Thermal conductance of metal-metal interfaces". In: *Physical Review B* 72.24 (2005), p. 245426.

[124] L. M. Jiji. "Microscale Conduction". In: *Heat Conduction*. 3rd ed. Berlin, Heidelberg: Springer, 2009. Chap. 11, pp. 347–401.

[125] A. Ovcharenko et al. "Simulation of Magnetic Erasure Due to Transient Slider-Disk Contacts". In: *IEEE Transactions on Magnetics* 46.10 (2010), pp. 770–777.

[126] M. Shamsa et al. "Thermal conductivity of diamond-like carbon films". In: *Applied Physics Letters* 89.16 (2006), p. 161921.

[127] M. Suk, P. Dennig, and D. Gillis. "Magnetic Erasures Due to Impact Induced Interfacial Heating and Magnetostriction". In: *Journal of Tribology* 122.1 (1999), pp. 264–268.

[128] S. V. Sakhalkar et al. "Numerical and experimental investigation of heat transfer across a nanoscale gap between a magnetic recording head and various media". In: *Applied Physics Letters* 115.22 (2019), p. 223102.

[129] Q. Cheng et al. "Dependence of nanoscale heat transfer across a closing gap on the substrate material and ambient humidity". In: *Applied Physics Letters* 116.21 (2020), p. 213102.

[130] S. V. Sakhalkar et al. "Numerical and Experimental Investigation of Nanoscale Heat Transfer in the Head-Media Interface During Static Touchdown". In: *Proceedings of the ASME 2019 28th Conference on Information Storage and Processing Systems. ASME 2019 28th Conference on Information Storage and Processing Systems.* San Diego, California, USA. June 27–28 (2019).

[131] H. Stanley, I. Etsion, and D. Bogy. "Adhesion of Contacting Rough Surfaces in the Presence of Sub-Boundary Lubrication". In: *ASME Journal of Tribology* 112.1 (1990), pp. 98–104.

[132] J. Zheng and D. B. Bogy. "Investigation of flying-height stability of thermal fly-height control sliders in lubricant or solid contact with roughness". In: *Tribology Letters* 38.3 (2010), pp. 283–289.

[133] J. Zheng and D. B. Bogy. "Numerical simulation of touchdown dynamics of thermal flying-height control sliders". In: *IEEE Transactions on Magnetics* 48.9 (2012), pp. 2415–2420.

[134] J. Zheng and D. B. Bogy. "A numerical investigation of different touchdown patterns of thermal-flying-height-control sliders". In: *Microsystem Technologies* 19.9-10 (2013), pp. 1377–1381.

[135] G.-J. Lo, C. M. Mate, and Q. Dai. "Finite Element Simulation of the Mechanical and Thermal Behaviors of a Disk Drive Head Contacting a Disk Asperity". In: *Tribology Letters* 64.1 (2016), p. 6.

[136] S. Lee et al. "Thermomechanical contact between magnetic recording head and disk defect accounting for heat partition factor". In: *IEEE Transactions on Magnetics* 50.3 (2014), p. 3300307.

[137] K. Ono. "Numerical Method of Analyzing Contact Mechanics between a Sphere and a Flat Considering Lennard-Jones Surface Forces of Contacting Asperities and Non-contacting Rough Surfaces". In: *ASME Journal of Tribology* 134.1 (2012), p. 011402.

[138] K. Ono. "Surface Texture Parameters of Perpendicular Magnetic Recording Disks". In: *IEEE Transactions on Magnetics* 53.3 (2017), p. 3300806.

[139] K. Ono. "Analysis of Microwaviness-Excited Vibrations of a Flying Head Slider in Proximity and Asperity Contact Regimes". In: *ASME Journal of Tribology* 139.6 (2017), p. 062001.

[140] A. Y. Suh and A. A. Polycarpou. "Adhesive contact modeling for sub-5-nm ultralow flying magnetic storage head-disk interfaces including roughness effects". In: *Journal of Applied Physics* 97.10 (2005), p. 104328.

[141] A. Y. Suh and A. A. Polycarpou. "Analytical determination of the surface energy of sub-5-nm head-disk interfaces accounting for multilayer effects". In: *Journal of Applied Physics* 99.8 (2006), 08N111.

[142] C. T. Rettner. "Thermal and tangential-momentum accommodation coefficients for N_2 colliding with surfaces of relevance to disk-drive air bearings derived from molecular beam scattering". In: *IEEE Transactions on Magnetics* 34.4 (1998), pp. 2387–2395.

[143] W. Zhou et al. "Numerical Simulations of Accommodation Coefficient Effects at the Head-Disk Interface". In: *Japanese Journal of Applied Physics* 49.9R (2010), p. 095206.

[144] C. M. Mate et al. "Nanoscale origins of dynamic friction in an asymmetric contact geometry". In: *Physical Review Letters* 97.21-24 (2006), p. 216104.

[145] F. Ling, W. Lai, and D. Lucca. "Surface Temperatures in Moving Bodies". In: *Fundamentals of Surface Mechanics*. 2nd ed. New York: Springer, 2002. Chap. 2, pp. 11–68.

[146] S. Fukui and R. Kaneko. "Analysis of Ultra-Thin Gas Film Lubrication Based on Linearized Boltzmann Equation: First Report—Derivation of a Generalized Lubrication Equation Including Thermal Creep Flow". In: *Journal of Tribology* 110.2 (1988), pp. 253–261.

[147] S. Lu. "Numerical simulation of slider air bearings". Ph.D. thesis. University of California, Berkeley, 1997.

[148] S. Fukui and R. Kaneko. "A Database for Interpolation of Poiseuille Flow-Rates for High Knudsen Number Lubrication Problems". In: *Journal of Tribology* 112.1 (1990), pp. 78–83.

[149] J. Zheng. "Dynamics and Stability of Thermal Flying-height Control Sliders in Hard Disk Drives". Ph.D. thesis. University of California, Berkeley, 2012.

[150] M. G. Beghi et al. "Bonding and mechanical properties of ultrathin diamond-like carbon films". In: *Applied Physics Letters* 81.20 (2002), p. 38044.

[151] V. Gupta and D. B. Bogy. "Dynamics of sub-5-nm air-bearing sliders in the presence of electrostatic and intermolecular forces at the head-disk interface". In: *IEEE Transactions on Magnetics* 41.2 (2005), pp. 610–615.

[152] S. Canchi and D. B. Bogy. "Slider dynamics in the lubricant-contact regime". In: *IEEE Transactions on Magnetics* 46.3 (2010), pp. 764–69.

[153] Y-K Chen, J. Zheng, and D.B. Bogy. "Light contact and surfing state dynamics of air bearing sliders in hard disk drives". In: *Applied Physics Letters* 100.24 (2012), p. 243104.

[154] Y-K Chen, J.-P. Peng, and D. B. Bogy. "Thermal protrusion-induced air bearing slider instability at disk proximity and light contact". In: *IEEE Transactions on Magnetics* 50.7 (2014), p. 3301707.

[155] Y. S. Ma et al. "Adsorbed Water Film and Heat Conduction from Disk to Slider in Heat-Assisted Magnetic Recording". In: *Tribology Letters* 56.1 (2014), pp. 93–99.

[156] S. V. Sakhalkar et al. "Investigation of Heat Transfer across a Nanoscale Air Gap Between a Flying Head and a Rotating Disk". In: *Journal of Applied Physics* (submitted) (2020).

[157] S. V. Sakhalkar, Q. Cheng, and D. B. Bogy. "Numerical and Experimental Investigation of Nanoscale Heat Transfer Between a Flying Head Over a Rotating Disk". In: *Proceedings of the ASME 2020 29th Conference on Information Storage and Processing Systems. ASME 2020 29th Conference on Information Storage and Processing Systems.* (to be published) Virtual, Online. June 24–25 (2020).

[158] J.-Y. Juang and J. Zheng. "Thermal analysis of continuous and patterned multilayer films in the presence of a nanoscale hot spot". In: *AIP Advances* 6.10 (2014), p. 105102.

[159] E. Schreck et al. "Thermal Aspects and Static/Dynamic Protrusion Behaviors in Heat-Assisted Magnetic Recording". In: *IEEE Transactions on Magnetics* 50.3 (2014), p. 3300406.

[160] S. Xiong et al. "Thermal Response Time of Media in Heat-Assisted Magnetic Recording". In: *IEEE Transactions on Magnetics* 53.10 (2017), p. 3301906.

[161] A. Lyberatos and G. J. Parker. "Model of ballistic-diffusive thermal transport in HAMR media". In: *Japanese Journal of Applied Physics* 58.4 (2019), p. 045002.

[162] T. Rausch. "Standard media stack and figure of merits for HAMR NFT modeling," ASTC Heads Working Group, Technical Report, 2011.

[163] Y. Hu et al. "Nanoscale thermal analysis for heat-assisted magnetic recording". In: *Journal of Applied Physics* 122.13 (2017), p. 134303.

[164] B. Xu et al. "Thermal Effects in Heat Assisted Bit Patterned Media Recording". In: *IEEE Transactions on Magnetics* 45.5 (2009), pp. 2292–2295.

[165] A. Chernyshov et al. "Measurement of FePt thermal properties relevant to heat-assisted magnetic recording". In: *Journal of Applied Physics* 115.17 (2014), 17B735.